Chaotic Advection for Enhanced Reagent Mixing

by

Michelle Seeun Cho

A thesis
presented to the University of Waterloo
in fulfillment of the
thesis requirement for the degree of
Doctor of Philosophy
in
Civil Engineering

Waterloo, Ontario, Canada, 2019

Examining Committee Membership

The following served on the Examining Committee for this thesis. The decision of the Examining Committee is by majority vote.

External Examiner	David C. Mays Associate Professor, University of Colorado Denver
Supervisor(s)	Neil R. Thomson Professor, University of Waterloo
Internal Member	James R. Craig Associate Professor, University of Waterloo
Internal-external Member	Walter A. Illman Professor, University of Waterloo
Internal-external Member	David L. Rudolph Professor, University of Waterloo

Author's Declaration

This thesis consists of material all of which I authored or co-authored: see Statement of Contributions included in the thesis. This is a true copy of the thesis, including any required final revisions, as accepted by my examiners.

I understand that my thesis may be made electronically available to the public.

Statement of Contributions

Chapter 2 of this thesis is reproduced from a paper that has been submitted for publication, which was co-authored by myself, Mr. Felipe Solano (University of Waterloo, now at Geosyntec Consultants), Dr. Neil R. Thomson (University of Waterloo), Dr. Michael G. Trefry (independent researcher), Dr. Daniel R. Lester (RMIT University), and Dr. Guy Metcalfe (Swinburne University of Technology). M.S.C. designed and performed the experiments, developed the quantitative methods for analysis, analyzed the data, prepared the figures/tables and wrote the manuscript. F.S. performed the experiments and provided suggestions for improvements to the design. N.R.T. supervised the project, aided with the design of the experiments, provided the materials and critically reviewed the manuscript. M.G.T., D.R.L. and G.M. helped with the interpretation of the data, offered suggestions for additional quantitative methods, and provided feedback on the manuscript based on their deep theoretical knowledge of chaotic advection.

Chapter 3 of this thesis been prepared with the intent for submission, which is co-authored by myself, Dr. Zhanfeng Zhao (University of Waterloo, now at the Institute of Geographic Science and Natural Resources Research, Chinese Academy of Sciences), Dr. Neil R. Thomson, and Dr. Walter A. Illman (University of Waterloo). M.S.C. designed and performed the field pumping tests, set-up and executed all simulations, analyzed the data, prepared the figures and wrote the manuscript. Z.Z. provided technical support to the inverse model algorithm, and aided with the interpretation of the model output. W.A.I. provided the algorithm and feedback on the manuscript. N.R.T supervised the project, aided with the conceptual modeling process, provided the support/materials, and critically reviewed the manuscript.

Chapter 4 of this thesis has been prepared with the intent for submission, and is co-authored by myself and my supervisor, Dr. Neil R. Thomson.

Abstract

In situ remediation techniques commonly involve the injection of a reagent into the subsurface to create a zone in which biological and/or chemical reactions lead to mass destruction of contaminants. In these injection-driven remedial systems, the delivery of reagent solutions is a key requirement for success; however, the design of an effective delivery system remains a significant challenge. Subsurface heterogeneities create preferential flow pathways over a range of spatial scales that produce an uneven distribution of the injected fluid. For conventional injection methods that use vertical wells, the injected reagent will follow the path of least resistance from the wellbore into the porous medium, and the distribution will be greater in areas of higher hydraulic conductivity (K) with potential to bypass adjacent regions of lower K. In these lower K zones, molecular diffusion is possibly the primary transport mechanism responsible to bring the injected reagent into contact with the contaminant; however, diffusion is a slow process and contributes to inefficient mixing.

Chaotic advection refers to the generation of small-scale structures from the repeated stretching and folding of fluid elements in a laminar flow regime. The small-scale structures produced by this chaotic stirring create fluid elements that are stretched out into long, thin filaments with a length scale sufficiently small for diffusion to promote efficient mixing. It has been theorized that chaotic advection has the potential to overcome preferential flow paths and enhance mixing. One configuration which has been theoretically and experimentally used to invoke chaotic advection in porous media is termed a rotated potential mixing (RPM) flow. An RPM flow system involves periodically re-oriented dipole flow through the transient switching of pressures at a series of radial wells. If chaotic advection can be invoked and controlled *in situ*, reagent delivery and treatment effectiveness may be significantly improved. Thus, the primary objective of this research effort was to improve our understanding of chaotic advection and its implications on reagent delivery.

To investigate if chaotic advection can be engineered in a natural aquifer system using RPM flow, and to assess the consequent impact on the spatial distribution of a conservative tracer, a series of field-scale experiments were completed. Investigations were performed in an experimental gate at the University of Waterloo Groundwater Research Facility at the Canadian Forces Base in Borden, ON, Canada. Each experiment involved the injection of a pre-determined

tracer volume in the center of a circular array of injection/extraction wells, followed by either mixing using an RPM flow protocol to invoke chaotic advection, or by natural processes (advection and diffusion) as the control. Hydraulic data and tracer breakthrough responses were used to investigate the presence of chaotic advection. Various quantitative metrics (e.g., integrated volume under the three-dimensional contours of tracer concentration data, variance of tracer concentrations, spatial concentration gradients, and the first two spatial moments of the tracer concentration distribution) were adopted to assess field-scale evidence of mixing. The results from these various quantitative metrics indicated the presence of chaotic advection which led to improved lateral spreading and enhanced mixing to establish uniform concentrations across the monitoring network. The findings demonstrated that an RPM flow system is a viable and efficient approach to enhance reagent mixing.

Prior to the implementation of a chaotic advection system, determination of the RPM flow protocol will likely require a numerical model for adequate representation of groundwater flow undergoing periodically re-oriented dipole pumping. It is expected that the K field will control the behavior of the system. To capture K heterogeneities in a target treatment zone, hydraulic head responses from multiple independent dipole pumping tests were used in a three-dimensional steady-state hydraulic tomography (SSHT) analysis. For validation of the estimated K field from SSHT analysis, forward simulations of steady-state and transient groundwater flow were performed. The impact of using this K field on the spatial distribution of a hypothetical reagent in the target treatment zone was then investigated using particle tracking methods. The findings demonstrated that the same well system used to invoke chaotic advection is a viable site characterization tool to delineate the variability of the K field using SSHT analysis. Furthermore, the use of this K field in a particle tracking engine led to more spatially and densely distributed particle trajectories indicative of enhanced reagent mixing than those produced by an effective parameter approach (i.e., a single value of K assigned across the entire spatial domain). These results suggested that using K information applicable to a specific area of interest leads to a more effective design of an RPM flow system that can enhance reagent mixing.

Simulations were performed in two dimensions to investigate whether a conventional modeling method can be used capture the transport behavior of a conservative reagent in the presence of chaotic advection, and to explore the impact of specific engineering controls associated with an RPM flow system on reagent mixing. The multiple lines of evidence assembled in this study demonstrated that this modeling approach captured the key features of the expected transport behavior reported in other studies of chaotic advection over a range of scales (e.g., theory, laboratory and field). Visual observations from the reagent distribution produced, and the results from the quantitative metrics of mixing behavior highlighted the different responses that are possible by the various combinations of RPM flow parameters explored. The findings demonstrated the importance of combining theoretical considerations with practical limitations when designing an RPM flow system. The flow rate and pumping duration were identified as key parameters of an RPM flow system that have direct consequences on the degree of reagent spreading and mixing. In addition, the use of the same RPM flow protocol in a heterogeneous *K* field led to significantly greater degree of reagent mixing than in a homogeneous *K* setting. These findings represent a significant step towards the development of a modeling approach for the design of an effective RPM flow system that can support field implementation of chaotic advection and promote enhanced reagent mixing.

The tracer experiments described in this proof-of-concept study are significant since these investigations are the first field-scale efforts to extend on the established theoretical underpinnings and observations from bench-scale experiments of chaotic advection. Multiple lines of evidence assembled in this research effort demonstrate that chaotic advection can be engineered at the field scale using an RPM flow system. These findings also provide comprehensive information about chaotic advection as an approach to enhance reagent mixing in a natural aquifer system. The suite of quantitative metrics and numerical efforts presented in this study provide various tools for the design of an RPM flow system, and the subsequent data interpretation to support field applications of chaotic advection. Collectively, the combination of experimental and computational efforts presented in this study provide comprehensive insights into an effective design and implementation of an RPM flow system to generate chaotic advection for enhanced reagent mixing.

Acknowledgements

Raising a child might not be the only thing that takes a village. I might suggest that it also takes a village to complete a Ph.D. (though I think this Ph.D. has taught me that we need "a village" to do just about everything in life). I have truly been blessed with a community who kept me going during the last six and a half years of this Ph.D. journey. Without them, this thesis and degree would not be possible.

First and foremost, I would like to thank my supervisor, Dr. Neil R. Thomson – for not only providing countless hours of technical guidance, but for always seeing my potential and challenging me to become the best version of myself. I am thankful that he took me on as his student and provided me with the opportunity to grow and thrive. At times, sincerely empathetic and at other times, a tough disciplinarian, Dr. Thomson was the best supervisor I could have asked for.

Financial support for this research was provided by a Natural Sciences and Engineering Research Council (NSERC) of Canada Graduate Scholarship, as well as by the American Petroleum Institute (API), and a NSERC Canada Collaborative Research and Development Grant (N.R. Thomson).

I would like to thank the members of my advisory committee Dr. James Craig, Dr. Walter Illman, Dr. David Rudolph and Dr. David Mays for sharing their time and technical expertise towards this thesis. I thank Dr. Michael G. Trefry, Dr. Daniel R. Lester and Dr. Guy Metcalfe, who welcomed me into the complex world of chaotic advection, and always explained the difficult concepts with patience and encouragement. I also owe a special thank you to Dr. Robert McKillop and Dr. David Brush in the Department of Civil and Environmental Engineering, who have been my unofficial mentors throughout my graduate studies. Every one of these individuals have expanded my knowledge in a unique way, and for that, I could not be more grateful.

I would like to extend my gratitude towards everyone who took part in this research effort over the years, from the eureka brainstorming sessions to the countless hours of field work: the staff at the University of Waterloo – present, past and retired (Felipe Solano, Terry Ridgway, Bob Ingleton, Paul Johnson, Shirley Chatten and Wayne Noble) and our co-op students (Michael DeWeerd, Julie Taylor, Kevin Lee, Lara De Beer and Bill McLaren). I am also grateful for the graduate students with whom I have been blessed to have crossed paths with during my Ph.D. journey (Dr. Mahsa Shayan, Dr. Saeid Shafieiyoun, Yunxiao Wei, Iolanda Montagnese, Janice Cooper, Lorenzo Simonetti, Andrea Marrocco, Zahra Sadeghi Ardestani, Sonia Jaberi, Brad Wilson, Silvia Vlad, Fred Cheng and Chris Rausch).

A special thank you to my dearest friends (Elaine, Sam, Rachel, Audrey, Joe, Philemon, Teresa, Sarah, Jessica and Allyson) and church community at New Hope Fellowship. I cannot thank them enough for the hours of listening to me rant and cry, as if it were the first time every time.

I would not be here today without the constant love, encouragement and prayers of my family (my parents, Lauren, James and in-laws). I am grateful that they never stopped believing that I had what it takes to keep going and finish this journey. They continue to be my best cheerleaders -- loving through me through each trial, and helping me to get up after each setback and failure.

I owe a huge part of this thesis to my husband, Francis – for his unconditional love, support and faith in me. From the long distance days while I was preparing for my comprehensive exam to getting married and seeing this thesis come to fruition, my gratitude goes to him for carrying the burden of this Ph.D. with me each day, especially on the days when I ran out of strength. He has been my tissue box, speaker of truth, and prayer warrior. He is also my personal barista, supplying me with my daily dose of caffeine (because coffee really is the lifeline of every Ph.D. student). I am thankful that I get to share this huge milestone with someone who is able to celebrate my accomplishments with more joy and pride than I do.

Truly, thank you all – from the bottom of my heart. I am made better by you.

Dedication

“For nothing is impossible with God” – Luke 1:37

To God be all the glory and praise.

Table of Contents

List of Figures

List of Tables

Chapter 1

Introduction

1.1 GENERAL BACKGROUND

Groundwater is a vital natural resource for domestic, agricultural and industrial uses in North America (Environment Canada, 2013; USGS, 2018); however, a lack of understanding and poor management practices have led to widespread contamination of this resource. While both natural and anthropogenic sources contribute to groundwater contamination, most of the compounds found in the subsurface originate from human activities, with organic compounds being the primary contaminants of concern (Kavanaugh et al., 2003; Kitanidis and McCarty, 2012). Common anthropogenic sources of groundwater contamination include leaking fuel and septic tanks, chemical spills, and improper application of pesticides and/or fertilizers. Chemical compounds released from these anthropogenic sources can be toxic and persistent in the subsurface (Environment Canada, 2017). As a result, substantial efforts have been devoted to the remediation of contaminated groundwater systems to protect human health and the environment.

In situ groundwater remediation techniques typically involve the injection of a reagent into the subsurface to create a zone in which biological and/or chemical reactions lead to the mass destruction of contaminants. For instance, chemical oxidants are delivered for the treatment of a wide range of organic contaminants (Siegrist and Simpkin, 2016). In enhanced bioremediation, electron acceptors and/or nutrients are injected to achieve a thriving environment for indigenous microbes to degrade organic contaminants (Reinhard et al, 1997; Liebeg and Cutright, 1999). In either situation, the delivery of reagent solutions is a key requirement for success; however, it remains a significant challenge (Kitanidis and McCarty, 2012).

Following the injection of a reagent solution, the desired chemical or biological transformations are initiated by transport processes that bring the injected reagent and contaminant together (Kitanidis and McCarty, 2012). While this contact between the injected reagent and contaminant is the desired outcome of an effective delivery system, it can be one of the most difficult to achieve. While spreading increases the zone of contact between the reagent and contaminant, subsurface heterogeneities create preferential flow pathways at a range of spatial scales (Dagan,

1986) that lead to uneven spatial distribution of the injected fluid. For conventional injection methods that use vertical wells, which rely on advection as the primary process of transporting injected solutions in porous media (Suthersan and Payne, 2005), the reagent distribution will be greater in the areas of higher hydraulic conductivity (*K*). The injected fluid follows the path of least resistance from the wellbore into the porous medium (Payne et al., 2008) with potential to bypass adjacent regions of lower permeability (Saenton et al., 2002; Zhong et al., 2011).

Ineffective reagent delivery can lead to partial removal of the contaminant mass. The remaining contaminant mass remains as immobilized, disconnected pockets that are trapped in diffusion-controlled zones (Conrad et al., 1992) or in the lower *K* zones where contact with the injected reagent is limited (Parker et al., 1994). In these regions, molecular diffusion ($D^* \sim 10^{-9}$ m^2/s) is possibly the primary transport mechanism responsible for bringing the injected reagent and contaminant together (Jose and Cirpka, 2004; Gale et al., 2015); however, diffusion is a slow process and contributes to ineffective mixing (Kitanidis and McCarty, 2012). This residual contaminant mass becomes as a long-term source that can lead to eventual rebound and persistence of dissolved plumes downgradient of the source zone (Thomson et al., 2008).

Various configurations of recirculation systems have been reported for *in situ* remediation. Most commonly, recirculation systems are designed as a single dipole, consisting of one injection and one extraction well (Payne et al., 2008). More complex systems have used multiple extraction wells placed in a grid pattern, surrounding a single injection well (Lowe et al., 2002), or a series of “nested” injection wells and extraction wells installed along the groundwater flow direction (Luo et al., 2007). In conventional recirculation systems, the extracted contaminated groundwater is mixed with the amendments above-ground before being re-injected (Kitanidis and McCarty, 2012). The “daisy wheel” approach is another configuration that has been reported to enhance mixing in *in situ* denitrification systems (Mercado et al., 1988), in which substrates are delivered through a series of small diameter wells surrounding a central extraction well. Conventional recirculation systems typically use steady and uniform flows; however, a time-dependent flow field is required to promote enhanced mixing (Aref, 1984; Ottino, 1989; Sposito, 2006), and it is . For example, Thomson et al. (2007) observed incomplete destruction of the source zone using a conventional recirculation system due to limited contact between the permanganate and residual NAPL mass. In light of these challenges associated with *in situ* treatment systems that involve reagent delivery, there is a need for a novel approach that can enhance mixing.

1.2 CHAOTIC ADVECTION

Chaotic advection (Trefry et al., 2012; Aref et al., 2017) has the potential to improve reagent distribution in the subsurface and promote enhanced mixing. Chaotic advection can be defined as the creation of "small-scale structures” caused by the repeated stretching and folding of fluid elements in a laminar flow regime (Ottino, 1989; Aref et al., 2017). This rapid stretching and folding of individual fluid parcels creates highly complex particle trajectories which have been theorized to improve the spatial distribution of solutes in porous media and increase the zone of contact across which reactions can occur (Ottino, 1989; Bagtzoglou and Oates, 2007; Lester et al., 2009; Mays and Neupauer, 2012). The “small-scale structures” produced from the chaotic stirring creates fluid elements that are exponentially stretched out into thin filaments with a length scale sufficiently small for diffusion to contribute to efficient mixing (Aref et al., 2017). If chaotic advection can be invoked and controlled *in situ*, reagent delivery and treatment effectiveness may be significantly improved (Bagtzoglou and Oates, 2007).

One configuration which has been theoretically and experimentally used to achieve chaotic advection in porous media involves periodically re-oriented dipole flow through the transient switching of pressures at a series of radial wells. This configuration has been termed rotated potential mixing (RPM) flow in relevant literature (Metcalfe et al., 2008). A conventional RPM flow protocol assumes a completely closed system where the fluid removed from the extraction well is immediately re-injected at the injection well (Trefry et al., 2012). In an RPM flow system, a dipole (i.e., one injection and one extraction well, separated by 180°) operates for a fixed time (t_p). The dipole is then instantaneously rotated by a reorientation angle (Θ) and resumes pumping for t_p. A repeated sequence of this periodic switching of dipole pumping may eventually cause the flow to become chaotic (Lester et al., 2009; Metcalfe et al., 2010a). This transient, periodic variation of the velocity field generated by an RPM flow system is an example of a time-dependent flow scheme that has potential to significantly improve the spatial distribution of the injected reagent and enhance mixing (Lester et al., 2009). The reorientation angle (Θ), pumping duration (t_p), and flow rate (Q) have been identified as key parameters in an RPM flow protocol (Metcalfe et al., 2010a) that can be configured to create either zones of enhanced mixing or confinement for increased residence time of reagents within the network of RPM flow injection/extraction wells (Trefry et al., 2012).

The established theoretical underpinnings (Sposito, 2006; Bagtzoglou and Oates, 2007; Trefry et al., 2012; Mays and Neupauer, 2012; Neupauer et al., 2014) and observations from bench-scale experiments (Zhang et al., 2009; Metcalfe et al., 2010b; Nissan et al., 2017) strongly suggest that chaotic advection has the potential to significantly improve reagent mixing at the field-scale; however, no previous effort has demonstrated chaotic advection in a natural aquifer system and investigated its effects on mixing. The underlying motivation for this research effort was to extend on this foundational work and investigate if chaotic advection can be invoked using an RPM flow protocol in a natural aquifer system. For successful implementation of an RPM flow system that can achieve chaotic advection and enhance reagent mixing, field investigations must be supported by a suite of quantitative metrics and modeling tools that can aid the design and interpretation process. For instance, published quantitative metrics that have been used to indicate the presence of chaotic advection (Ottino, 1990) were developed at the theoretical scale by tracking positions of individual fluid particles over space and time. Peer-reviewed studies of bench-scale experiments have reported the use of various analytical techniques based on images obtained from their experimental set-up (Zhang et al., 2009; Metcalfe et al., 2010b). Since these methods cannot be readily applied using the spatial and temporal resolution of typical field data, alternative quantitative metrics are needed to demonstrate the presence of chaotic advection and its impact on mixing. Furthermore, several peer-reviewed studies have demonstrated the use of various modeling methods to provide theoretical evidence of chaotic advection in porous media and its impacts on solute mixing (Mays and Neupauer, 2012; Neupauer et al., 2014; Rodriguez-Escales et al., 2017). Most of these studies have focused on advective particle tracking approaches to gain insight into chaotic mixing behavior, and there exist limited efforts to perform transport simulations specifically for an RPM flow system. The development of these modeling tools and quantitative metrics that can support field implementation of chaotic advection is critical for the design of an effective RPM flow system and data interpretation.

1.3 RESEARCH OBJECTIVES

To improve our understanding of chaotic advection and its implications on reagent mixing in porous media, the major objectives of this research were to:

1) Investigate the feasibility of an RPM flow protocol to generate engineered chaotic advection in a natural aquifer system,
2) Develop quantitative metrics to evaluate the presence of chaotic advection and its impacts on mixing based on the spatial and temporal resolution of field data,
3) Investigate whether the same well system required to invoke chaotic advection can be applied in a hydraulic tomography (HT) analysis to capture *K* heterogeneities in a target treatment zone,
4) Explore the impact of using the *K* field estimated from HT analysis on the selection of an RPM flow protocol and on the spatial distribution of a hypothetical reagent,
5) Determine whether a conventional modeling approach can capture the transport behavior of a conservative reagent subjected to an RPM flow system, and
6) Explore the impact of specific RPM flow parameters on reagent mixing.

1.4 THESIS SCOPE

The thesis is organized into five chapters, three of which are core chapters (Chapters 2 to 4) that address the research objectives. Chapter 5 summarizes the key contributions and conclusions emerging from this research effort, as well as recommendations for future work related to chaotic advection in the context of reagent delivery to support *in situ* remediation.

To investigate whether chaotic advection can be engineered in a natural porous medium using an RPM flow system and to assess the consequent impact on reagent mixing, a series of tracer experiments were conducted at the University of Waterloo Groundwater Research Facility at CFB Borden over two field seasons. Each experiment involved the injection of a pre-determined tracer volume in the center of a circular array of injection/extraction wells, followed by either mixing using an RPM flow protocol to invoke chaotic advection, or by natural processes (advection and diffusion) as the control. Hydraulic data and tracer breakthrough responses collected during the field tests were used to investigate the presence of chaotic advection. In addition, various quantitative metrics were adopted to demonstrate field-scale evidence of mixing. Chapter 2 is devoted to the results and discussion from these field investigations of chaotic advection using an RPM flow system, and addresses Objectives 1 and 2 of this research.

Prior to implementation of a chaotic advection system in the field, the selection of RPM flow parameters is critical to achieve the desired outcomes. Determination of an RPM flow protocol that is presumed to enhance reagent mixing will likely require a numerical model for adequate representation of groundwater flow undergoing transient, periodically re-oriented dipole pumping. It is expected that the *K* field will control the behavior of the system. Chapter 3 reports on an investigation to determine whether the same well system used to invoke chaotic advection can also be used as a site characterization tool to delineate *K* variability within a specific target treatment zone, and then to assess the impact of using this estimated *K* field on the spatial distribution of a hypothetical reagent. To generate an estimate of the *K* field in a target treatment zone (i.e., *K* tomogram), hydraulic head responses from multiple independent dipole pumping tests were used in a three-dimensional steady-state hydraulic tomography (SSHT) analysis. For validation of the *K* tomogram, forward simulations of steady-state and transient groundwater flow were performed. These forward simulation results using the *K* tomogram were then compared to those generated by an effective parameter approach in which a single value of *K*, as determined by single well pumping and slug tests, was assigned across the entire spatial domain as representation of the *K* distribution. The impact of the *K* tomogram on the spatial distribution of a hypothetical reagent in the target treatment zone was then investigated using particle tracking methods. Chapter 3 addresses Objectives 3 and 4 of this research.

Chapter 4 describes an investigation to explore whether a conventional modeling method can capture the transport behavior of a conservative reagent in the presence of chaotic advection, and to gain insight into the role specific RPM flow parameters have on reagent mixing behavior. The reagent transport behavior was simulated within an area of interest, as defined by the limits of eight injection/extraction wells in a circular array, which was chosen to represent a target treatment zone in a shallow aquifer system. Transport simulations consisted of an initial injection of a conservative reagent in the center of the circular array of injection/extraction wells, followed by the activation of an RPM flow protocol. Breakthrough curves at a series of hypothetical observation locations, and contours of simulated concentrations were generated within the area of interest. Particle tracking was also performed and compared to the expected behavior of theoretical diagnostic tools that have been reported to demonstrate the presence of chaotic advection. Various scenarios were then simulated to explore the impact of specific engineering controls of an RPM flow system on reagent mixing behavior. Chapter 4 addresses Objectives 5 and 6 of this research.

Chapters 2, 3 and 4 were edited by N.R. Thomson and prepared with the intent for submission for publication, and hence are written as stand-alone chapters. Some repetition across these chapters are unavoidable. Chapter 2 has been submitted to *Groundwater Monitoring and Remediation*. Chapters 3 and 4 have been prepared for submission to *Journal of Contaminant Hydrology*. A detailed list of contributions for the co-authored material is provided in the front matter of this thesis.

Chapter 2

Field Trials of Chaotic Advection to Enhance Reagent Delivery[1]

Abstract

Chaotic advection is a novel approach that has the potential to enhance contact between an injected reagent and target contaminants, and thereby improve the effectiveness of *in situ* treatment technologies. One configuration that is capable of generating chaotic advection is termed the rotated potential mixing (RPM) flow. A conventional RPM flow system involves periodically re-oriented dipole flow driven by transient switching of pressures at a series of radial wells. To determine whether chaotic advection can be engineered using such an RPM flow system, and to assess the consequent impact on the spatial distribution of a conservative tracer, a series of field-scale experiments were conducted. These experiments involved the injection of a tracer in the center a circular array of wells followed by either mixing using an engineered RPM flow system to invoke chaotic advection, or by natural processes (advection and diffusion) as the control. Pressure fluctuations from the mixing tests using the RPM flow system showed consistent peak amplitudes during injection and extraction at a frequency corresponding to the switching time, suggesting that the target hydraulic behaviors were achieved with the time-dependent flow field. The tracer breakthrough responses showed oscillatory behavior at all monitoring locations during the mixing tests which indicated that the desired RPM flow was generated. Comparisons to observations from a previous laboratory experiment using RPM flow, and the Fourier spectrum of the temporal tracer data suggested presence of chaos. Results from several quantitative metrics adopted to assess field-scale evidence of chaotic advection showed that mixing led to improved lateral tracer spreading and approximately uniform concentrations across the monitoring network. The multiple lines of evidence assembled in this proof-of-concept study suggested that chaotic advection can be engineered at the field scale. This investigation is a critical step in the development of chaotic advection as a viable and efficient approach to enhance reagent delivery.

---

[1] This chapter is from a paper that has been submitted for publication: Cho, M.S., Solano, F., Thomson, N.R., Trefry, M.G., Lester, D.R., Metcalfe, G. Field trials of chaotic advection to enhance reagent delivery. Ground Water Monitoring and Remediation. Submitted on November 30, 2018.

2.1 INTRODUCTION

In situ treatment typically involves the injection of a reagent into the subsurface to create a zone in which biological and/or chemical reactions lead to the destruction of contaminants. For example, electron acceptors and/or nutrients are used to create a thriving environment for indigenous microbes to biodegrade organic contaminants (Reinhard et al. 1997; Liebeg and Cutright 1999), while chemical oxidants are injected to destroy or transform a range of contaminants (Siegrist and Simpkin 2016). In either situation, the delivery of the reagent solution is a key requirement for the success of these *in situ* treatment systems; however, the design of an effective delivery system remains a significant challenge (Kitanidis and McCarty 2012).

Following the injection of a reagent solution into the subsurface, the desired chemical or biological transformations are initiated by transport processes that bring the injected reagent and contaminant together (Kitanidis and McCarty 2012). While this contact between the injected reagent and contaminant is the desired result of an effective delivery system, it can be one of the most difficult to achieve. In relevant literature, it is widely recognized that mixing is distinct to spreading. *Spreading* is associated with the deformation of a reagent plume providing additional opportunities for contact with the contaminant, while *mixing* (or dilution) is a result of various transport mechanisms (e.g., diffusion, sorption/desorption) that cause the reagent and contaminant to overlap, leading to a reduction in concentration variance toward a homogenous state (Kitanidis 1994; Jose and Cirpka 2004; Aref et al. 2017). This distinction is particularly important for heterogeneous porous media (Cushman and Tartakovsky 2017). While spreading increases the overall zone of contact between the reagent and contaminant, subsurface heterogeneities create preferential flow pathways over a range of spatial scales (Dagan 1986; Scheibe and Yabusaki 1998) that produce an uneven distribution of the injected reagent fluid. For conventional injection methods that use permanent or temporary vertical wells, the injected reagent will follow the path of least resistance from the wellbore into the porous medium, and the reagent distribution will be greater in areas of higher hydraulic conductivity (K) (Payne et al. 2008). Depending on the permeability contrast, perhaps due to the presence of small-scale structures in sedimentary deposits (e.g., bedding planes, laminations, joints etc.), the injected reagent may bypass adjacent regions of lower permeability (Saenton et al. 2002; Dagan and Neuman 2005; Zhong et al. 2011).

Ineffective reagent delivery in source zones can result in partial contaminant mass removal during *in situ* treatment. The remaining contaminant mass exists as immobilized, disconnected pockets/blobs that remain trapped in diffusion-controlled zones (Conrad et al. 1992), or in lower permeability zones where contact with the injected reagent is hindered by heterogeneity (Parker et al. 1994). In these zones, molecular diffusion ($D^* \sim 10^{-9}$ m^2/s) is likely the primary transport mechanism responsible for bringing the injected reagent and contaminant together (Jose and Cirpka 2004; Gale et al. 2015); however, diffusion is a slow process and contributes to inefficient mixing (Kitanidis and McCarty 2012). The remaining contaminant mass becomes a long-term source that can lead to eventual rebound and persistence of dissolved plumes downgradient of the source zone (Thomson et al. 2008).

In light of such phenomena, chaotic advection (Trefry et al. 2012; Aref et al. 2017) has the potential to improve reagent distribution in the subsurface and overcome preferential flow paths. Chaotic advection can be defined as the creation of "small-scale structures” caused by the repeated stretching and folding of fluid elements in a laminar flow regime (Ottino 1989; Aref et al. 2017) leading to stretching of material elements which is exponential in time. This rapid stretching of individual fluid elements creates highly complex, ramified particle trajectories, which have been theorized to improve the spatial distribution of solutes in porous media and to increase the contact area across which reactions can occur (Ottino 1989; Bagtzoglou and Oates 2007; Lester et al. 2009; Metcalfe et al. 2011; Mays and Neupauer 2012). Chaotic stirring creates fluid elements that are stretched out into long, thin filaments with a length scale sufficiently small for diffusion to promote efficient mixing (Aref et al. 2017). If chaotic advection can be invoked and controlled *in situ*, reagent delivery and treatment effectiveness may be significantly improved (Bagtzoglou and Oates 2007).

Aref (1984) was the first to show mathematically that chaotic advection can be achieved in a laminar flow regime by introducing time-dependent flow. Ottino (1989) concluded that since fluid particle trajectories in two-dimensional (2D) steady flows are fixed without intersection, there are no opportunities for mixing in such systems, and reported that periodic variation of flow is a key feature for invoking chaotic advection. Sposito (2006) observed fixed streamlines in a groundwater flow system and demonstrated that a time-dependent flow field is required to produce unsteady groundwater flows for enhanced mixing. Lester et al. (2009) introduced a configuration termed a rotated potential mixing (RPM) flow as an example of a time-dependent flow scheme capable of generating chaotic advection. A conventional RPM flow system involves periodically re-oriented dipole flow through the transient switching of pressures at a series of radial wells (Metcalfe et al. 2008), although other spatial configurations are possible. The RPM flow protocol assumes a completely closed flow system in which the fluid removed at the extraction well is immediately re-injected into the injection well (Trefry et al. 2012). In an RPM flow system, a dipole (i.e., one injection and one extraction well, separated by 180°) operates for a fixed time (t_p). The dipole is then instantaneously re-oriented by a reorientation angle (Θ) and resumes pumping for t_p. A repeated sequence of this periodic switching of dipole pumping may eventually cause the flow to become chaotic (Lester et al. 2009; Metcalfe et al. 2010a). Using an RPM flow system, it is possible to create either zones of enhanced mixing or confinement for increased residence time of reagents within the network of RPM flow injection/extraction wells (Trefry et al. 2012). The reorientation angle (Θ), pumping duration (t_p), and flow rate (Q) are the key parameters in an RPM flow system (Lester et al. 2010a; Metcalfe et al. 2010a). The actual mixing properties, chaotic or otherwise, of an RPM system can be selected by tuning the RPM parameters Θ, t_p, and Q.

Several studies have theoretically investigated chaotic advection in porous media. Trefry et al. (2012) showed that chaotic advection can be achieved in a synthetic aquifer system using an RPM flow protocol, and can withstand the impact of a local hydraulic gradient to produce both regions of enhanced mixing and confinement. This work also demonstrated that aquifer heterogeneities contribute to increased mixing of reagents; however, in a highly heterogeneous aquifer ($\sigma^2_{\ln K}$ >4), reduced duration of confinement was observed with the solute plume eventually moving outside the circular network of RPM flow injection/extraction wells. Sposito (2006) demonstrated that chaotic advection can be induced near a vertical recirculation well with time-dependent flow, leading to improved solute spreading. Bagtzoglou and Oates (2007) showed that a system of three wells, that oscillate between injection and extraction, with random time-dependent flow rates, can also achieve chaotic advection. Mays and Neupauer (2012) simulated an engineered sequence of injections and extractions to create time-dependent flow, and observed enhanced solute spreading by chaotic advection in a synthetic aquifer. Neupauer et al. (2014) reported that their engineered injection-extraction sequence combined with aquifer heterogeneities can improve spreading. Rodriguez-Escales et al. (2017) also used the engineered injection-extraction sequence reported by Mays and Neupauer (2012) in a numerical model, and demonstrated that chaotic advection increases the spreading of a reagent plume in a synthetic aquifer with a heterogeneous K field.

There have only been a few bench-scale experiments that have investigated chaotic advection in porous media. Metcalfe et al. (2010b) conducted an experiment in a Hele-Shaw cell flow to demonstrate chaotic flow behavior using a RPM flow system. Dipole pumping, consisting of one inlet and one outlet separated by 180° was operated for a specified duration (t_p), and then re-orientated by an angle Θ. Fluorescence images of the cell distinguishing injected and emplaced fluid were captured to visually illustrate evidence of chaotic advection that compared favorably with results from theoretical models (Lester et al. 2010a). Zhang et al. (2009) applied the oscillating well triplet reported by Bagtzoglou and Oates (2007) in a sand-packed flow cell with three inlet/outlet ports arranged in the shape of an equilateral triangle. To invoke chaotic advection, an oscillating flow scheme was used which involved periodic variations of flow rate and direction at each port every ~8 minutes. In the constant flow scheme (control), the flow rate and direction at the ports were held constant for the experiment duration. Digital image analysis of colorimetric and fluorescent dyes inside the flow cell indicated that the oscillating flow scheme led to enhanced solute spreading and confinement in comparison to the constant flow scheme. Nissan et al. (2017) used time-dependent flows through a sand-packed column to investigate the transport behavior of a conservative tracer under fully saturated conditions. Their experimental observations combined with modeling results showed that time-dependent flows increased tracer spreading and residence time inside the column (albeit the term chaotic advection was not used).

The established theoretical underpinnings and observations from bench-scale experiments strongly suggest that chaotic advection has the potential to significantly enhance reagent mixing at the field scale. Thus, the underlying motivation for this research effort was to extend this foundational work and investigate if chaotic advection can be invoked in a natural aquifer system. To test this hypothesis, a series of field-scale solute tracer experiments were performed. Each tracer experiment consisted of an initial injection of a pre-determined tracer volume in the center of a circular array of injection/extraction wells followed by the activation of an RPM flow protocol. While there are published quantitative methods (e.g., Poincaré sections, Lyapunov exponents, Melnikov functions, etc.) that can be used to indicate the presence of chaotic advection at the theoretical scale using individual fluid particle trajectories over time and space

(Ottino 1990), these methods cannot readily be applied using the spatial and temporal resolution of typical field data collected. As a result, alternative quantitative metrics were developed to demonstrate the presence of chaotic advection and its impact on mixing using the data collected. To the best of our knowledge, this is the first attempt to investigate aspects of chaotic advection at the field scale. The findings from this proof-of-concept study represent a critical step in the development of a novel method that can be used to improve the effectiveness of *in situ* treatment technologies.

2.2 METHODS

2.2.1 Site Description

This investigation was performed in an experimental gate located in the sandpit area at the University of Waterloo Groundwater Research Facility at the Canadian Forces Base (CFB) in Borden, ON, Canada. The gate was 8 m wide by 11 m long and hydraulically isolated on two sides by hanging sheet pilings driven down to ~2 m below ground surface (bgs). The other two sides have ~2.5 m wide openings in the center that allow groundwater to flow through the cell controlled by the local horizontal hydraulic gradient in the upper 2 m of the aquifer.

The unconfined Borden aquifer at this location is composed primarily of unconsolidated fine to medium-grained well-sorted sand (porosity of 0.33, specific storage of $1x10^{-3}$ /m, and hydraulic conductivity from $6.0x10^{-6}$ to $2.0x10^{-4}$ m/s) that extends ~9 m in thickness and underlain by a clayey and sandy silt aquitard. Some microscale heterogeneities are present in the form of silty sand and coarse sand lenses. The vertical hydraulic conductivity is approximately one third of the horizontal conductivity. The water table varies seasonally but is typically located at ~1 m bgs. The annual average hydraulic gradient is estimated to be ~0.0043 m/m (Mackay et al. 1986; Sudicky 1986).

2.2.2 Dipole Pumping System

For the RPM flow system, eight (8) injection/extraction (IE) wells (identified as IE-1 to IE-8) were installed in a circular network with an approximate diameter of 1.75 m in the middle of the gate (Figure 2.1). In addition to the IE wells, one additional well (identified as IW) was installed at the center of the circular network for injection of a conservative tracer solution. All boreholes were advanced using a direct-push method (Geoprobe® 7720DT) to a depth of ~2 m bgs. While the casing was pulled back to surface, sand was allowed to collapse around the 5.1 cm diameter well (schedule 40 PVC). Each injection/extraction well was screened (2.5 mm slot) from 0.75 to 1.75 m bgs. All wells were developed after installation.

Sequential dipole pumping was performed by an above-ground injection/extraction system (Figure A-1) that consisted of sixteen (16) solenoid valves (ASCO Red-Hat 8210G002 120/60, 110/50) connected to a peristaltic pump (MasterFlex, 7549-32 with MasterFlex, 7019-43 pump head) and a programmable logic controller (PLC) unit (Allen-Bradley 1760-L18AWA-EX ser. B with 1760-IA12XOW6I ser. A expansion). Check valves were attached to the end of each solenoid valve to avoid potential clogging and malfunction since solenoid valves are one-directional and may not be able to withstand backpressure from pumping. Dedicated PVC tubing was connected to the respective solenoid valve pair and placed in each IE well. The end of each PVC tube (~10 cm in length) was prepared with 3.9 mm holes and wrapped with 125 µm Nitex® screen.

2.2.3 Monitoring Infrastructure

To monitor the groundwater tracer concentration, 17 multi-level wells (MLs) were installed within the circular array of IE (Figure 2.1). Each ML was constructed from a 1.3 cm CPVC pipe (center stalk) and equipped with two sampling locations, at nominal depths of 1.0 m and 1.5 m bgs. At each sampling location, a length of 0.6 cm OD PTFE tubing was cut and fixed onto the center stalk with 10 cm of the tubing slotted and wrapped with 200 µm Nitex® screen. The ML located in the center was identified as C1, the MLs within the middle region of the circular array were identified as M1 to M4, and the MLs nearest the IE wells were identified as O1 to O12. The shallow and deep sampling locations at each ML are denoted by the suffix -S and -D respectively.

Five dipole resistivity probes (DRPs) were attached to the center stalk of ML C1, and M1 to M4 (0.65, 1.0, 1.25, 1.5 and 1.85 m bgs), and four DRPs were attached to the center stalk of ML O1 to O12 (0.65, 1.1, 1.45 and 1.85 m bgs). The DRPs are identified by the associated ML name and a numerical suffix that increases with depth (e.g., C-1 to C-5, see Figure 2.1(b)). Each DRP was constructed by pulling a stainless steel cable through holes on a PVC pipe to create two exposed wires. When immersed in fluid, the DRP has the capability of providing a reading, R_s, that indicates the electrical resistance of the fluid between the two detector wires (Stevenson et al.

2018). Each DRP was connected to a multiplexer (Campbell Scientific, AM16/32B) and datalogger (Campbell Scientific, CR 1000). Output from the data logger represents a dimensionless value, *X,* that reflects the relative magnitude of resistance as given by

$$X(-) = \frac{R_f}{R_s + R_f} \tag{2.1}$$

where R_f is a constant resistance in the data logger circuit, and R_s is the variable resistance sensed. This relative resistivity can be correlated to local electrical conductivity (EC) if sufficient local EC data is available for probe calibration. As the ionic concentration increases in the pore fluid, values of EC increase resulting in a higher value for *X*. Responses were collected from all 73 depth-specific DRPs at 1-minute intervals. For details on the DRP used, see Stevenson et al. (2018).

A submersible datalogger (CTD Diver, Van Essen Instruments, Kitchener, ON) was placed in each IE well (8 in total), and programmed to take records of pressure, temperature and EC every minute. All pressure transducer readings were barometrically corrected. A flow meter (Assured Automation, WM-PC-050) was dedicated to each dipole (8 in total), and recorded the cumulative volume of groundwater pumped from the extraction to injection well over the entire test duration.

2.2.4 Experimental Approach

Over the course of two field seasons, a total of 12 tracer tests were conducted. Each tracer test consisted of an injection, equilibrium, mixing and extraction phase. The injection phase was used to consistently place a known volume of conservative tracer (NaCl) in the center of the circular array of IE wells. An injection volume of 430 L was selected to achieve the desired coverage within the monitoring network (assuming 60% internal coverage of the circular well network area, 1 m deep corresponding to the well screen length, and porosity of 0.33). The tracer concentration was 10 g/L, and deemed to be a representative reagent concentration (Siegrist and Simpkin 2016) that was high enough to be detected easily by the monitoring tools employed. The tracer solution was delivered into the center injection well (IW) at a rate of ~3.5 L/min using a peristaltic pump (Cole-Parmer, Masterflex® 7549-32 with Masterflex® 7019-43 pump head). Following tracer injection, the equilibrium phase consisted of a 24-hour period to allow sufficient time for the pressure changes resulting from the tracer injection to subside.

After this equilibrium period, an RPM flow protocol was initiated (mixing phase) using the above-ground dipole pumping system where each IE well pair was operated for a specified t_p at Q_{RPM}. After duration t_p, the active dipole was turned off (i.e., valves closed) and re-oriented by the reorientation angle (Θ) before pumping resumed at the new dipole for the same specified t_p and Q_{RPM}. This sequential, transient dipole pumping was repeated around the IE well network for 6 to 7 days. After the mixing phase was completed, the tracer solution was extracted from IW using a peristaltic pump at a flow rate of ~2.0 L/min until responses from all 73 DRPs returned to baseline conditions.

Control tracer tests were performed in an identical manner as described above except for the mixing phase where the injected tracer solution was allowed to mix by natural processes (i.e., advection and diffusion) without any engineered intervention (identified as the natural mixing phase). The observations from the initial control tests conducted using a tracer concentration of 10 g/L suggested that density-driven advection was occurring. As a result, additional control tracer tests were conducted using a tracer solution with a concentration of 1 g/L.

Groundwater sampling was performed at all MLs (34) and IE wells (8) during each tracer test. Sampling events were conducted at various times during the test phases, including: before/after injection, after equilibrium, and before/during/after implementation of the RPM flow system. Each sampling round was completed within 30 to 45 minutes using a peristaltic pump (Geotech Environmental Equipment Inc., Geopump™ series II equipped with easy-load II® pump head). Prior to sample collection, at least one full tubing volume was purged from each location. EC and temperature were measured in the field (Thermo™ Scientific Orion™ 4-Star, equipped with Orion™ 013605MD conductivity cell). Samples were collected in 20 mL glass vials and transported to the University of Waterloo Soil and Groundwater Remediation Laboratory prior to analysis for chloride (Cl^-) using an ion chromatograph (IC) (Thermo™ Scientific Dionex™ ICS-1100, equipped with a Dionex AS-DV; method detection limit (MDL) of 0.073 mg/L). Standards and blanks were included with each IC run for QA/QC purposes.

2.2.5 Resistivity Probe Sensitivity and Calibration

To evaluate the sensitivity of the DRPs to tracer concentrations, a laboratory column experiment and field calibration tests were performed. The data from the laboratory and field efforts were also used for the generation of calibration curves to: (1) determine whether the DRP responses collected from the tracer tests were representative of *in situ* tracer concentrations, and (2) convert DRP responses to equivalent concentrations of Cl^- for mass balance considerations.

The objective of the column experiment was to compare the sensitivity of three similarly constructed DRPs to various tracer concentrations, and to compare actual DRP responses to their theoretical behavior. The column experiment was conducted in a 30 cm long plexiglass column (diameter 15.2 cm) with inlet and outlet ports at each end. The column was packed homogeneously with dry aquifer material from CFB Borden. During packing, three DRPs were placed directly in the sand at ~5 cm from the bottom of the column. The DRPs were arranged in the shape of a triangle in the center of the column (plan view) with similar separation distances between the probes. Each DRP was connected to a multiplexer (Campbell Scientific, AM16/32B) and datalogger (Campbell Scientific, CR 1000). The column was then saturated with deionized water using a peristaltic pump (Cole-Parmer, Masterflex® L/S 7551-30) connected to the inlet port to permit flow through the column. The response of the DRPs was evaluated for varying concentrations (0.01, 0.1, 0.5, 1.0, 5.0, and 10 g/L) of sodium chloride (NaCl, reagent grade) in the inlet solution. These levels reflect the anticipated range of concentrations that might be observed during the field tracer test using an injection solution concentration of 10 g/L. DRP responses were collected from all three probes at 1-minute intervals. The EC (mS/cm) in the column effluent was monitored using an EC meter (Thermo™ Scientific Orion™ 4-Star, equipped with Orion™ 013605MD conductivity cell). Once steady-state conditions were reached, the injected tracer solution was switched to the next higher concentration.

Field calibration was performed by injecting a known volume of NaCl solution into select ML locations and observing the response from the DRP at the corresponding depth. Four different concentrations of tracer solution (0.5, 1.0, 5.0, and 10 g/L), representative of the expected concentration range likely to be observed during the tracer tests, were prepared using 1 L of groundwater extracted from a nearby well. For each concentration, the EC (mS/cm) of the tracer solution was measured prior to injection. The tracer solution was delivered using a peristaltic pump (Geotech Environmental Equipment Inc., Geopump™ series II equipped with easy-load II® pump head) at a rate of ~1 L/min. DRP readings were recorded every 2 minutes until steady-state conditions were observed. The injection was then repeated for the next tracer concentration (from low to high concentration). At the end of the calibration test, groundwater was extracted from the ML well until a DRP response representative of background conditions was obtained.

2.2.6 Data Analysis

The published quantitative methods that have been used to indicate the presence of chaotic advection (Ottino 1990) involve tracking positions of individual passive fluid tracer particles over space and time. Studies of bench-scale experiments have reported the use of various analytical techniques based on images obtained from their experimental set-up (Zhang et al. 2009; Metcalfe et al. 2010b) to indicate the presence of chaotic advection. Unfortunately, it is not feasible to apply these methods using the spatial and temporal resolution of data collected in this field investigation. As a result, alternative quantitative metrics were developed to investigate the presence of chaotic advection and its impact on mixing. In this study, chaotic advection was presumed to be occurring if enhanced spatial distribution of the tracer (spreading) and reduced concentration variance (mixing) were observed within the monitoring network (Kitanidis 1994; Zhang et al. 2009). This assumption is based on the understanding that the small-scale structures resulting from chaotic advection can manifest as both enhanced spreading and mixing at the field scale (Ottino 1990; Mays and Neupauer 2012; Aref et al. 2017).

Data analysis was performed using the DRP responses collected, which were treated as proxy measures of tracer concentrations (denoted by C^*; evidence provided below). To assess the impact of chaotic advection on tracer mixing, the following quantitative metrics were used: integrated volume under the three-dimensional (3D) contours of DRP responses, variance of tracer concentrations ($s^2_{C^*}$), spatial tracer concentration gradients ($\Delta C^*/\Delta r$), and the first two integral or spatial moments of the tracer concentration distribution.

Prior to data analysis, the DRP responses were smoothed using a central averaging algorithm where the DRP response reported at a given time is the moving window average of the 20 nearby observations (10 observations on either side of the time point). This data-smoothing step was sufficient to reduce the minor signal noise present in the DRP responses. Smoothed values of the DRP responses were either imported directly or converted to an equivalent Cl^- concentration (C^*) and then imported into Tecplot 360 (Tecplot Inc., Bellevue, Washington, USA) for visualization and analysis. 3D contours of the DRP responses or C^* were generated by using the inverse distance weighting scheme (exponent of 3.5, and 8 neighboring data points distributed as evenly as possible throughout the surrounding 8 octants) to interpolate the observed DRP responses (or C^*) gathered at the 73 locations to a uniform grid with a spatial interval of 0.06 m. The origin was assigned to the center of the screened portion of IW with the x direction corresponding to the groundwater flow direction, the y direction transverse to the groundwater flow direction (see Figure 2.1(a)), and the z direction coincident with the middle of IW (positive upwards).

For selected times during a tracer test, the Tecplot 360 built-in integration tool was used to estimate the total volume under the 3D DRP response distribution for values of a DRP response greater than background levels (X >0.05). Enhanced spreading of the tracer is expected to manifest as an increase in the spatial volume that the tracer plume occupies as captured by the monitoring network.

The spatial concentration variance ($s_{C^*}^2$), as represented by the DRP responses, can be used to quantify the degree of mixing in a system (Kapoor and Kitanidis 1998; Pannone and Kitanidis 2001; Cushman and Tartakovsky 2017). The spatial variance of C^* is a measure of mixing that describes the variability across the concentration field (Cushman and Tartakovsky 2017). As the system becomes well-mixed and uniform concentrations are achieved across the monitoring network, $s_{C^*}^2$ is expected to approach zero (Sposito 1998), which corresponds to the homogeneous state. To estimate the average equivalent Cl^- response ($\overline{C}^*$) and $s_{C^*}^2$, the Cl^- concentration field was reconstructed from the C^* values estimated at the 73 DRP locations.

Horizontal spatial gradients ($\Delta C^*/\Delta r$) in the radial direction were approximated by dividing the change in equivalent Cl^- response (ΔC^*) between the probe closest to the injection well (C1) and another probe within the monitoring network by the distance between the probe locations (Δr). Prior to the start of the RPM flow system, a relatively large difference in the equivalent Cl^- response between the probe closest to the injection well (C1) and those more distal is expected, as most of the tracer mass resides in the vicinity of IW. As mixing progresses, a decrease in the horizontal spatial gradients would suggest smaller differences in the equivalent Cl^- responses between two probe locations resulting from uniform concentrations across the monitoring network consistent with a decrease of $s_{C^*}^2$.

The first spatial moment of a tracer concentration distribution represents the mean location of the centroid of the tracer mass, and the second spatial moment provides an estimate of the degree of spreading around the centroid (Kitanidis 1988; Le Borgne et al. 2010). To estimate these spatial moments, the interpolated equivalent Cl$^-$ responses were exported from Tecplot 360 and processed. Due to the nature of the RPM flow, it is expected that as mixing proceeds, the centroid ($\bar{x}_c$, $\bar{y}_c$, $\bar{z}_c$) of the tracer distribution would remain near the center of the screened portion of the IW (the origin), and that increases in the second moment (s_x^2, s_y^2, s_z^2) would be indicative of an enlarged tracer spatial distribution within the monitoring network. In contrast, for the control tracer tests subjected to ambient advection and diffusion, the location of the centroid of the tracer mass is expected to be controlled by the local groundwater velocity, and spreading, as captured by the second moment would be minimal.

2.3 RESULTS AND DISCUSSION

A total of eight (8) mixing and four (4) control tracer tests were performed over two field seasons (Table 2.1). Some of these tracer tests were, unfortunately, influenced by: (1) high intensity precipitation events (thunderstorms) that resulted in rapid pressure increases in the aquifer and in some cases also power outages; (2) minor equipment malfunctions which impacted the operation of the dipole pumping system and data collection efforts; and, (3) an unseasonably low water table that impacted the consistency between the various tracer tests. The water table location varied from 0.3 to 0.9 m bgs (average of 0.6 m bgs) over the two field seasons. For illustrative purposes in this paper, we primarily present and discuss results from one mixing (RPM45-A) and one control (CTR1-A) tracer test (Table 2.1). The mixing phase of the RPM45-A tracer test was 168 hours long and involved 21 cycles with a re-orientation angle of $\Theta = 45°$, pumping rate of Q ~2 L/min, and duration of $t_P = 1$ hour. The natural mixing phase of the CTR1-A tracer test lasted for 121 hours. Data from tracer test RPM135-A and RPM45-B (same methods as RPM45-A) are shown in Appendices B and C, respectively.

2.3.1 Hydraulic Response during RPM flow

Figure 2.2 shows the pressure change relative to baseline conditions for each dipole well during the mixing phase for the RPM45-A tracer test. A positive pressure change implies that water was being injected into the well, while a negative pressure change implies that water was being extracted from the well. During this tracer test, a rainfall event (~10 mm) began ~36 hours into the test and resulted in a slight overall rise in the water pressure relative to the baseline pressure.

Despite some minor pressure inconsistencies at early time (< 18 hours), the dipole system operated as expected with one IE well pair pumping for one hour before switching to the next pair. The frequency of the peak pressure changes corresponds to the switching time (t_p of 1 hour) associated with the dipole pumping system which, for this test, was determined from the theoretical work of Lester et al. (2010a). After ~18 hours, a consistent peak amplitude change is observed for six of the eight dipoles, with peak pressure changes ranging from 41 to 92 cm during injection, and -38 to -18 cm during extraction. As expected, the pressure changes during extraction are less than those observed during injection for shallow wells in an unconfined aquifer (Freeze and Cherry 1979). Pressure changes are also observed at the wells located ~0.7 m on either side of the active IE wells, with pressures approximately an order of magnitude less than those observed at the active dipole wells. Minor fluctuations in pressure (≤0.5 cm) are observed at wells furthest away from the active IE wells.

The only exception is the hydraulic response at IE-4 (Figure 2.2(d)) where the maximum and minimum amplitudes are suppressed relative to those observed in the other IE wells, and the pressure does not return to near baseline levels when this well is inactive. This behavior is suspected to be the result of a solenoid value associated with IE-4 being clogged with sediment, and hence remained partially open. The maximum increase in pressure (~90 cm) during injection at IE-1 and IE-2 is greater than that observed at the other wells, and is likely reflective of a slightly lower hydraulic conductivity at these locations. The anomalous pressure change of >1 m observed at 46 hours at IE-2 (Figure 2.2(b)) is suspected to be the result of a temporary clog in the dipole pumping system. At ~30 hours, a double peak at IE-1 and IE-5 is observed without the expected 4-hour time delay, and then at ~120 hours this double peak is observed at IE-1 and IE-5, and IE-2 and IE-6 (Figure 2.2(a, b)). Both of these discrepancies in timing are likely a result of a short power outage and subsequent restart of the system.

In comparison to this mixing tracer test, minor pressure changes are observed during the CTR1-A test (Figure A-2) as expected. A slight pressure change with a ~ 24-hour frequency is assumed to be a result of water uptake by vegetation (grasses) during daylight hours. This pressure change is most noticeable for ~8 hours of the 24-hour cycle (Figure A-2) that corresponds to a period of time (11:00 am to 7:00 pm) when maximum root adsorption is expected (Ritchie 1974; Freeze and Cherry 1979). A rainfall event (~5 mm) that began at ~100 hours into the test was responsible for the small increase in observed pressure at this time. Aside from these minor perturbations, the pressure changes remain constant for the entire duration of the CTR1-A tracer test.

The trends in hydraulic response for the other tests performed (e.g., see Appendix B and C) are consistent with the behavior observed during the RPM45-A and CTR1-A tracer tests. Pressure changes during the RPM135-A test (Appendix B) show one active IE well pair pumping for one hour before switching to the next pair located 135° apart. Consistent peak amplitudes are observed for six of the eight dipoles with pressure changes ranging from 38 to 94 cm during injection, and -30 to -19 cm during extraction at a frequency corresponding to the switching time of 1 hour. At the wells on either side of the injection/extraction wells, pressure changes are approximately an order of magnitude less than those observed at the active dipole wells. Minor fluctuations in pressure (≤0.5 cm) are observed at wells furthest away from the active IE wells. The suppressed pressure changes observed at IE-4 during the RPM45-A test is also apparent during the RPM135-A tracer test.

While one pumping well (IE-4) did not operate as expected, the resultant flow field is still time-dependent and therefore capable of generating chaotic advection (Aref 1984; Ottino 1989). At a minimum, two dipoles are needed to achieve temporally varying flow through periodic switching. Thus, the transient hydraulic requirements for the target RPM flow were satisfied in the RPM45-A and other tracer tests, with three dipoles undergoing periodic switching for about 170 hours.

2.3.2 DRP Calibration and Proxy for Tracer Concentration

The steady-state DRP responses from each of the three probes used in the column experiment and the observed effluent EC (mS/cm) are shown on Figure A-3. The similar response observed from all three DRPs confirms that the probes used in the column experiment are similar in construction. The observed relationship is linear at lower EC values and becomes non-linear as EC increases, which is consistent with the theoretical work of Stevenson et al. (2018). These data suggest that the DRPs placed in a flow-through column packed with Borden sand are sensitive over the range of tracer concentrations used in the field tracer tests, and produced responses that are representative of the tracer concentration in this column system. For the field calibration effort, an average of five steady-state DRP responses over a 10-minute interval from each probe was used in conjunction with the EC of the injected tracer solution to evaluate DRP behavior (e.g., see Figure A-4). As expected, the best-fit relationship was determined to be non-linear (r^2 ~0.91) over the range of tracer concentrations used (0.5 to 20 g/L). This suggests that these DRPs are able to capture steady-state responses that are representative of changes in *in situ* tracer concentrations over the range explored. Similar relationships were obtained for all ML wells investigated during the field calibration effort (data not shown).

Cl^- concentration and EC data from groundwater samples collected for all tracer tests performed were pooled (Figure A-5). The resulting best-fit relationship was linear (r^2 ~0.98), clearly indicating that either EC (mS/cm) or Cl^- concentration (mg/L) could be used interchangeably in this investigation. As a result, scatterplots of DRP responses versus Cl^- concentrations from groundwater samples collected from an associated ML sampler were prepared for each probe location to evaluate the ability of each DRP to provide a continuous response representative of *in situ* tracer concentrations (e.g., see Figure 2.3). Each scatterplot (34 in total) represents a pooled data set from the manual sampling events conducted at various times during both the mixing and control tracer tests. Cl^- concentrations < 1000 mg/L were detected at most of the shallow (-S) MLs (located 1.0 m bgs) with respective DRP responses showing a linear trend at this lower range of EC or Cl^- concentration. The deep (-D) MLs (located 1.5 m bgs) yielded Cl^- concentrations ranging from 150 to 14,000 mg/L, and the best-fit DRP relationship was non-linear (Stevenson et al. 2018). Eight (8) out of the 34 (24%) scatterplots analyzed produced r^2 values ≤0.70 (O1-D/O1-3, O2-S/O2-2, O6-D/O6-3, O10-D/O10-3, O12-D/O12-3, M1-S/M1-2, M2-S/M2-2, and M3-S/M3-2) suggestive of a poorer representation by the DRP response of *in situ* concentrations Of these eight locations, the observed Cl^- concentrations at seven were < 1000 mg/L, suggesting that perhaps the DRPs were not sensitive at lower Cl^- concentrations, which is inconsistent with the laboratory and field calibration findings. An alternative explanation may be the presence of local interference between the probe and the corresponding ML that resulted in an unacceptable correlation. For the remaining 26 DRPs, similar best-fit regression coefficients were determined indicating consistency in the DRP responses for the range of Cl^- concentrations observed across all tracer tests.

This calibration and comparison effort demonstrated that the DRP responses can be treated as a proxy for *in situ* Cl^- concentrations in this investigation. The ability of these DRPs to collect high-resolution temporal and spatial information that can be converted to equivalent Cl^- concentrations is essential for the assessment of chaotic advection discussed below.

2.3.3 Probe Responses and Quantitative Evidence of Chaotic Advection

The DRP response breakthrough curves (BTC) from two locations (C1 and O6 at all depths) for the RPM45-A tracer test (Figure 2.4) reveal an oscillatory behavior that is similar to the BTCs observed in a previous laboratory experiment using RPM flow in a porous medium and is a necessary precursor to chaotic advection (Lester et al. 2010b). The periodic switching in the RPM flow system leads to stretching and spreading of the tracer plume which is detected at the probes as subharmonic oscillations of DRP responses as the tracer mass moves in and out of the vicinity of each probe in response to dipole pumping. A Fourier transform of the temporal DRP responses at these two probe locations does not reveal distinguishable dominant frequencies, but rather a continuous series of many broad, smaller peaks that persist across the frequency spectrum (Figure A-6). This observation supports the presence of chaos given that a chaotic signal has many different frequency components that produces a continuous spectrum of frequencies rather than a few narrow peaks or “spikes” (Moon 2008). While results from all DRPs at C1 and O6 are presented for illustration (Figure A-6), similar frequency domain trends were observed for all DRPs at the other 15 locations (data not shown). Collectively, these results are consistent with the generation of chaotic advection as a result of the imposed RPM flow.

At the probes adjacent to IW (C1), DRP responses at all depths are initially ~0.3 to 0.4 after injection (*t* = 0 on Figure 2.4) and decline in an oscillating manner to values <0.1 within ~60 hours of mixing. This suggests that the tracer solution moves beyond the vicinity of the injection well towards the outer probes in the monitoring network during this time. At the DRPs at O6, located ~0.7 m from IW, responses at all depths are initially at background levels (<0.02), and then the O6-2, O6-3 and O6-4 DRPs increase to a maximum of 0.10 within 30 hours of mixing before they decrease in a step-wise response to the RPM flow system. In contrast, the BTCs at the same two monitoring locations (C1 and O6) for the CTR1-A tracer test (Figure A-7) are essentially flat during the first ~100 hours of the natural mixing phase at all depths with only minor fluctuations. At location C1, the DRP responses remain at a value of ~0.10 for all depths corresponding to levels observed following tracer injection, while a background level of 0.02 persists at all depths at location O6. The DRP responses at locations M3 and M4 also remain close to 0.10 for the duration of the natural mixing phase, while the DRP responses at locations M1 and M2 were ~0.10 for the first approximately 40 hours before they started to decrease (data not shown). After ~100 hours into the natural mixing phase, the response of the DRPs at locations O7, O8 and O9 started to increase from background levels (data not shown). The slight decrease in DRP response at locations M1 and M2, and increase at locations O7, O8 and O9 is reflective of a shift in tracer mass as a result of ambient groundwater flow through the gate. Aside from this minor displacement, the majority of the tracer mass remains near IW during the natural mixing phase. Note that the difference in the range of values observed in the DRP responses during the RPM45-A and CTR1-A tracer tests is a result of the lower concentration of the injected tracer solution used in the CTR1-A tracer test (i.e., 1 g/L compared to the 10 g/L used in the RPM45-A tracer test). This discrepancy does not affect our ability to extract the critical trends and overall behavior between the mixing and control tracer tests. Similar trends were observed in the BTCs of DRP responses at all probe locations and depths for both the RPM45-A and CTR1-A tests (data not shown).

One expected consequence of enhanced mixing by chaotic advection is a more homogeneous spatial distribution of the tracer in the zone of interest. In this study, enhanced mixing would correspond to observations within a smaller range of DRP responses over all of the probe locations within the monitoring network. At the end of the injection phase, the tracer plume (as captured by the DRP response contours) is observed within the immediate vicinity of IW where the highest values of DRP responses occur (Figure 2.5(a)). As sequential dipole pumping is repeated during RPM flow, the tracer plume appears to undergo spreading (Figure 2.5(b-d)). By the end of the mixing phase at 7 days, the varying levels of DRP responses present at the end of the injection phase are no longer evident, and DRP responses less than 0.08 are observed across the entire monitoring network (data not shown). In contrast, the DRP response contours for the CTR1-A tracer test (Figure 2.6) shows minimal movement of the tracer throughout the natural mixing phase. The slight skew of the tracer mass in the positive *x*-direction in all the panels (~29 cm over 4 days) is a result of the ambient groundwater flow through the gate (Figure 2.1(a)). Aside from this shift of tracer mass, the magnitude of DRP responses as well as the spatial extent of the tracer plume appear to be steady throughout the 5-day duration of this test.

The normalized volume of the tracer plume for the RPM45-A tracer test (Figure 2.7(a)) increases steadily during the mixing phase, and by ~60 hours reaches a value of ~1.7 indicating that the volume occupied by the tracer (for $X > 0.05$, equivalent to approximately 250 mg/L) increased by 70%. In comparison, the normalized volume of the tracer plume during the CTR1-A tracer test remains near unity for the first 60 hours of the natural mixing phase (Figure 2.7(a)). These results suggest that dipole pumping leads to an increase in the volume occupied by the tracer plume within the monitoring network, and that enhanced tracer spreading was generated by the RPM flow system. A slight decrease in the normalized volume estimated at early times during the RPM45-A tracer test is likely due to a small portion of the tracer mass (5 to 10%) that was detected at the IE wells at relatively low concentrations (Figure A-8). An analysis of the observed BTCs from all IE wells indicated that this small portion of the total tracer mass captured at the extraction wells is recirculated between the IE wells for the remainder of the mixing phase, but had minimal impact on the tracer behavior observed at the DRP locations. The results of this analysis also showed that there was little to no change in the overall trends and behavior after ~60 hours of mixing, which suggest that quasi steady-state conditions are established by this time. Thus, the subsequent discussion is focused on the results of various quantitative metrics using the equivalent Cl^- responses over the first 60 hours of the mixing phase.

Spreading provides a description of the spatial extent of the tracer plume using average concentrations rather than its distribution within the plume (Cushman and Tartakovsky 2017). Based on the potential for chaotic advection to enhance both spreading and mixing, concentration variance ($s_{C^*}^2$) was used as an indicator of the degree of mixing (Kitanidis 1994; Kapoor and Kitanidis 1998; Dentz et al. 2011; Le Borgne et al. 2011). Normalized values of $s_{C^*}^2$ during the RPM45-A tracer test (Figure 2.7(b)) begin to decrease from unity starting at ~16 hours towards a value close to 0.2 after ~60 hours of RPM flow. This suggests that the RPM flow system promotes enhanced mixing of the tracer which leads to uniform DRP values being achieved across the monitoring network. This interpretation is consistent with the behavior expected from a well-mixed system that produces a similar range of concentrations within the tracer plume that leads to a $s_{C^*}^2$ value of zero (Sposito 1998). Conversely, the normalized values of $s_{C^*}^2$ during the CTR1-A tracer test (Figure 2.7(b)) remain near unity for the first 60 hours of the natural mixing phase, indicating high variability in the DRP responses within the tracer plume as represented by 3D contours of DRP responses (Figure 2.6). The results from the CTR1-A tracer test suggest that while the tracer plume undergoes some spreading by the ambient groundwater flow through the gate, limited mixing mechanisms are present.

All normalized spatial gradients associated with the RPM45-A tracer test (Figure 2.8(a)) which begin at unity show a dramatic decline towards a final $|\Delta C^{*}/\Delta r|$ value of <0.1. Despite some fluctuations in the data, the final $|\Delta C^{*}/\Delta r|$ values appear to occur within ~60 hours of operation of the RPM flow. This suggests that by ~60 hours, similar values of equivalent Cl^{-} responses are observed between the probes closest to IW (C1) and some outer probe locations for all depths. This is attributed to a uniform tracer distribution resulting from mixing of the tracer mass across the monitoring network. During the CTR1-A tracer test (Figure 2.8(b)), the normalized $|\Delta C^{*}/\Delta r|$ values remain near unity for the first 60 hours, suggesting that the same initial differences in the equivalent Cl^{-} responses observed between the probes at C1 and the outer probes at the beginning of the natural mixing phase persists. This interpretation is consistent with the visual observations from the BTCs (Figure A-7) and the plume contours (Figure 2.6) that suggest that the tracer mass remains near IW during the natural mixing phase.

After 60 hours of mixing, the center of the tracer mass ($\bar{x}_c$, $\bar{y}_c$, $\bar{z}_c$) during the RPM45-A tracer test, as estimated from the first spatial moment, had moved 1 cm in the direction of groundwater flow, 3 cm transverse to the groundwater flow direction, and risen 5 cm in the vertical direction indicating that the tracer distribution remained near the center of the screened portion of IW as expected. By the end of the mixing phase for the RPM45-A tracer test (at 168 hours), the center of tracer mass had moved -2 cm in the direction of groundwater flow, 13 cm transverse to groundwater flow, and risen 17 cm. Despite using a tracer concentration of 10 g/L, the RPM flow system was apparently able to overcome the expected density-driven advection behavior based on these moment estimates. In comparison, at the end of natural mixing phase for the CTR1-A tracer test (at 120 hours), the center of tracer mass had moved 29 cm in the direction of groundwater flow, -5 cm transverse to groundwater flow, and sank 6 cm in the vertical direction. The displacement in the x-direction is a direct result of tracer transport by the ambient groundwater flow through the gate as discussed above.

During the RPM45-A tracer test, the degree of spreading around the centroid, as estimated by the second spatial moments, fluctuates in all directions before increasing non-linearly at ~24 hours and then remaining at normalized values of >1.5 after ~60 hours of mixing (Figure 2.9(a)). While a formal error analysis of these second moment estimates is not possible, we have set arbitrary uncertainty bounds of ±20% implying that values outside of this envelope are likely representative of changes in the second moment. This result suggests that the complex flow field produced by the RPM flow system leads to enhanced lateral and vertical spreading of the tracer plume within the monitoring network. In comparison, the values of normalized variance in all directions around the center of tracer mass during the CTR1-A tracer test (Figure 2.9(b)) remain relatively flat (< ±20%) over the first 60 hours.

The DRP response BTCs and results from the corresponding spectral analysis using Fourier transformations suggest that it is possible to produce engineered chaos in the subsurface using an RPM flow system. Quantitative analysis of DRP (and equivalent Cl^-) responses from the mixing and control tracer tests suggests that this chaotic behavior of the flow field leads to enhanced tracer spreading and mixing in comparison to the control. The mixing test using an RPM flow system led to a more even spatial distribution of the tracer, and uniform equivalent Cl^- values were established within the monitoring network within the first 60 hours. Despite a small portion of the tracer mass being captured at early times and subsequently recirculated by the IE wells, the trends in the results and tracer behavior remain consistent at all probe locations for the quantitative metrics employed. While only one representative mixing (RPM45-A) tracer test and the control (CTR1-A) tracer test were presented for discussion, similar behavior was observed for the other mixing tests performed (e.g., see Appendix B and C).

2.3.4 Impact of RPM Flow Reorientation Angle on Mixing

The DRP response BTCs for the mixing test with a reorientation angle of 135° (Appendix B) show similar oscillatory behaviors as observed in the other tracer tests using an RPM flow system. The 3D contours of DRP responses (Appendix B) also show a similar evolution of tracer movement. Despite some minor differences between the data sets, the normalized integrated volume (Figure 2.7(a)), concentration variance (Figure 2.7(b)), spatial gradients (Figure 2.8(c)), and second spatial moments around the tracer mass centroid (Figure 2.9(c)) associated with the RPM135-A tracer test show a close similarity to the overall behavior observed for RPM45-A tracer test. The magnitude of maximum values of normalized integrated volume and second spatial moments are comparable to those observed in the RPM45-A (Figures 2.7(a) and 2.9(a)), suggesting that a similar degree of mixing was achieved during both tests.

While these results indicate that chaotic advection leads to enhanced tracer spreading and mixing within the monitoring network, the reorientation angle of 135° does not appear to have considerable impact on how much mixing actually occurred. Lester al. (2010a) defined the parameter, q, as the ratio of the mixing rate associated with an RPM flow with that of a purely dispersive system under steady flow. It was reported that q strongly varies with the RPM flow parameters, where greater values of q correspond to a faster rate of mixing toward the well-mixed state. Given a Peclet number of ~20 for our experimental system based on the radius between the IE wells as the length scale, we use Figure 2(a) from Lester et al. (2010a) to estimate the degree of mixing theoretically possible between the two RPM scenarios involving different reorientation angles. The value of τ was determined by dividing the pumping duration (t_p) by the characteristic domain emptying time, as defined by Trefry et al. (2012). For values of $\Theta/2\pi$ corresponding to our reorientation angle of 45° and 135° (i.e., 1/8 and 3/8, respectively) and τ of 0.05, both the RPM45-A and RPM135-A tracer tests appear to lie in a similar region (q ~1.75). This indicates that both RPM reorientation angles are theoretically predicted to produce a similar rate of mixing. As discussed by Lester et al. (2010a), the degree of mixing relies not only on the reorientation angle but also on a combination of other RPM flow parameters. The flow rate, pumping duration and reorientation angle must be determined in conjunction with theoretical considerations to achieve the desired outcome. While a greater degree of mixing may be theoretically possible, practical design limitations must also be considered in the selection of the flow rate and pumping duration to minimize the amount of mass being captured at the IE wells.

2.4 CLOSURE

Multiple lines of evidence assembled in this proof-of-concept study demonstrate the potential of enhanced reagent delivery using chaotic advection. The pressure fluctuations showed a fairly consistent peak amplitude during injection and extraction. Despite issues in one of the IE wells, the hydraulic requirements for RPM flow were successfully achieved in all tracer tests, with six dipoles undergoing transient switching for the entire test duration. The *in situ* DRPs yielded responses that were shown to be a proxy for the Cl^- concentrations observed in groundwater samples, and where used to collect high-resolution temporal and spatial data. Consequently, the DRPs provided an inexpensive alternative for real-time, continuous monitoring of tracer distributions that yields analogous measures to concentrations, and minimizes the need for manual sampling events. The BTCs of the DRP responses showed oscillatory behavior at all depths, which suggests that RPM flow was occurring in this system. The Fourier transform of the temporal data revealed a broad, continuous spectrum in the frequency domain, consistent with the expected behavior of a chaotic signal, suggesting that chaos was generated *in situ*. A comparison of the DRP or equivalent Cl^- responses between the mixing and control tests suggested that a higher degree of spreading and mixing is made possible by chaotic advection. The results from various quantitative metrics adopted to demonstrate field-scale evidence of chaotic advection showed that the mixing test led to increased lateral spreading and enhanced mixing of the tracer with uniform or equivalent Cl^- values established across the monitoring network.

While the results discussed in this paper highlight the potential of an RPM flow system to invoke chaotic advection for enhanced reagent delivery, insights into the engineering controls to achieve optimal system behavior are not discussed. Based on the results, it was observed that the extent of the tracer spreading and mixing relies not only on the reorientation angle in an RPM flow system, but on a combination of RPM flow parameters which is consistent with Lester et al (2010a). In this study, eight IE wells in a circular array (diameter of 1.75 m) were used for the RPM flow system; however, chaotic advection can be invoked with any number of wells depending on the desired spatial scale, as long as the hydraulic requirements are met with a minimum of two dipoles to achieve transient switching. With sufficient optimization of the RPM flow parameters based on theoretical considerations and conditioned on hydraulic properties, a greater degree of mixing is likely possible. In practice, the selection of RPM flow parameters is the most critical design consideration for successful implementation of chaotic advection to achieve enhanced mixing while minimizing the tracer mass captured at the IE wells.

In summary, the findings from this field investigation demonstrate that an RPM flow system is a viable method for achieving chaotic advection in a porous medium that can significantly enhance reagent delivery. For improved robustness of this system, this proof-of-concept study should be extended to larger spatial scales and higher degree of heterogeneity using alternative RPM flow protocols leading to a more comprehensive understanding of engineered chaotic advection in the subsurface.

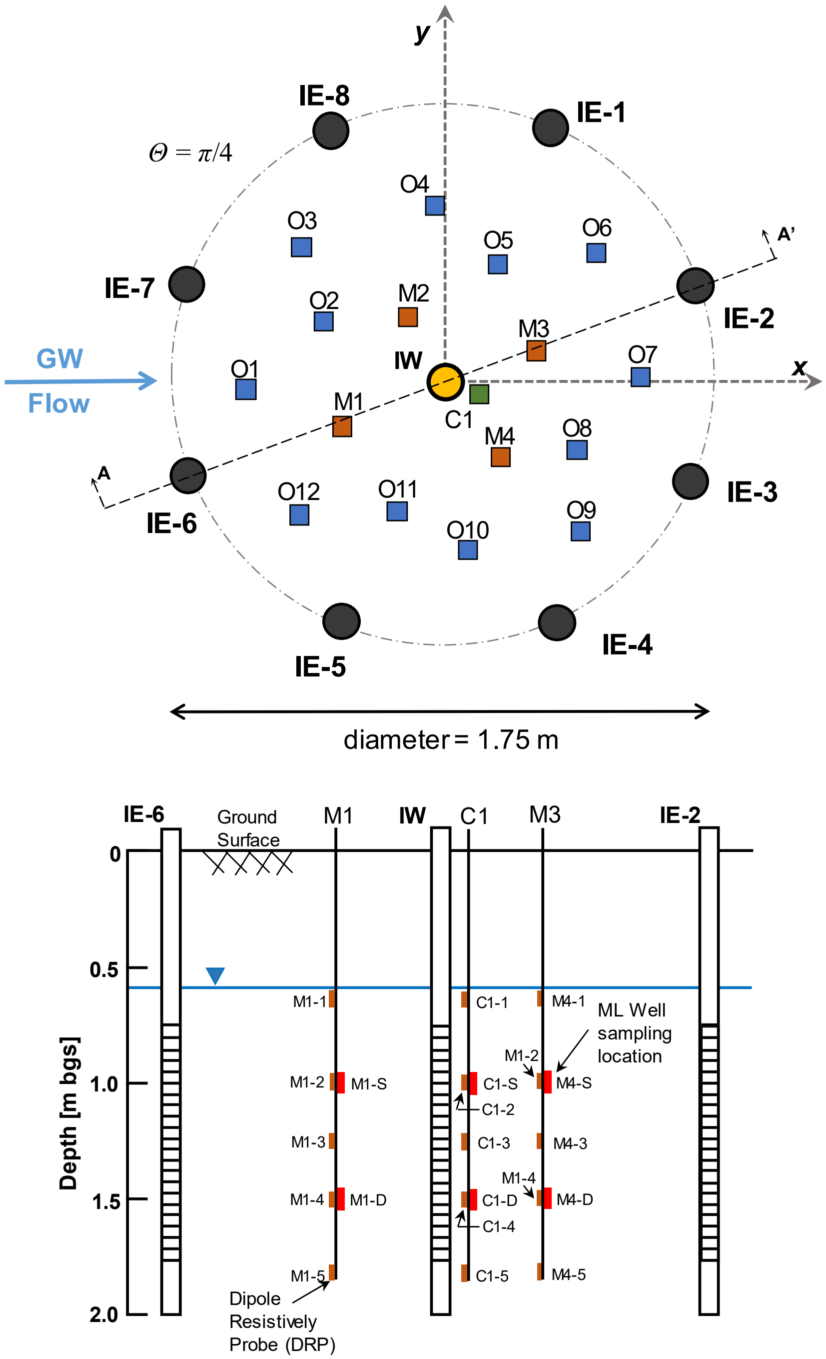

Figure 2.1. (a) Plan view of the circular system of injection/extraction wells (IE-1 to IE-8), central tracer injection well (IW), and location of monitoring wells: central ML well (C1), middle ML wells (M1 to M4), and outer ML wells (O1-O12). (b) Cross-section view (A-A') showing injection/extraction well IE-6 and IE-2, the tracer injection well IW, and ML wells M1, C1 and M4. Each ML well was equipped with a shallow (-S) and deep (-D) groundwater sampling location, and a series of dipole resistivity probes (DRPs). The water table location varied from 0.3 to 0.9 m bgs (average of 0.6 m bgs) over the two field seasons.

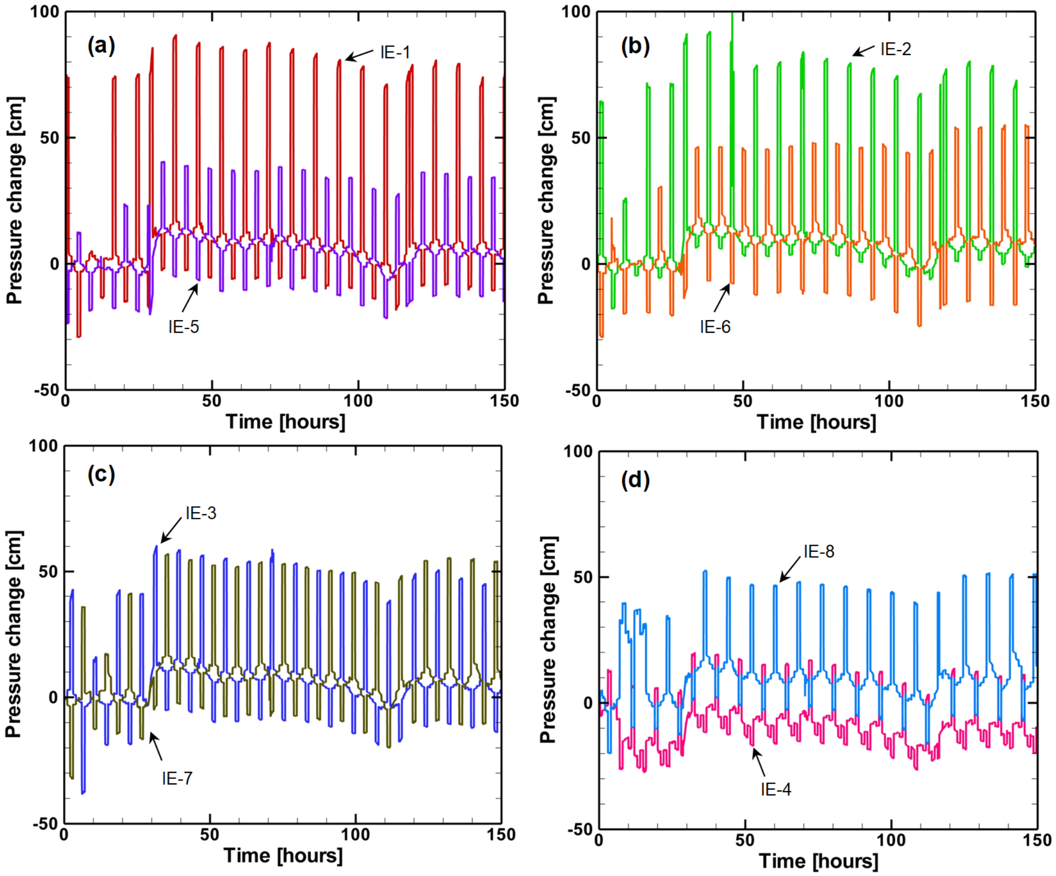

Figure 2.2. Pressure change during the mixing phase for the RPM45-A tracer test at well pairs: (a) IE-1 & IE-5, (b) IE-2 & IE-6, (c) IE-3 & IE-7 and (d) IE-4 & IE-8. A positive pressure change implies that the well is operating as an injection well, while a negative pressure change implies that the well is operating as an extraction well.

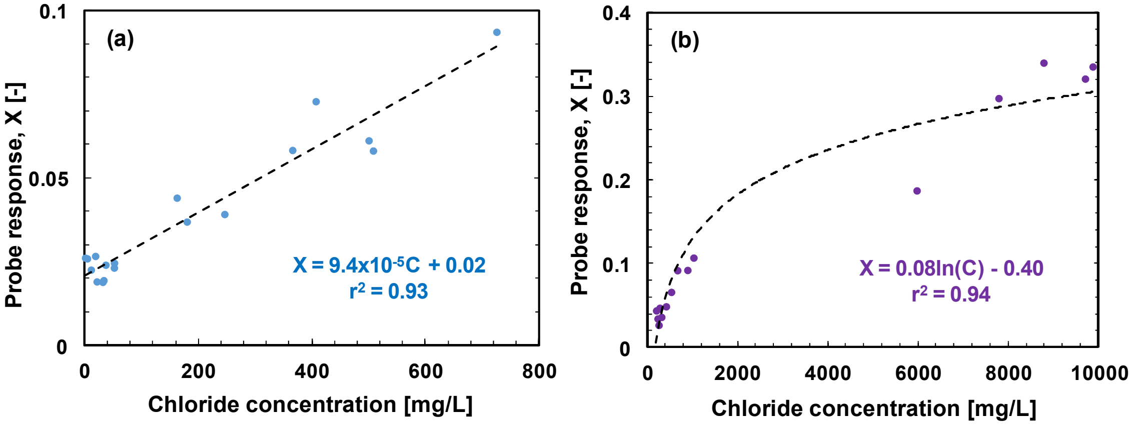

Figure 2.3. DRP response and chloride concentration (mg/L) sampled from the corresponding ML location for (a) O7-S (1.1 m bgs) and (b) M2-D (1.5 m bgs). Dashed line is the best-fit logarithm relationship.

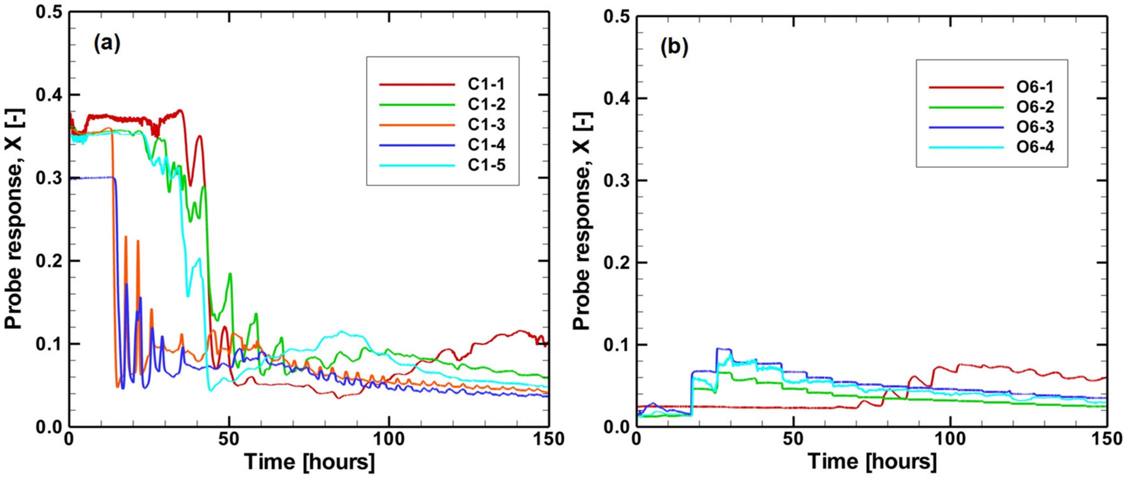

Figure 2.4. DRP response breakthrough curves during the mixing phase for the RPM45-A tracer test at location (a) C1 (0.3 m away from the IW), and (b) O6 (0.7 m away from the IW).

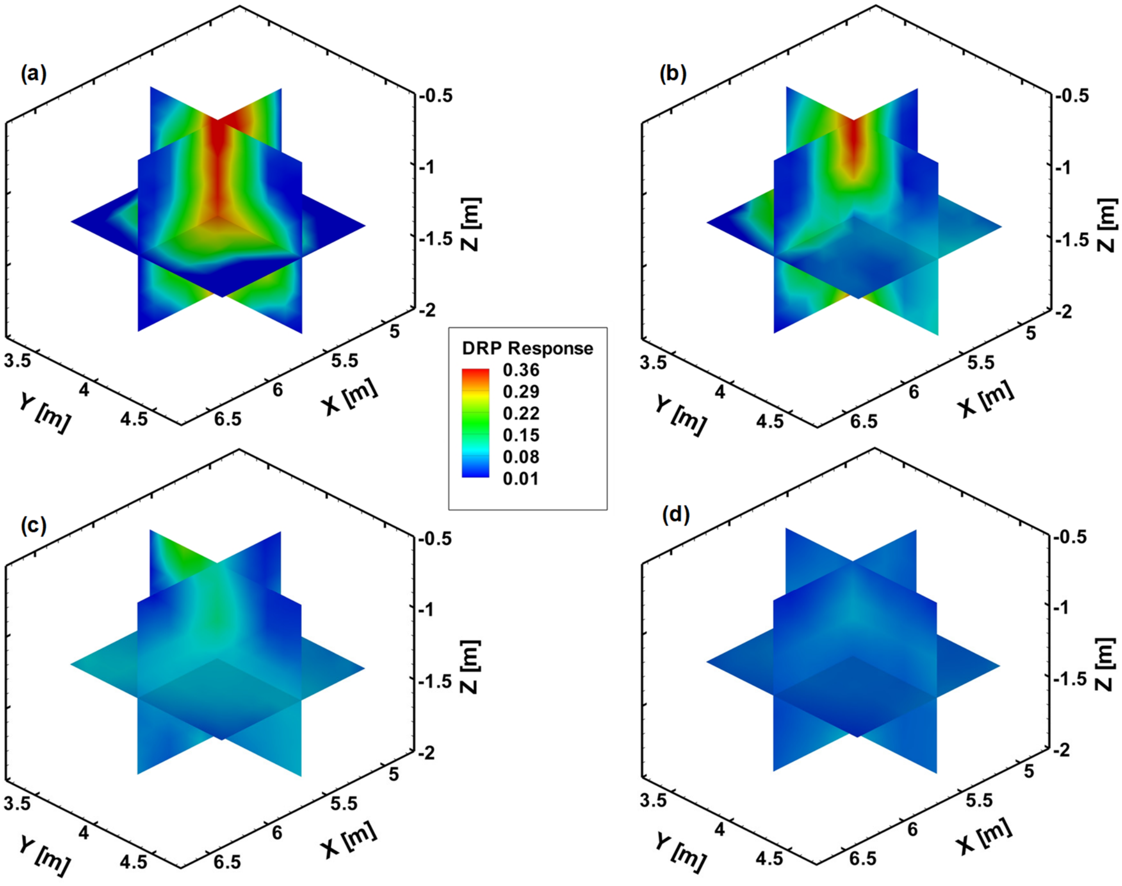

Figure 2.5. DRP response contours along three orthogonal planes through the center of the screened portion of the IW during the RPM45-A tracer test for (a) post-injection, (b) after 1 day of RPM flow, (c) after 2 days of RPM flow, and (d) after 4 days of RPM flow.

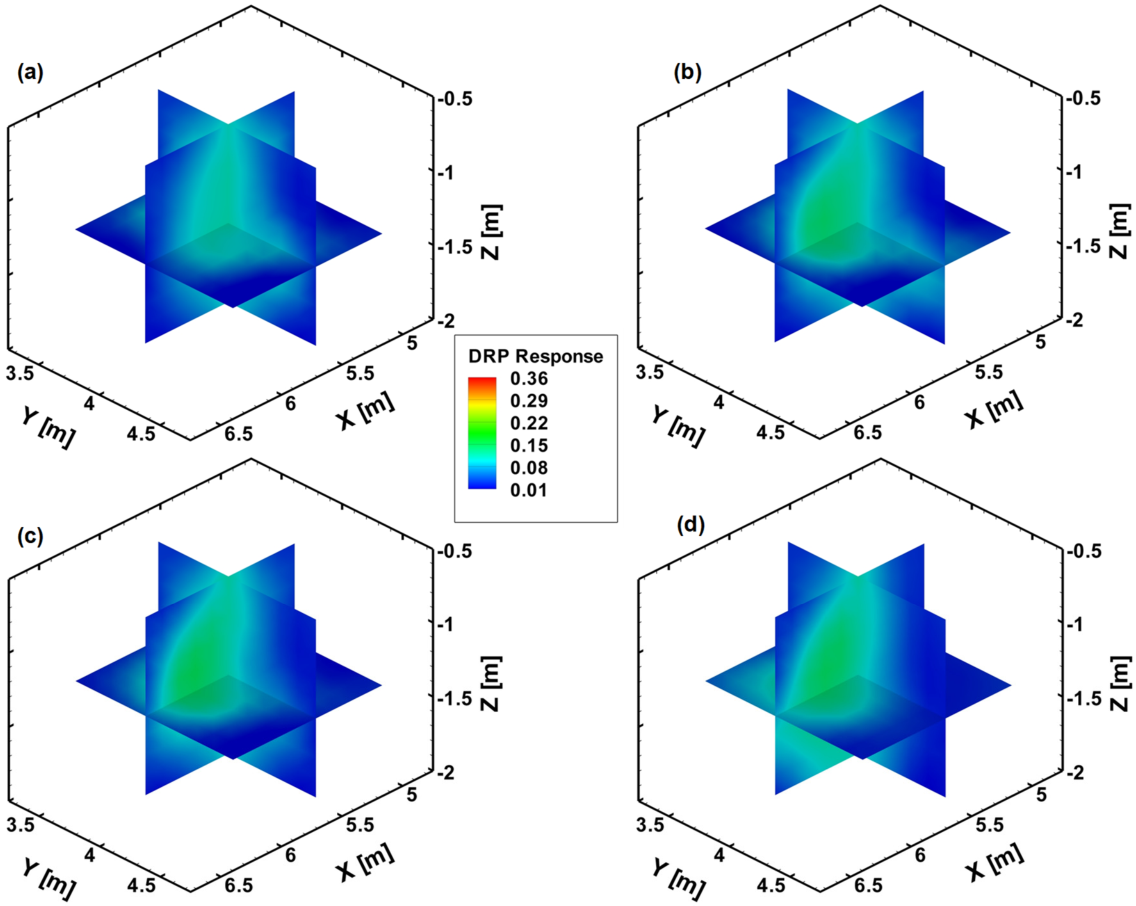

Figure 2.6. DRP response contours along three orthogonal planes through the center of the screened portion of the IW during the CTR1-A tracer test (C_{inj} of 1 g/L) for (a) post-injection, (b) after 1 day, (c) after 2 days, and (d) after 4 days.

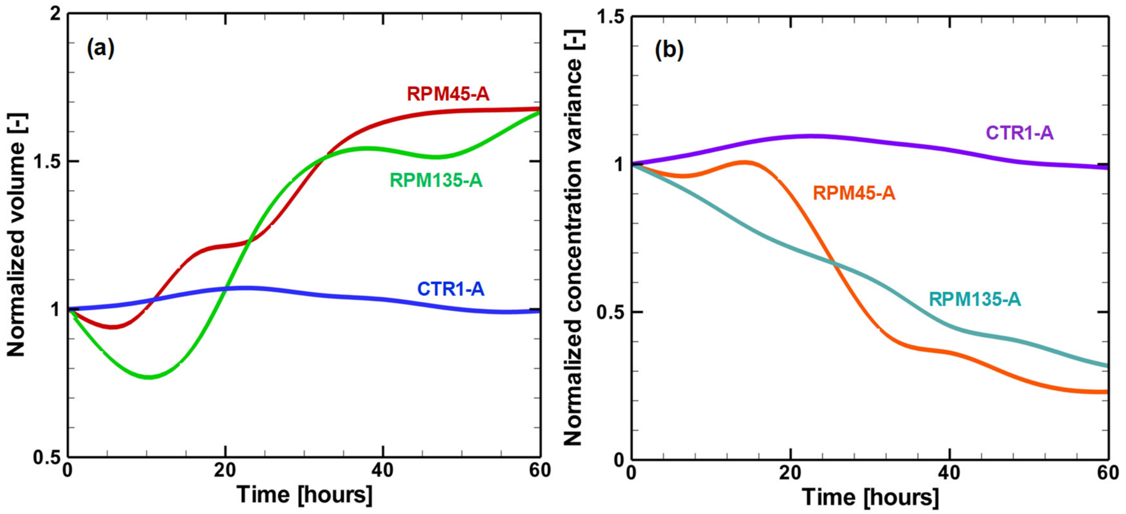

Figure 2.7. Temporal profile of normalized (a) total enclosed volume based on the DRP response contours, and (b) variance ($s^2_{C^*}$) of the equivalent Cl$^-$ concentrations from the 73 DRPs for the RPM45-A, RPM135-A and CTR1-A tracer tests. Volume and variance were normalized to values estimated at the end of the equilibrium phase.

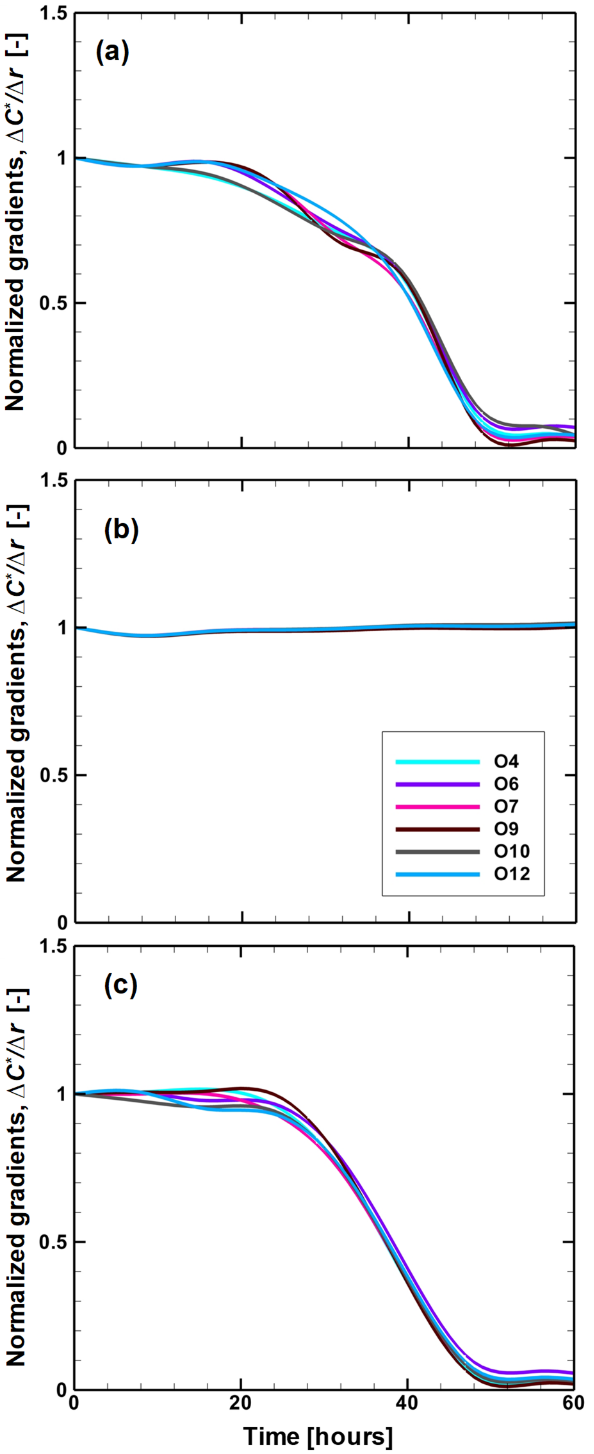

Figure 2.8. Temporal profile of normalized values of absolute concentration gradients between the outer probe locations (O#) relative to C1 at a depth of 1 m bgs during the (a) RPM45-A, (b) CTR-A and (c) RPM135-A tracer test. Gradients were normalized to values estimated at the end of the equilibrium phase.

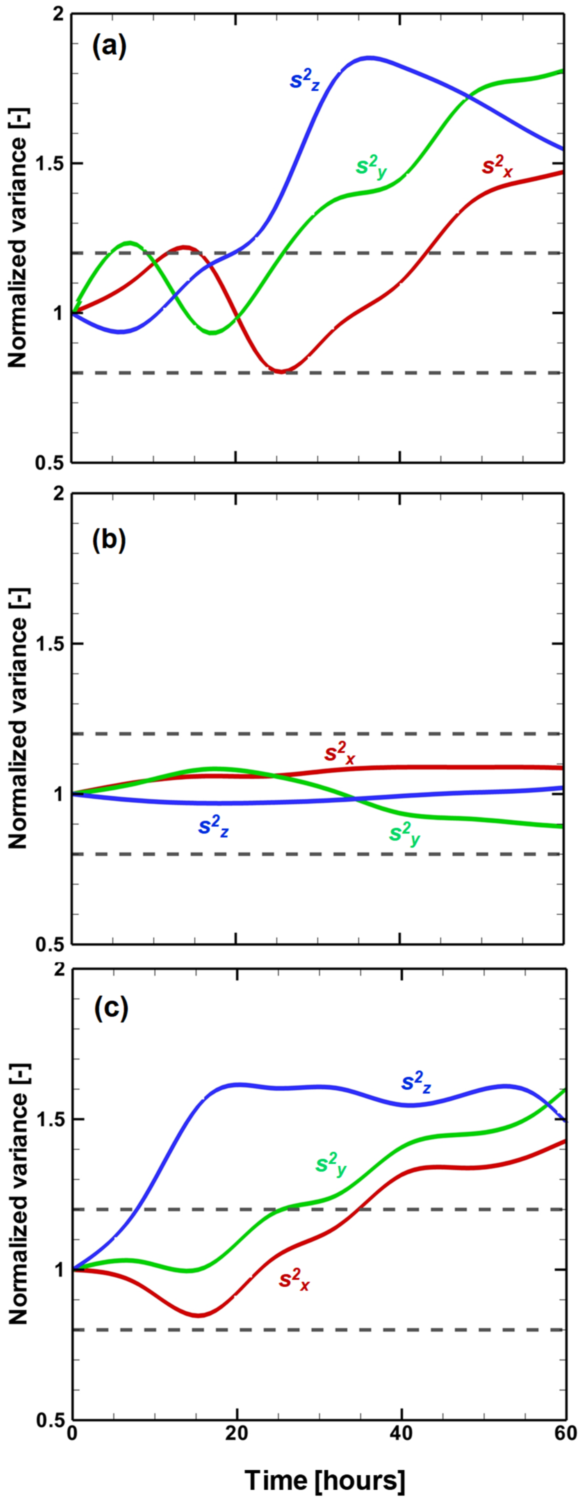

Figure 2.9. Temporal profile of normalized spatial variance (s^2_x, s^2_y, and s^2_z) for tracer tests (a) RPM45-A, (b) CTR1-A, and (c) RPM135-A. Variances were normalized to values estimated at the end of the equilibrium phase. The horizontal dashed lines represent an arbitrary uncertainty envelope of ±20% around the initial variance values.

Table 2.1. Summary of chaotic advection tracer tests performed in the 8-well installation.

Phase	**Parameters**	**Test Series[1]**			
		RPM45	**RPM135**	**CTR1**	**CTR10**
	Number of tests	6	2	3	1
Injection	Tracer concentration, C_{inj} (g/L)	10	10	1	10
	Total duration, t_{inj} (hours)	0.5	0.5	0.5	18
Equilibrium	Total duration, t_{eqm} (hours)	24	23	-	-
Mixing		***RPM Flow Mixing***		***Control***	
	Pumping rate, Q_{RPM} (L/min)	~2	2.5	-	-
	Pumping duration, t_p (hours)	1	1	-	-
	Re-orientation angle, Θ (degrees)	45	135	-	-
	Number of cycles, n	21	18	-	-
	Total duration, t_{RPM} (hours)	168	142	121	124
Extraction	Total duration, t_{ext} (days)	9	8	8	7

1. Tracer tests within each series are denoted by a letter suffix. For example, CTR1-A, CTR1-B, and CTR1-C are used to identify the three tests associated with the CTR1 Series.

Chapter 3

Use of Steady-State Hydraulic Tomography to Inform the Design of a Chaotic Advection System[2]

Abstract

The concept of chaotic advection is a novel approach that has the potential to overcome some of the challenges associated with mixing of reagents that commonly occurs when injection based *in situ* treatment techniques are used. The rotated potential mixing (RPM) flow system is one configuration which has been theorized to achieve chaotic advection in porous media, and enhance reagent mixing by periodically re-oriented dipole pumping at a series of radial wells. Prior to field implementation of chaotic advection, the selection of an RPM flow protocol will likely require a numerical model that can adequately represent groundwater flow within the zone of interest. The hydraulic conductivity (*K*) field is the most critical input requirement for the selected groundwater flow model. Hydraulic tomography (HT) is an innovative characterization approach that has shown potential to provide information on a *K* field. In this investigation, we explored whether the same well system required to invoke chaotic advection can also be applied in a HT analysis, and evaluated the use of the generated *K* tomogram for the selection of RPM flow parameters that can enhance reagent mixing. A series of dipole pumping tests were conducted within an area of interest as defined by the limits of the circular network of eight injection/extraction wells used to invoke chaotic advection. Hydraulic head data collected from independent dipole pumping tests were used in an inverse model to perform steady-state hydraulic tomography (SSHT) analysis and generate a *K* tomogram. Both the *K* tomogram and an effective parameter approach (i.e., a single *K* value assigned across the entire spatial domain as determined by single well pumping and slug tests) produced estimates of hydraulic head that closely resembled those observed due to the relative homogeneous nature of the aquifer and the small spatial scale of the area of interest. In contrast, particle tracking results showed that incorporating a heterogeneous *K* field significantly enhanced the spatial distribution of particle trajectories indicative of reagent mixing. These findings support the hypothesis that the same

---

[2] This chapter is adapted from a paper that has been prepared with the intent for publication: Cho, M.S., Zhao, Z., Thomson, N.R., Illman, W.A. Use of steady-state hydraulic tomography to inform the selection of a chaotic advection system. *J. Contam. Hydrol.*

well system used to invoke chaotic advection can be combined with SSHT analysis as a viable site characterization tool for delineating the spatial variability of *K*. Incorporating this *K* tomogram in a groundwater flow model with a particle tracking engine can be used to aid in the selection of a site-specific RPM flow protocol to achieve enhanced reagent mixing.

3.1 INTRODUCTION

In situ treatment commonly involves the injection of a reagent into the subsurface to create a zone in which biological and/or chemical reactions lead to the mass destruction of contaminants (e.g., enhanced biodegradation, chemical oxidation/reduction). In these injection-driven remedial systems, the delivery of reagent solutions is a key requirement for success. Following the injection of a reagent solution, the reagent and contaminant must come in contact in the subsurface for the desired biological or chemical reactions to occur (Kitanidis and McCarty, 2012). This contact between the injected reagent and contaminant is the desired outcome of an effective delivery system; however, it is often hindered by subsurface heterogeneities that create preferential flow pathways at a range of spatial scales (Dagan, 1986; Scheibe and Yabusaki, 1998) which leads to a non-uniform distribution of the injected reagent. For conventional injection methods that use vertical wells, the injected reagent distribution will be greater in areas of higher hydraulic conductivity (K) (Payne et al., 2008), as the fluid follows the path of least resistance from the wellbore into the porous medium. Depending on the K contrast, perhaps due to the presence of small-scale structures in sedimentary deposits (e.g., bedding planes, laminations, fractures, etc.), the injected reagent may bypass adjacent regions of lower K (Saenton et al., 2002; Dagan and Neuman, 2005; Zhong et al., 2011). In these lower K zones, molecular diffusion ($D^* \sim 10^{-9}$ m^2/s) is the primary transport mechanism responsible to bring the injected reagent and contaminant together (Jose and Cirpka, 2004; Gale et al., 2015); however, diffusion is a slow process which contributes to inefficient mixing (Kitanidis and McCarty, 2012). Ineffective mixing can lead to partial removal of the contaminant mass in a source zone which results in eventual rebound of contaminant levels and long-term persistence of plumes (Thomson et al., 2008), contributing to lengthy remediation timelines (Kitanidis and McCarty, 2012).

The concept of chaotic advection (Trefry et al., 2012; Aref et al., 2017) has the potential to overcome some of these challenges associated with mixing, and improve reagent distribution in the subsurface. Chaotic advection has been defined as the creation of "small-scale structures" resulting from the repeated stretching and folding of fluid elements in a laminar flow regime (Ottino, 1989; Aref et al., 2017). This stretching and folding of individual fluid parcels yields highly complex, intersecting particle trajectories which has been theorized to enhance the spatial distribution of solutes in porous media, and exponentially increase the zone of contact across which reactions can occur (Ottino, 1989; Bagtzoglou and Oates, 2007; Lester et al., 2009; Mays and Neupauer, 2012). The "small-scale structures" act to stir the fluid to elements at length scales small enough for diffusion to contribute to efficient mixing (Aref et al., 2017). One configuration which has been theoretically and experimentally used to achieve chaotic advection in porous media involves periodically re-oriented dipole flow through the transient switching of pressures at a series of radial wells. This configuration has been termed rotated potential mixing (RPM) flow in the relevant literature (Metcalfe et al., 2008), and assumes a completely closed system where the fluid removed from the extraction well is immediately re-injected at the injection well (Trefry et al., 2012). In an RPM flow protocol, a dipole consisting of one injection and one extraction well separated by 180° operates for a fixed time (t_p). This dipole is then instantaneously re-oriented by a specified reorientation angle (Θ) and resumes pumping for t_p. A repeated sequence of this periodically re-oriented dipole pumping will eventually produce chaos in the flow regime corresponding to complex particle trajectories (Lester et al., 2009; Metcalfe et al., 2010). In an RPM flow system, the reorientation angle (Θ), pumping duration (t_p) and flow rate (Q) have been identified as key parameters (Metcalfe et al., 2010).

The selection of RPM flow parameters (t_p, Θ and Q) is critical for successful implementation of chaotic advection in the field (Lester et al., 2010; Trefry et al., 2012). Determination of an RPM flow protocol will likely require a numerical model that can adequately represent groundwater flow within an aquifer undergoing periodically re-oriented dipole pumping. It is expected that the K field will be the critical data requirement for the groundwater flow model. It is widely accepted that accurate estimation of the K field can have significant implications for groundwater flow, contaminant transport and hence, on the design of an effective remediation system to achieve the desired treatment outcomes (Illman et al., 2008; Berg and Illman, 2013).

Traditional K characterization methods (i.e., pumping tests) yield effective parameters, which are averaged over a large volume and are representative only of bulk flow behavior (Brauchler et al., 2011). Other K characterization methods like slug tests yield a single K estimate for a small aquifer volume in the immediate vicinity of the piezometer (Freeze and Cherry, 1979). Using geostatistical interpolation to obtain a spatial distribution of K requires a large number of small-scale K measurements from cores or slug tests, which is both expensive and time-consuming (Yeh and Liu, 2000; Liu et al., 2007; Berg and Illman, 2013). For instance, Sudicky (1986) obtained over 1279 *K* estimates from falling head permeameter tests on core samples to delineate the spatial variability of a *K* field. In contrast, hydraulic tomography (HT) is a novel characterization approach that has shown potential to provide information on a *K* field. HT involves pumping (or injecting) water into a well, monitoring the aquifer response at nearby well locations, and then repeatedly switching the pumping or injection locations (Yeh and Liu, 2000; Zhu and Yeh, 2005). The drawdown responses collected from a HT survey are subsequently used in an inverse model to generate an image of the *K* distribution (i.e., *K* tomogram). Transient hydraulic tomography (THT) yields a tomogram of both *K* and specific storage (S_s). Both steady-state and transient hydraulic tomography have been used to characterize aquifer heterogeneities in laboratory-scale sandbox experiments and in the field (Liu et al., 2007; Illman et al., 2007; Berg and Illman, 2011b; Berg and Illman, 2013; Zhao and Illman, 2018). Results from these studies indicate that use of *K* tomograms lead to considerably improved prediction of aquifer responses during a pumping test. Forward simulations using *K* tomograms as the representation of the *K* field consistently showed the highest correlation between simulated and observed drawdown in comparison to the effective parameter approach (i.e., a single *K* value assigned across the entire spatial domain) and other methods (e.g., *K* fields from interpolation of small-scale measurements).

In this study, we propose that the well system required to invoke chaotic advection can also be applied in a HT analysis, and explore whether subsequent use of this *K* tomogram in a groundwater flow model can aid in the design of an RPM flow system. The specific objectives were to assess whether hydraulic head responses from multiple independent dipole pumping tests can be used in three-dimensional steady state hydraulic tomography (SSHT) analysis to capture *K* heterogeneities, and then to investigate the impact of using this *K* tomogram on the selection of an RPM flow protocol and the spatial distribution of a hypothetical reagent. The findings from this investigation are significant since the ability to use the same well system to invoke chaotic advection, as that used as a site characterization tool to delineate *K* variability, would be advantageous. Using *K* information applicable to a specific target treatment zone would allow for improved design of a chaotic advection system, which would ultimately lead to enhanced treatment effectiveness.

3.2 HYDRAULIC TOMOGRAPHY (HT) SURVEY

The HT survey was performed in an experimental gate located in a sandpit at the University of Waterloo Research Aquifer Facility at Canadian Forces Base (CFB) in Borden, Ontario. The gate was 8 m wide by 11 m long, and hydraulically isolated on two sides by hanging sheet pilings driven down to ~2 m below ground surface (bgs). The other two sides had ~2.5 m wide openings in the center that allowed groundwater to flow through the cell controlled by the regional horizontal hydraulic gradient in the upper 2 m of the aquifer.

The unconfined Borden aquifer at this location is composed primarily of unconsolidated fine to medium-grained well-sorted sand (porosity of 0.33) that extends ~9 m in thickness and underlain by a clayey and sandy silt aquitard. Some microscale heterogeneities are present in the form of silty sand and coarse sand lenses. The water table varies seasonally but is typically located at ~0.6 m bgs (Mackay et al., 1986; Sudicky, 1986). The specific storage is reported to range from 3.3×10^{-5} to 1.0×10^{-3} m^{-1} (Moench, 2008; Frind et al., 1999). Previous analysis on soil cores collected from CFB Borden reported a range of horizontal K from 6.0×10^{-6} to 2.0×10^{-4} m/s, with a geometric mean of 6.8×10^{-5} m/s. Geostatistical analyses of the K estimates from core samples indicated that the average horizontal and vertical correlation lengths, and variance of ln$K$ ($\sigma^2_{\ln K}$) are 4.75 m, 0.2 m, and 0.2, respectively (Sudicky, 1986; Woodbury and Sudicky, 1991; Rivett et al., 1994; Turcke and Kueper, 1996; Tomlinson, 2003). The vertical hydraulic conductivity is estimated to be approximately one third of the horizontal (Mackay et al., 1986; Sudicky, 1986).

Within the gate, eight (8) injection/extraction wells (identified as IE-1 to IE-8) were installed in a circular network with an approximate diameter of 1.75 m (Figure 3.1). All boreholes were advanced using a direct-push method (Geoprobe® 7720DT) to a depth of ~2 m bgs. While the casing was pulled back to surface, the aquifer material was allowed to collapse around the 5.1 cm diameter well (schedule 40 PVC). Each IE well was screened (2.5 mm slot) from 0.75 to 1.75 m bgs. All wells were developed after installation.

Eight (8) single well pumping tests, and a series of slug tests (a total of six (6) falling and rising head tests) were performed at each IE well to obtain estimates of K. The single well pumping tests were performed using a peristaltic pump (Cole-Parmer, Masterflex® 7549-32 with Masterflex® 7019-43 pump head) with a flow rate of ~3 L/min for 35 to 40 minutes until apparent steady-state conditions were established (i.e., when insignificant changes were observed in the hydraulic heads at all IE well locations). Once the pumping test was finished, a recovery period (20 to 30 minutes) was implemented to allow water levels to return to baseline conditions prior to the start of the next test. Slug tests were performed using a bailer (2 m in length) which was placed into the respective IE well and removed after 2 to 3 minutes.

An above-ground injection/extraction system (Figure D-1) that consisted of sixteen (16) solenoid valves (ASCO Red-Hat 8210G002 120/60, 110/50) connected to a peristaltic pump (MasterFlex, 7549-32 with MasterFlex, 7019-43 pump head), and a programmable logic controller (PLC) unit (Allen-Bradley 1760-L18AWA-EX ser. B with 1760-IA12XOW6I ser. A expansion) was used for the HT survey. Check valves were placed at the end of each solenoid valve to prevent potential clogging and malfunction, as solenoid valves are one-directional and unable to withstand backpressure from pumping. Dedicated PVC tubing was attached to the respective solenoid valve pair and placed in each IE well. The end of each PVC tubing (~10 cm in length) was prepared with 3.9 mm holes and wrapped with 125 µm Nitex® screen.

The HT survey consisted of two data collection stages. During Stage-1, a series of independent dipole pumping tests were conducted using the eight IE wells (see Table 3.1 for the well pairs involved in each test) and the above-ground injection/extraction system (Figure D-1). Each pumping test involved only one active dipole (one injection and one extraction well), with all other wells inactive. The independent dipole pumping tests were performed using a "high" (Q ~3 L/min) and a "low" (Q ~1.8 L/min) flow rate. Each test was run until apparent steady-state conditions were established as indicated by insignificant changes in the observed hydraulic heads at all IE well locations. After each independent dipole pumping test, a rest period (~15 minutes) was implemented to allow sufficient time for the hydraulic head changes resulting from the pumping to return to baseline conditions. Steady-state observations of hydraulic heads from select independent dipole pumping tests were then used in the inverse model to generate a K tomogram. The remainder of the dipole pumping tests not used in the SSHT analysis were compared to the simulated predictions of steady-state hydraulic heads for validation of the K tomogram. During Stage-2, a complete RPM flow protocol was implemented using the dipole pumping system where each IE well pair was operated for t_p = 1 hour at Q_{RPM} ~1.8 L/min. After duration t_p, the active dipole was turned off (i.e., valves closed) and re-oriented by the reorientation angle (Θ = 45°) before pumping resumed at the new dipole using the same t_p and

Q_{RPM}. This periodically re-oriented dipole pumping was repeated around the IE well network for ~6 days (i.e., 18 complete RPM cycles, $N = 18$). Observations of transient hydraulic heads collected during the implementation of this RPM flow protocol were compared to simulated hydraulic heads for validation of the K tomogram.

A submersible datalogger (CTD Diver, Van Essen Instruments, Kitchener, ON) was placed in each IE well (eight (8) in total) and collected measurements of pressure every minute. All pressure transducer readings were barometrically corrected. A total of eight (8) flow meters (Assured Automation, WM-PC-050), dedicated to each dipole, recorded the cumulative volume of groundwater pumped from each extraction to injection well over the duration of each test.

3.3 MODELING APPROACH

Hydraulic head data collected from select independent dipole pumping tests were used in an inverse model to perform SSHT analysis and for generating an estimate of the K field (i.e., K tomogram). To assess the impact of using this K tomogram in a three-dimensional (3D) groundwater flow model, simulated steady-state hydraulic heads were compared to those observed during the independent dipole pumping tests. A 3D transient groundwater flow model was also developed and was used to simulate the hydraulic response of the Borden aquifer during an RPM flow protocol. This 3D transient model was subsequently extended to include particle tracking and used to investigate the impact of this K tomogram on the spatial distribution of particle trajectories in a target treatment zone as an indicator of reagent mixing. For validation of the estimated K field, all forward simulations were performed using the K tomogram (SSHT scenario) determined from the inversion of steady-state hydraulic head observations during the independent dipole pumping tests, and compared to the effective parameter approach (K_{eff} scenario) in which a single value of K was assigned across the entire spatial domain as the representation of the K distribution.

3.3.1 Steady-State Hydraulic Tomography (SSHT) Analysis of Multiple Dipole Pumping Tests

3.3.1.1 Inverse Modeling Method

The SSHT analysis of independent dipole pumping tests was performed using the sequential successive linear estimator (SSLE) model developed by Yeh and Liu (2000). All inverse simulations were performed using a finite element mesh (8 m by 11 m by 9 m; Figure D-2) which consisted of rectangular elements variable in size. In the central portion of the model domain where all field tests were conducted, 0.25 m by 0.25 m by 0.25 m size elements were used. Outside this central portion, the element size was increased to 0.5 m by 0.5 m in the x- and y- directions. In the z-direction (where $z = 0$ coincides with the underlying aquitard), one element was assigned from 0 to 6.5 m, and 10 elements ($\Delta z = 0.25$ m) from 6.5 to 9 m, corresponding to the depth of the sheet pilings (0 to 2 m bgs). In total, the model domain consisted of 6776 elements (28 x 22 x 11) and 8004 nodes (29 x 23 x 12).

The bottom, and portions of the model domain that correspond to the location and depth of the sheet pilings, were assigned no-flow boundary conditions. Along all other boundaries, a constant head boundary condition was employed and assigned a value of 9 m. Additional input parameters specified were initial estimates of K, as well as geostatistical parameters (correlation lengths (λ_x, λ_y, λ_z) and variance) (see Table 3.2). Pumping wells were assigned as source/sink terms in the elements corresponding to the location of IE well pair involved in each dipole pumping test with estimated flow rates from the field (Q = 2.9 to 4.1 L/min, and $\bar{Q}$ = 3 L/min across all dipoles). Hydraulic head responses were selected from the steady-state portion of the change in hydraulic head profiles associated with each independent dipole pumping test. Convergence criteria were considered to be met when either the change in the estimated K field was below a minimum threshold (i.e., variance between iterations <0.001), or the maximum number iterations ($n = 500$) was achieved.

3.3.1.2 Calibration and Validation of *K* Tomogram using the SSLE

To assess whether the use of the K tomogram leads to improved predictions of hydraulic head responses during an independent dipole pumping test, 3D simulations of steady-state groundwater flow were performed using the SSLE model with the K tomogram as the representation of the K distribution. These steady-state simulation results using the K tomogram were then compared to those generated by the effective parameter approach in which a single value of K, as determined by the single well pumping and slug tests, was assigned across the entire spatial domain.

Scatterplots were used to illustrate the relationship between simulated and observed values of hydraulic head changes. Model calibration was examined by incorporating the K tomogram in the 3D forward SSLE model to simulate the steady-state hydraulic responses during the independent dipole pumping tests used in the inversion process. These calibration simulations examine how well the computed *K* tomogram was able to reproduce the observations of hydraulic head used in the inverse model. For model validation, predictions of steady-state hydraulic head were generated using the 3D forward SSLE model for the independent dipole pumping tests not used in the SSHT analysis (Illman et al., 2007; Berg and Illman, 2013).

For each scatterplot, the best-fit line consisting of the slope, intercept and coefficient of determination (r^2) was estimated, and compared to the 1:1 line which represents a perfect match between the simulated and observed values of hydraulic head changes. A strong correlation between the simulated and observed hydraulic head changes would lead to points scattering along the 1:1 line. To further assess how well the change in simulated values of hydraulic head compare to the observed, the mean absolute error norm (L_1) and mean square error norm (L_2) associated with each scatterplot were calculated for the independent pumping tests (Xiang et al., 1992; Berg and Illman, 2013):

$$L_1\,(m) = \frac{1}{n}\sum_{i=1}^{n}|\chi_i - \hat{\chi}_i| \tag{3.1}$$

$$L_2\,(m^2) = \frac{1}{n}\sum_{i=1}^{n}(\chi_i - \hat{\chi}_i)^2 \tag{3.2}$$

where *n* is the number of hydraulic head observations and, χ_i and $\hat{\chi}_i$ are simulated and observed change in hydraulic head (meters), respectively. The L_1 and L_2 norms are useful model performance metrics with smaller values of L_1 and L_2 norms indicative of simulated estimates of hydraulic head changes that are closer to the observed (Illman et al., 2007; Berg and Illman, 2015). While the L_1 norm is a useful indicator of the overall model performance, the L_2 norm gives more weight to larger differences, leading to detection of potential outliers (Xiang et al., 1992).

3.3.2 3D Transient Flow Simulations

Simulations were performed using a 3D transient groundwater flow model to investigate the impact of using the *K* tomogram as the representation of the *K* field on predictions of hydraulic heads, and on the spatial distribution of particle trajectories during repeated cycles of RPM flow.

The development of a numerical model that can represent groundwater flow during periodically re-oriented dipole pumping is a critical step towards the design of an effective RPM flow system.

The 3D transient simulations were performed using the MODFLOW-2005 and MODPATH engines in Visual MODFLOW® Flex (Version 2015.1; Waterloo Hydrogeologic, Kitchener, Ontario, Canada). The dimensions of the domain, as well as boundary conditions used for these transient simulations were the same as those used in SSLE model; however, this domain was discretized with the smallest grid blocks (0.05 m by 0.05 m by 0.05 m) in the central portion of the domain where all field tests were conducted. A smaller discretization was selected for this model domain to adequately represent the complexities in the flow fields produced by the transient RPM flow system. Outside this central portion, the grid blocks were increased to 0.1 m by 0.1 m in the x- and y-directions. In the z-direction, one block was assigned from 0 to 6.5 m, and 50 blocks ($\Delta z = 0.05$ m) from 6.5 to 9 m. In total, the finite difference grid was composed of 110 rows, 140 columns and 51 layers (Figure D-3).

Pumping wells were assigned to the appropriate layers of the model grid with a time-dependent schedule that corresponds to the IE well pair involved in the RPM flow protocol. Cumulative volumes obtained from flow meter data were used to estimate the average flow rate for each dipole (i.e., Q_{RPM} = 1.2 to 2.4 L/min, and $\bar{Q}_{RPM}$ = 1.8 L/min across all dipoles). A value of 0.33 was used for the specific yield, S_y, to represent this shallow unconfined aquifer system. The K tomogram generated from the SSHT analysis was imported into Visual MODFLOW® Flex and assigned as an interpolated surface to the corresponding layer of the finite difference grid. For the K_{eff} scenario, the same K value used in the steady-state SSLE model was assumed for the entire model domain. The Conjugate Gradient Solver (CGS) was used in the MODFLOW engine with a convergence criterion of 10^{-7} m.

A scatterplot was used to show the relationship between simulated values of hydraulic head and those observed during RPM flow, and to determine a best-fit regression line. In addition to the L_1 and L_2 norms, the correlation coefficient (R) was determined for the transient simulation results produced by both the SSHT and K_{eff} scenarios using (McCuen and Snyder, 1986; Liu et al., 2007):

$$R = \frac{\frac{1}{n}\sum_{i=1}^{n}(\chi_i - \mu_\chi)(\hat{\chi}_i - \mu_{\hat{\chi}})}{\sqrt{\frac{1}{n}\sum_{i=1}^{n}(\chi_i - \mu_\chi)^2 \cdot \frac{1}{n}\sum_{i=1}^{n}(\hat{\chi}_i - \mu_{\hat{\chi}})^2}} \tag{3.3}$$

where n is the number of hydraulic head observations, χ_i and $\hat{\chi}_i$ are simulated and observed values of hydraulic head changes at a given time, respectively, and μ_χ and $\mu_{\hat{\chi}}$ are the corresponding means of the simulated and observed hydraulic head changes, respectively. The *R* value is a quantitative metric that indicates the strength of correlation between observed and simulated values, with higher values of *R* (≤ 1) representing stronger correlation between the two data sets (McCuen and Snyder, 1986; Liu et al., 2007).

To investigate the consequence of using the *K* tomogram on the selection of an RPM flow protocol and the spatial distribution of a hypothetical reagent, the 3D transient groundwater flow model was extended to include particle tracking using the MODPATH engine. These particle tracking simulations represent a reagent solution previously injected at the center of the circular IE well network that is subsequently mixed by an RPM flow system. For this investigation, 48 particles were assigned in the cells immediately adjacent to the center of the circular network of the IE wells, at a depth that corresponds to the midpoint of the well screen. These initial particle positions are indicative of the approximate location of the hypothetical injected reagent solution. All particles were treated as forward tracking particles. Various combinations of RPM flow parameters (reorientation angle, Θ and pumping duration, t_p) were assessed for their ability to produce an enhanced spatial distribution of particle trajectories and thus, an increase in the cumulative travel distance within the area of interest, as defined by the limits of the IE wells to represent a target treatment zone. Using the spatial distribution of particle trajectories as an indicator of reagent mixing, and as a criterion for the selection of RPM flow parameters, supports the theory that chaotic advection results from the stretching and folding of fluid elements which produce highly complex, intersecting particle trajectories that can lead to enhanced reagent mixing (Ottino, 1989; Lester et al., 2009).

3.4 RESULTS AND DISCUSSION

3.4.1 Effective Hydraulic Conductivity

To determine *K* estimates in the area of interest by traditional characterization methods, the data collected from the single well pumping and slug tests were analyzed using AquiferTest (Waterloo Hydrogeologic, Kitchener, Ontario, Canada) (Table 3.3). The *K* estimate ranges from 5.3×10^{-5} to 7.6×10^{-5} m/s based on the single well pumping test data, and from 4.1×10^{-5} to 7.1×10^{-5} m/s using the slug test data. The *K* estimates from the single well pumping tests are slightly higher than those produced by the slug tests presumably due to the larger spatial scale captured by the test. Overall, the data from both tests yield a similar range of *K* estimates with a geometric mean of 6.3×10^{-5} m/s for the single well pumping tests, and 5.4×10^{-5} m/s for the slug tests. Since this difference is small, the horizontal K_{eff} value in the area of interest was assumed to be the combined geometric mean of 5.8×10^{-5} m/s (i.e., $K_{xx} = K_{yy}$). The vertical hydraulic conductivity, K_z, was assumed to be one third of this value to be consistent with previous findings for the Borden aquifer (Mackay et al., 1986; Sudicky, 1986). This K_{eff} value is within the typical range reported for the Borden aquifer (i.e., 6.0×10^{-6} to 2.0×10^{-4} m/s), and is consistent with the geometric mean (6.8×10^{-5} m/s) of the *K* estimates reported in other studies using soil cores from this site (Sudicky, 1986; Woodbury and Sudicky, 1991; Rivett et al., 1994; Turcke and Kueper, 1996). Collectively, these results indicate that the K_{eff} value determined from the single well pumping and slug test data is a reasonable assumption for the *K* value used in the effective parameter approach.

3.4.2 Hydraulic Responses

Figure 3.2 shows the observed hydraulic head changes relative to baseline conditions for all IE wells for two of the eight independent dipole pumping tests conducted at the "high" flow rate ($Q = 3 \pm 1.1$ L/min) (see Figure D-4 for the other test results). Only the hydraulic head observations from the dipole pumping tests performed at the high flow rate were used in the SSHT analysis based on the previous work of Illman et al. (2008) who demonstrated that increased pumping rates yield higher signal-to-noise ratios in the data collected from a HT survey, and lead to improved predictions of the *K* field. A positive hydraulic head change implies that water was being injected into the well, while a negative hydraulic head change implies that water was being extracted from the well. Steady-state conditions appear to be established within 2 minutes of pumping at each IE well, with steady-state hydraulic head changes ranging from 29 to 49 cm during injection, and from -48 to -25 cm during extraction (Figure 3.2). Hydraulic head changes are evident at the wells located ~0.7 m on either side of the injection/extraction wells, with hydraulic heads approximately an order of magnitude less than those observed at the active dipoles. Minor fluctuations in hydraulic head (≤ 0.5 cm) are observed at wells furthest away from the active IE wells.

Figure 3.3 shows the observed hydraulic head changes relative to baseline conditions at all IE wells during RPM flow. Figure 3.3(a) shows the change in hydraulic heads over the entire duration of the test when RPM flows are active (N = 18, t_{total} = 6 days), while Figure 3.3(b) shows the response to dipole pumping for the first 8 hours of the test (N = 1). Despite some fluctuations, the dipole system operated as expected with one IE well pair pumping for one hour before switching to the next pair. The frequency of the peak hydraulic head changes corresponds to the switching time (t_p of 1 hour) associated with the dipole pumping system, with peak hydraulic head changes ranging from 18 to 72 cm during injection, and -57 to -18 cm during extraction. As expected, the hydraulic head changes during extraction are less than those observed during injection for shallow wells in an unconfined aquifer (Freeze and Cherry, 1979). The suppressed amplitudes relative to the other IE wells during the fourth (D) and fifth (E) dipoles in the RPM flow pumping sequence (Figure 3.3(b)) is suspected to be the result of poor connection/contact between the solenoid valve wiring and the PLC unit that failed to provide the electrical signal required to open the valve and permit flow.

3.4.3 Visual Assessment of the *K* Tomogram

Sixteen (16) steady-state observations of hydraulic head from two different dipole pumping tests (Test G and Test B) were used sequentially in the SSHT analysis. The specific number and order of dipole pumping tests used in the inversion process were determined based on the combination of tests that produced a K tomogram within the range of K values observed from the single well pumping and slug tests in the area of interest. Previous work has shown that both the number and order of observations used in the inversion process are critical considerations in HT analysis as they impact the quality of the resulting K tomogram (Illman et al., 2008; Berg and Illman, 2011b).

The final K tomogram for the domain depth corresponding to the sheet pilings (i.e., 0 to 2 m bgs), and associated variance are shown in Figure 3.4. The upper ~0.4 m of the domain (red regions of the K tomogram in Figure 3.4(a)) shows K estimates that are higher than those observed from the single well pumping and slug tests in the area of interest (Table 3.3); however, this depth is above the well screen where no hydraulic head observations were available, and thus, is expected to produce greater uncertainty in the K estimates. Elsewhere in the area of interest, the K estimates are within the observed range (i.e., $4.1\text{x}10^{-5}$ to $7.6\text{x}10^{-5}$ m/s). The mean K within the area of interest from the K tomogram is $4.1\text{x}10^{-5}$ m/s, which is slightly lower than the K_{eff} value ($5.8\text{x}10^{-5}$ m/s), and near the lower limit of the observed K range based on the single well pumping and slug test data. The slight difference between these two mean K values is likely related to the spatial scale associated with each estimation method. The K tomogram provides a representation of the K distribution across the entire zone of interest and captures vertical K variability, whereas the estimate from the single well pumping and slug test data yield a bulk estimate of K.

The final K tomogram (Figure 3.4(a)) shows elongated zones of primarily horizontal, parallel layering that span across ~6 m in the x- and y- directions without interruptions by lower K features/horizons. Variability in the z-direction is observed with K estimates that range within an order of magnitude across layers ~0.25 m in thickness. These observations are consistent with previous efforts that have described the Borden aquifer as relatively homogeneous with horizontal and vertical correlation lengths of 4.75 m and 0.2 m, respectively (Sudicky, 1986; Woodbury and Sudicky, 1991; Rivett et al., 1994; Turcke and Kueper, 1996; Tomlinson, 2003). Furthermore, the sequential inversion of the dipole pumping tests produced a K field with a variance of ln(K) (σ^2_{lnK}) of 1.6 for the entire model domain. This value, as determined by the SSLE model as a variance of the K estimates assigned to each of the elements in the modeling domain (i.e., 6776 estimates in total), represents the overall degree of heterogeneity (Yeh and Liu, 2000). While σ^2_{lnK} values typically reported for the Borden aquifer range from 0.3 to 0.6 (Woodbury and Sudicky, 1991; Turcke and Kueper, 1996), these values are based on K estimates obtained from laboratory permeameter data. K estimates obtained from field pumping tests are expected to yield higher σ^2_{lnK} values due to the scale effects associated with observed responses, as well as aquifer heterogeneities (Berg and Illman, 2011b). For the relatively homogeneous Borden aquifer, σ^2_{lnK} values ranging from <1 to 2 from the SSLE model is considered reasonable based on values reported for other field sites of varying heterogeneity (Sudicky et al., 2010; Zhao and Illman, 2018). As a result, the σ^2_{lnK} value of 1.6 generated from the SSHT analysis is deemed to be a reasonable representation of the degree of heterogeneity for the entire model domain.

The variance associated with the *K* estimates is also low (~0.2 to 0.4 in Figure 3.4(b)) which suggests confidence in the *K* estimates obtained from the SSLE model. The values in Figure 3.4(b) represent the variance for a single *K* estimate at the centroid of each element in the model domain, with smaller values indicative of higher accuracy of the estimate (Yeh and Liu, 2000). The areas with the highest values of variance (≥ 0.35) correspond to the locations where no hydraulic head observations were available, as discussed above, indicating greater uncertainty in the *K* estimates across this portion of the domain. This suggests that the *K* field is adequately captured near the IE wells, but less information is available further from the pumping wells as expected. Since the focus of this study is on the characterization of the *K* field within the limits of the network of IE wells, these results suggest that the hydraulic observations used in the inverse SSLE model were sufficient to generate the *K* tomogram for the area of interest.

3.4.4 Calibration and Validation of the *K* Tomogram using SSLE

Figure 3.5 shows the changes in simulated and observed steady-state hydraulic head changes produced by the SSHT and K_{eff} scenarios. These scatterplots show data that form three separate zones along the best-fit line with a cluster of data near the origin (0,0), and data clusters near the upper and lower "extremes" of the hydraulic head changes corresponding to the active IE wells. The two "extreme" data clusters at the IE wells show high statistical leverage, as visually indicated by the distance of these isolated clusters from the main cluster near the origin and supported using the quantitative analysis presented by Hoaglin and Welsch (1978). It is recognized that data with high statistical leverage can have a strong influence on the regression results (i.e., estimated slope and r^2 value) (Chatterjee and Hadi, 1986); however, the presence of these high leverage clusters is a direct product of the small spatial scale associated with the area of interest used in this study. It is expected that the data would become more distributed along the 1:1 line as the separation distance between the IE wells was increased.

In the scatterplots associated with the model calibration data, the slope of the best-fit line associated for Test G is 0.83±.05 (standard error) and for Test B is 1.14±.08 (Figure 3.5; Table

3.4). These slopes are not statistically different from unity at the 5% level of significance (LOS). These results suggest that the *K* tomogram is able to adequately reproduce the steady-state observations of hydraulic heads during dipole pumping Test G and Test B which were used in the inverse model to estimate the *K* field.

The other scatterplots (Tests A, C, D, E, F and H in Figure 3.5) represent model validation data and illustrate how well the *K* tomogram generated by the SSLE model was able to predict changes in hydraulic head. The simulated results produced by the SSHT scenario were compared to those from the K_{eff} scenario, which indicate the ability of the bulk *K* estimate to capture the observations of hydraulic head changes during the independent dipole pumping tests. The slopes of the best-fit lines for these six scatterplots produced by the SSHT scenario range from 0.81±.05 to 1.06±.09 (Table 3.4). For the K_{eff} scenario, the slopes of the best-fit lines range from 0.70±.04 to 0.99±.11 across all eight scatterplots representing model validation data (Tests A to H; Table 3.4). With the exception of Test H, the slopes of the best-fit line for the model validation data produced by the SSHT scenario are not statistically different from unity (LOS of 5%), indicating that the hydraulic heads simulated using the *K* tomogram closely resemble those observed during the independent dipole pumping tests. The exception in Test H is presumably the consequence of the observed steady-state hydraulic head changes at the extraction well being lower than those from the rest of the independent dipole pumping tests. In contrast, the slopes of the best-fit lines from the K_{eff} scenario are statistically different from unity (LOS of 5%) for four of the eight independent dipole pumping tests (i.e., Tests C, F, G and H). These results suggest that the *K* tomogram is better able to predict changes in the steady-state hydraulic head than the bulk *K* estimate used in the effective parameter approach. The L_1 norms produced by the SSHT scenario are marginally lower than those determined using the K_{eff} scenario across all the scatterplots associated with model validation, with average L_1 norms of 0.003 m and 0.004 m, respectively (Table 3.4). The L_2 norms, however, are the same for both scenarios (~0.002 m^2). Collectively, these results suggest that the *K* tomogram as a representation of the *K* distribution yields simulated steady-state hydraulic head responses that are marginally superior to those produced by the effective parameter approach compared to the observed hydraulic heads. The difference in performance between the *K* tomogram and K_{eff} is small because the Borden aquifer is mildly heterogeneous. Larger differences have been observed at highly heterogeneous sites (e.g., Berg and Illman, 2011b; Zhao and Illman, 2018).

3.4.5 Transient Flow Simulations

Figure 3.6 shows a scatterplot of the changes in the simulated and observed transient hydraulic head changes produced by the SSHT and K_{eff} scenarios for all IE wells. Similar to the steady-state simulation results, the scatterplots associated with both scenarios show three distinct "bands" of data that are clustered together in horizontally elongated patterns. The two outer "bands" show high statistical leverage (Chatterjee and Hadi, 1986; Hoaglin and Welsch, 1978) and correspond to the hydraulic responses at the active IE wells, while the central "band" is associated with the non-pumping wells. As in the independent dipole pumping test data (Figure 3.5), the presence of these "bands" is due to homogeneous nature of the aquifer and the small spatial scale of the RPM flow system used. It is suspected that the horizontal elongated pattern observed in the outer "bands" is the result of the fluctuations in the hydraulic head observations due to: (1) the dipoles that did not operate in the RPM flow sequence as expected (i.e., fourth and fifth well pairs on Figure 3.3, and the reversed order of sixth and seventh well pairs), and (2) rainfall events that contributed to variations in the water table during the operation of the RPM flow system that were not simulated by the model. The temporal changes in the simulated and observed hydraulic heads at IE-2 and IE-6 are illustrated in Figure 3.7 (see Figure D-5 for the other IE wells). At IE-2, the observed hydraulic head changes show a slight decrease at ~50 hours, while minor fluctuations are noted at IE-6 between 28 to 50 hours that contribute to deviations from the amplitude of peak changes observed at other times. In contrast, the amplitude of the peak changes in the simulated hydraulic heads using the SSHT and K_{eff} scenarios remain constant. The peak changes in the simulated hydraulic heads produced by the SSHT scenario are greater than those from the K_{eff} scenario which is a product of the K estimates that were higher than the expected range in the upper ~0.4 m of the K tomogram (Figure 3.4(a)). The simulated hydraulic heads generated by the SSHT scenario are able to reproduce the amplitude of the observed changes during injection at IE-2 ($t \leq 50$ hours before the decrease in the observed hydraulic heads), and during extraction at IE-6 for the entire simulation duration. Conversely, the amplitude of the observed changes during injection at both of these IE wells are captured by the simulated hydraulic heads generated from the K_{eff} scenario. These results indicate that both the K tomogram and effective parameter approach as representations of the K field are able to capture the temporal changes in the hydraulic responses during the RPM flow protocol.

In total, 1055 and 1051 data points were used to calculate the L_1 and L_2 norms, and R values for the SSHT and K_{eff} scenarios, respectively (Table 3.5). The difference in the number of data is due to the outliers that were removed based on the visual inspection of each scatterplot and statistical analyses of the best-fit line. The slopes of the best-fit line on the scatterplots produced by the SSHT and K_{eff} scenarios were determined to be 1.20±.02 and 0.75±.01, respectively (Table 3.5); both slopes are not statistically different (LOS of 5%) from unity. Unfortunately, the estimates of the L_1 and L_2 norms and R value (Table 3.5) demonstrate a conflicting set of results. The L_1 norms of 0.093 and 0.076 m, and the L_2 norms of 0.027 and 0.022 m^2 for the SSHT and K_{eff} scenarios, respectively, suggest a slightly higher degree of error in the simulated hydraulic head values produced by the SSHT scenario. In contrast, the SSHT and K_{eff} scenarios both yield an R value of ~0.91 indicating a strong correlation between the simulated and observed values of hydraulic head. The discrepancies in the trends observed between these estimates of the L_1 and L_2 norms, and the R value is suspected to be the result of the high statistical leverage apparent in the data. While it is recognized that data with high statistical leverage can have influence on the overall regression results (Chatterjee and Hadi, 1986), we note that these "extreme" data clusters are observed in the simulated hydraulic heads produced by both the SSHT and K_{eff} scenarios, which strongly suggests this trend to be a product of the small spatial scale associated with the area of interest used in this study. Furthermore, the presence of these "extreme" data clusters produced by the SSHT and K_{eff} scenarios implies that both best-fit lines likely contain a similar degree of influence from the high leverage data points. Since the presence of statistical leverage is consistent to the data sets produced by both scenarios, we can assume that the overall findings remain unaffected by this influence. Another potential reason for the slight underperformance of the SSHT scenario was the use of steady state head data for inverse modeling. The inverse modeling of transient head data (i.e., transient hydraulic tomography (THT)) could yield both K and S_s tomograms, which should yield improved predictions of transient heads. The use of THT to further improve site characterization during RPM flows could be investigated in future studies.

These observations suggest that while the SSHT analysis is capable of generating a K tomogram that produces simulated transient hydraulic head responses with good correlation to those observed during RPM flow, the effective parameter approach also yields adequate predictions of hydraulic head responses. Other studies that have used HT analysis to delineate a K field were performed in moderately to highly heterogeneous aquifers with σ^2_{lnK} of ~6.5 (Brauchler et al., 2011; Cardiff et al., 2012; Hochstetler et al., 2015; Paradis et al., 2016; Zhao and Illman, 2018) where the use of a *K* tomogram led to significantly improved predictions of hydraulic head in comparison to the effective parameter approach (Zhao and Illman, 2018). Thus, the apparent ability of both the *K* tomogram and effective parameter approach to predict the transient hydraulic head changes during the RPM flow protocol is the consequence of the relative homogeneous nature of this aquifer ($\sigma^2_{lnK} < 1$) and the small spatial scale of the area of interest used in this study. As the degree of *K* heterogeneity and spatial scale increase, the *K* tomogram as the representation of the *K* distribution is expected to yield improved predictions of the hydraulic responses that more closely resemble those observed during an operation of the RPM flow system than the effective parameter approach.

3.4.6 Impact of the *K* Tomogram on Mixing

To investigate the impact of using the *K* tomogram on the spatial distribution of a hypothetical reagent, various combinations of RPM flow parameters (reorientation angle, Θ, pumping duration, t_p and flow rate, Q) were assessed. During the design process, the spatial distribution of particle trajectories was used as a criterion for the selection of RPM flow parameters. Particle tracking simulations were performed using both the *K* tomogram and effective parameter approach for an RPM flow protocol. These particle trajectories were then compared visually, and quantitatively using the cumulative travel distance. Based on observations from the comparison of particle trajectories produced by the SSHT and K_{eff} scenarios, one or more RPM flow parameter was adjusted to assess whether a higher degree of reagent mixing was feasible. This process was repeated until a specific set of RPM flow parameters generated the most enhanced spatial distribution of particle trajectories.

In all the combinations of RPM flow parameters explored, the SSHT scenario consistently produced complex, intersecting particle trajectories that are significantly more spatially distributed in the area of interest than the K_{eff} scenario. For illustration, a typical simulation result showing the particle trajectories relative to their initial positions are presented in Figure 3.8 for one set of RPM flow parameters ($\theta = 135°$ or $3\pi/4$, $t_p = 45$ minutes, $Q = 4$ m^3/d, $d = 1.75$ m, $N = 18$ and $t = 5$ days). In the SSHT scenario (Figure 3.8(a to d)), all particles move in a direction that corresponds to the reorientation angle used in the RPM flow protocol. The initial direction of particle movement is governed by the location of the first dipole in the pumping schedule, with a slight skew in the pathlines towards the first extraction well. For a period of time (*t* ~0.5 days), the particles travel within the limits of this initial trajectory, which produces regions of denser pathline distributions near the center of the IE well network; however, with increased number of RPM flow cycles, the particles eventually move away from this initial trajectory and produce enhanced spatial coverage in the *x*- and *y*- directions within the area of interest. While the overall particle trajectories show a symmetry related to the relatively homogeneous *K* field of the Borden aquifer (Figure 3.8(e)), the range of *K* values observed within the area of interest, albeit small, produces a distribution that is spatially complex and dense. In the *z*-direction, the particles show an overall change of ~2.5 cm from their initial positions but no intersection of particle trajectories is evident. Conversely, in the K_{eff} scenario (Figure 3.8(f)), all particles remain near their initial positions in the *x*-, *y*- and *z*-directions for the simulation duration ($t = 5$ days). Based on other peer-reviewed studies that have identified reagent mixing as a consequence of the complex distribution of intersecting particle trajectories produced by chaotic advection (Lester et al., 2009; Metcalfe et al., 2010), these results suggest that a greater degree of spreading and mixing of the reagent solution is achieved in the SSHT scenario in comparison to the K_{eff} scenario.

These qualitative observations of particle trajectories are supported by the average cumulative distance travelled by the particles. The incremental change in travel distance during each time step ranges from 0.7 to 5.1 cm for the SSHT scenario, and from 0.3 to 2.0 cm for the K_{eff} scenario. After a simulation period of ~5 days (18 complete cycles of RPM flow, $N = 18$), the average distance travelled by all particles increases linearly towards a cumulative value of 30.54±.65 m and 13.92±.13 m for the SSHT and K_{eff} scenarios, respectively. A comparison of the cumulative travel distances from both scenarios indicate that the particle trajectories produced by the SSHT scenario have longer travel distances, and thus, provide a greater spatial coverage within the area of interest indicative of enhanced reagent mixing. This finding is consistent with other peer-reviewed studies that also used particle tracking methods and demonstrated that reagent mixing is significantly enhanced when chaotic advection is used in a heterogeneous *K* setting (Trefry et al., 2012; Neupauer et al., 2014). Since heterogeneities in the *K* field typically lead to variations in the velocity field and contribute to enhanced reagent mixing (Kitanidis and McCarty, 2012), it is expected that for the same *K* field, an RPM flow system would produce an even greater degree of reagent spreading and mixing than by natural processes (advection and diffusion) alone. As the degree of *K* heterogeneity increases in the area of interest, the particle trajectories are expected to be more complex and asymmetric.

These particle tracking results demonstrate that for the same set of RPM flow parameters, the use of the *K* tomogram leads to significantly enhanced distribution and intersection of particle trajectories in all directions within the area of interest. While both the SSHT and K_{eff} scenarios produced estimates of hydraulic head changes that resemble those observed during the operation of the RPM flow system, the particle tracking results suggest that the improved representation of the variability in the *K* field has important implications on the mixing behavior of a reagent. The improved spatial distribution of particle trajectories indicates that using *K* information applicable to a specific area of interest leads to an effective design of an RPM flow system that can enhance reagent mixing.

3.5 CLOSURE

The results demonstrate that the *K* tomogram determined from the inversion of hydraulic head observations during two independent dipole pumping tests yields simulated estimates of steady-state and transient hydraulic heads that show good correlation to those observed in the area of interest, as defined by the limits of the circular array of IE wells. For the small spatial scale investigated in this relatively homogeneous aquifer, the effective parameter approach was comparable to the *K* tomogram in its ability to simulate changes in hydraulic head that are representative of those observed. While the flow simulations produced a similar range of hydraulic heads using both the *K* tomogram and effective parameter approach as representations of the *K* field, the particle tracking results showed that incorporating the *K* tomogram significantly enhanced the spatial distribution of particle trajectories within the area of interest. The use of the *K* tomogram generated more spatially and densely distributed particle trajectories indicative of enhanced reagent mixing than those produced by the effective parameter approach in which all particles showed minimal change from their initial positions for the entire simulation duration.

The findings from this study demonstrate that the same well system used to invoke chaotic advection can also be used in a HT analysis, providing a viable site characterization tool to delineate the spatial variability of *K* in the area of interest. In addition, using *K* information applicable to a specific area of interest in a groundwater flow model with a particle tracking engine provides a tool that can be used for the design of an effective RPM flow system to promote enhanced reagent mixing. While this proof-of-concept study presents supportive modeling tools for the characterization of the *K* field and the design of an effective RPM flow system, potential limitations of the relative homogeneous nature of the aquifer, and the small spatial scale of the area of interest were noted. For improved robustness of these modeling tools, this study should be extended to a larger area of interest at other field sites of varying degree of heterogeneity where the use of an RPM flow system is anticipated for the generation of chaotic advection to promote enhanced reagent mixing.

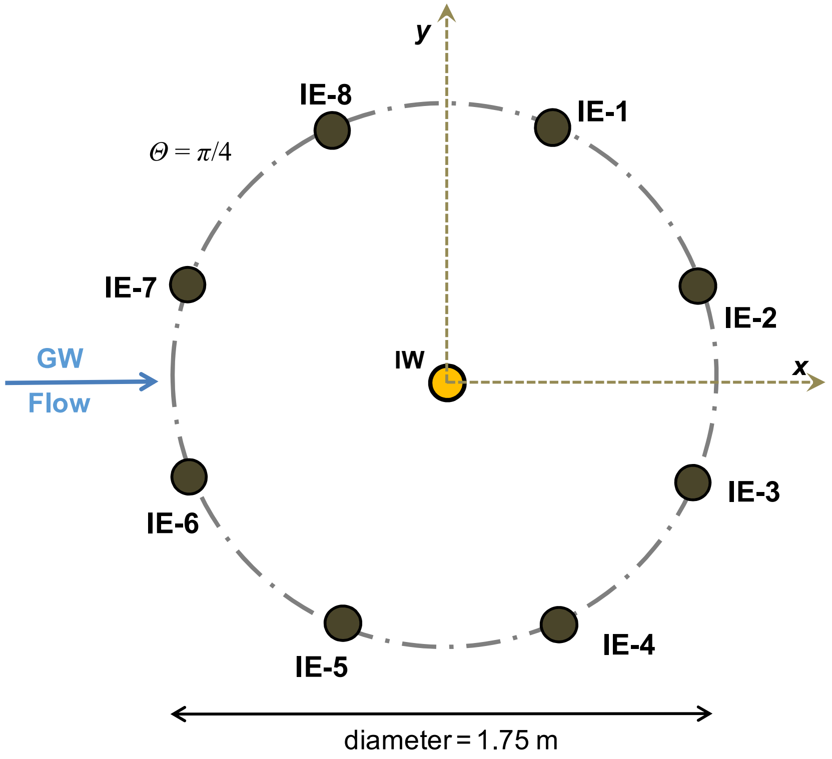

Figure 3.1. Plan view of the circular system of injection/extraction wells (IE-1 to IE-8).

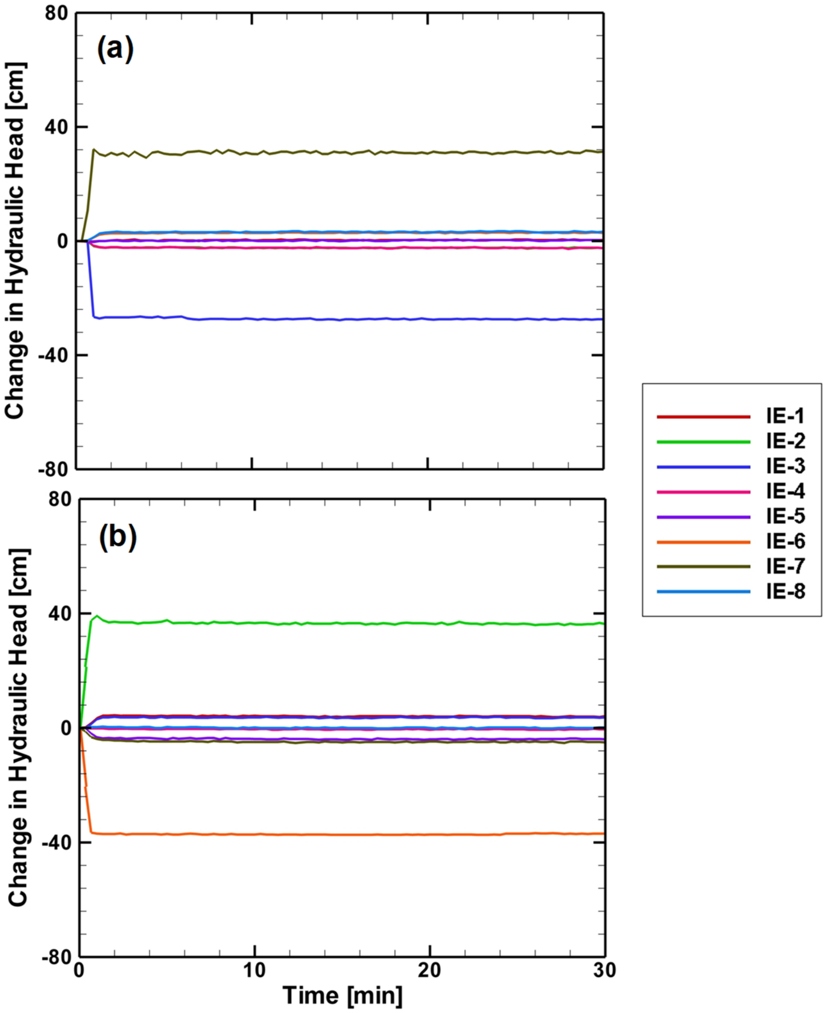

Figure 3.2. Observed changes in hydraulic head at all 8 IE wells for two of the eight independent dipole pumping tests ($Q \sim 3$ L/min) conducted as part of the Stage-1 hydraulic tomography survey: (a) Test G, and (b) Test B (see Table 3.1).

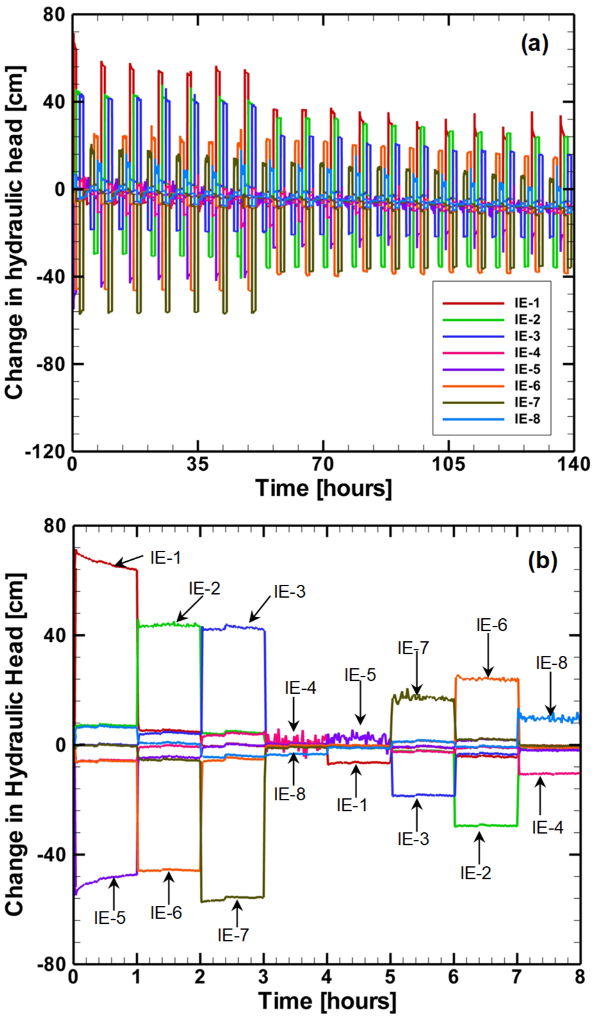

Figure 3.3. Observed hydraulic head changes at the IE wells during the RPM flow protocol for: (a) the entire test duration (140 hours), and (b) the first 8 hours.

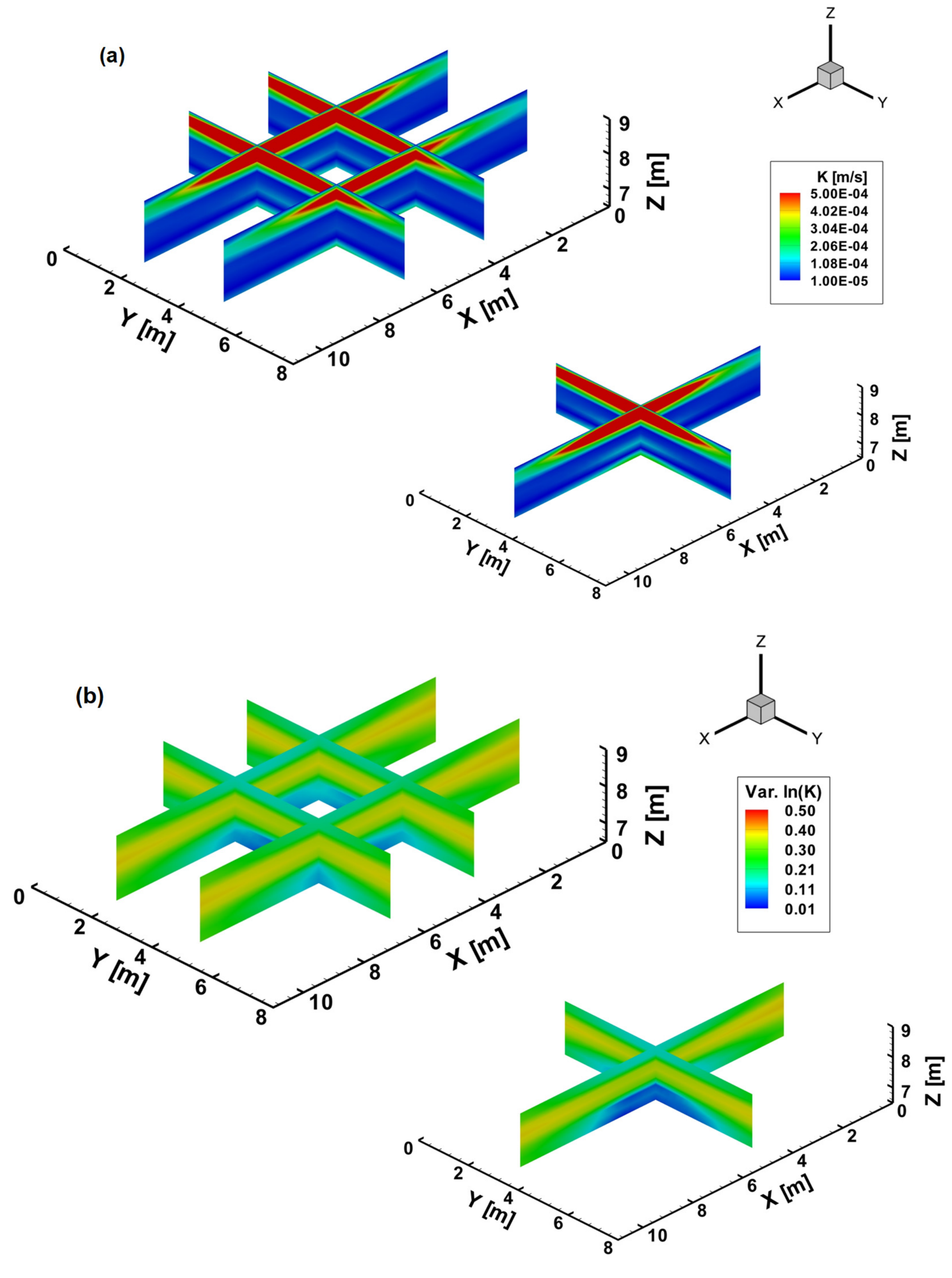

Figure 3.4. (a) *K* tomogram and (b) associated variance across the upper 2 m of the aquifer from the inverse modelling effort using observations from two pumping tests (Test G and Test B). Insets are cross-sections through the middle of the area of interest as defined by the limits of the circular network of IE wells.

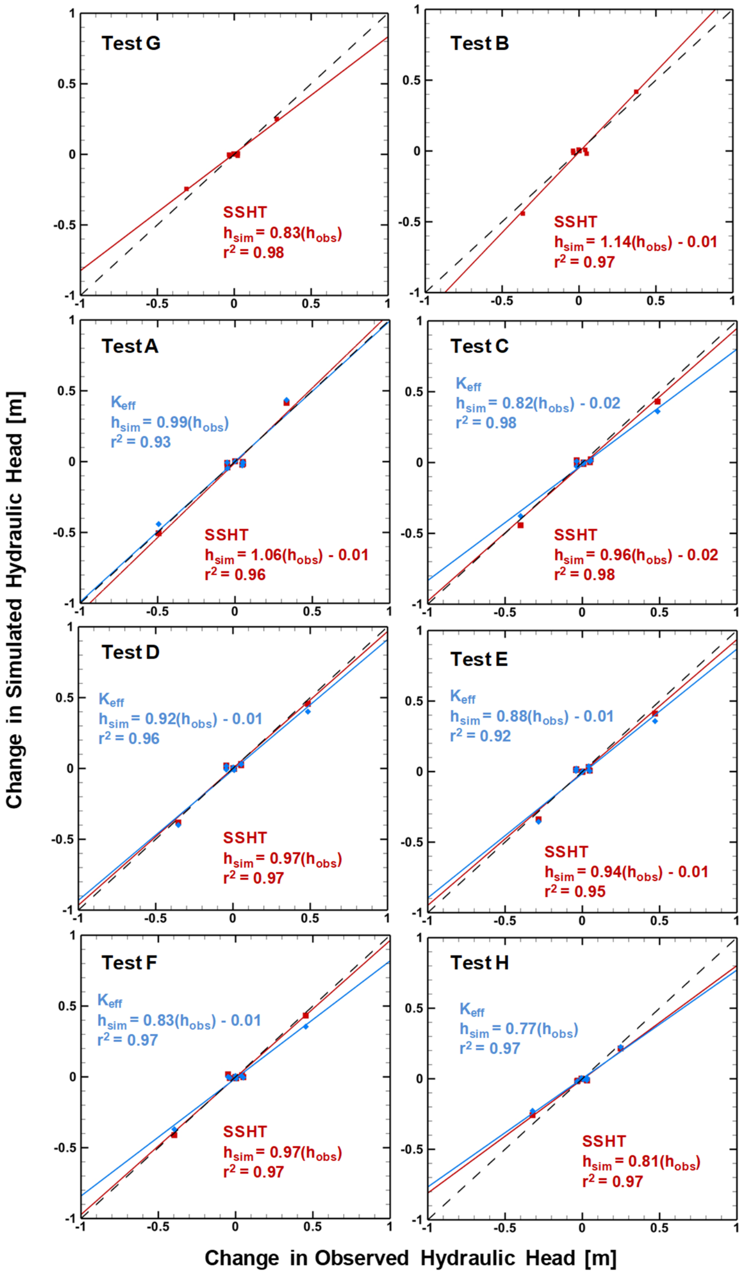

Figure 3.5. Scatterplots of observed and simulated steady-state hydraulic head changes at all IE wells produced by the SSHT and K_{eff} scenarios for the independent dipole pumping tests. The dotted line is a 1:1 line indicating a perfect match between observed and simulated values, while the solid line is the best-fit regression. For the SSHT scenario, scatterplots associated with Tests G and B (top panels) represent model calibration data. The scatterplots for the other six tests represent model validation data, and are compared to the K_{eff} scenario which illustrates the ability of the bulk K estimate determined from the single well pumping and slug tests to capture observations of hydraulic head changes during the independent dipole pumping tests.

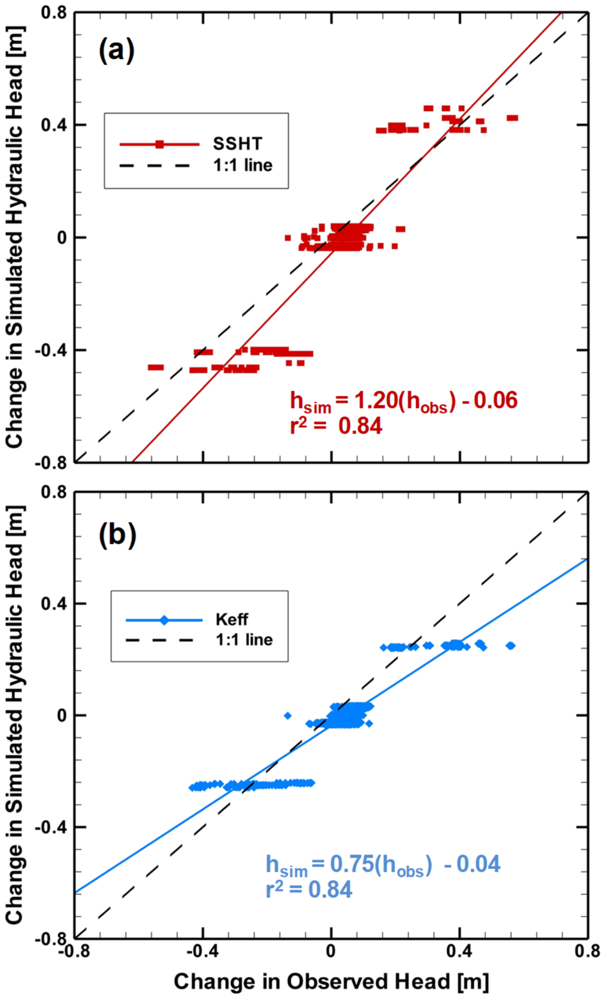

Figure 3.6. Scatterplot of observed and simulated transient hydraulic head changes at all IE wells during RPM flow produced by the: (a) SSHT and (b) K_{eff} scenarios. The dotted line is the 1:1 line indicating a perfect match between observed and simulated values, while the solid line is the best linear fit to the data.

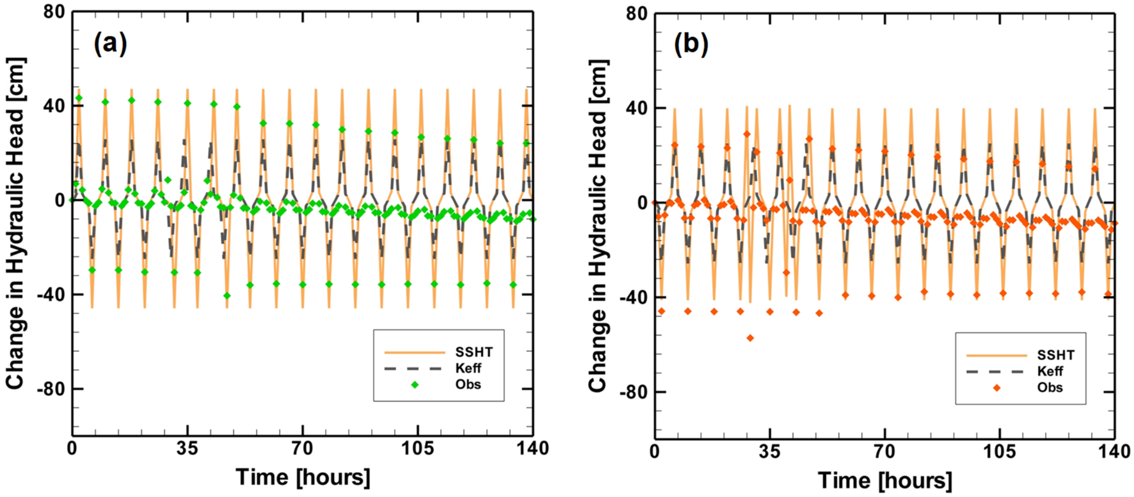

Figure 3.7. Temporal hydraulic head changes in IE-2 and IE-6 during implementation of the RPM flow protocol conducted as part of the Stage-2 hydraulic tomography survey. The solid orange lines are the simulated hydraulic head changes produced by the SSHT scenario, while the dotted grey lines are those produced by the K_{eff} scenario. The symbols represent the observed hydraulic head changes.

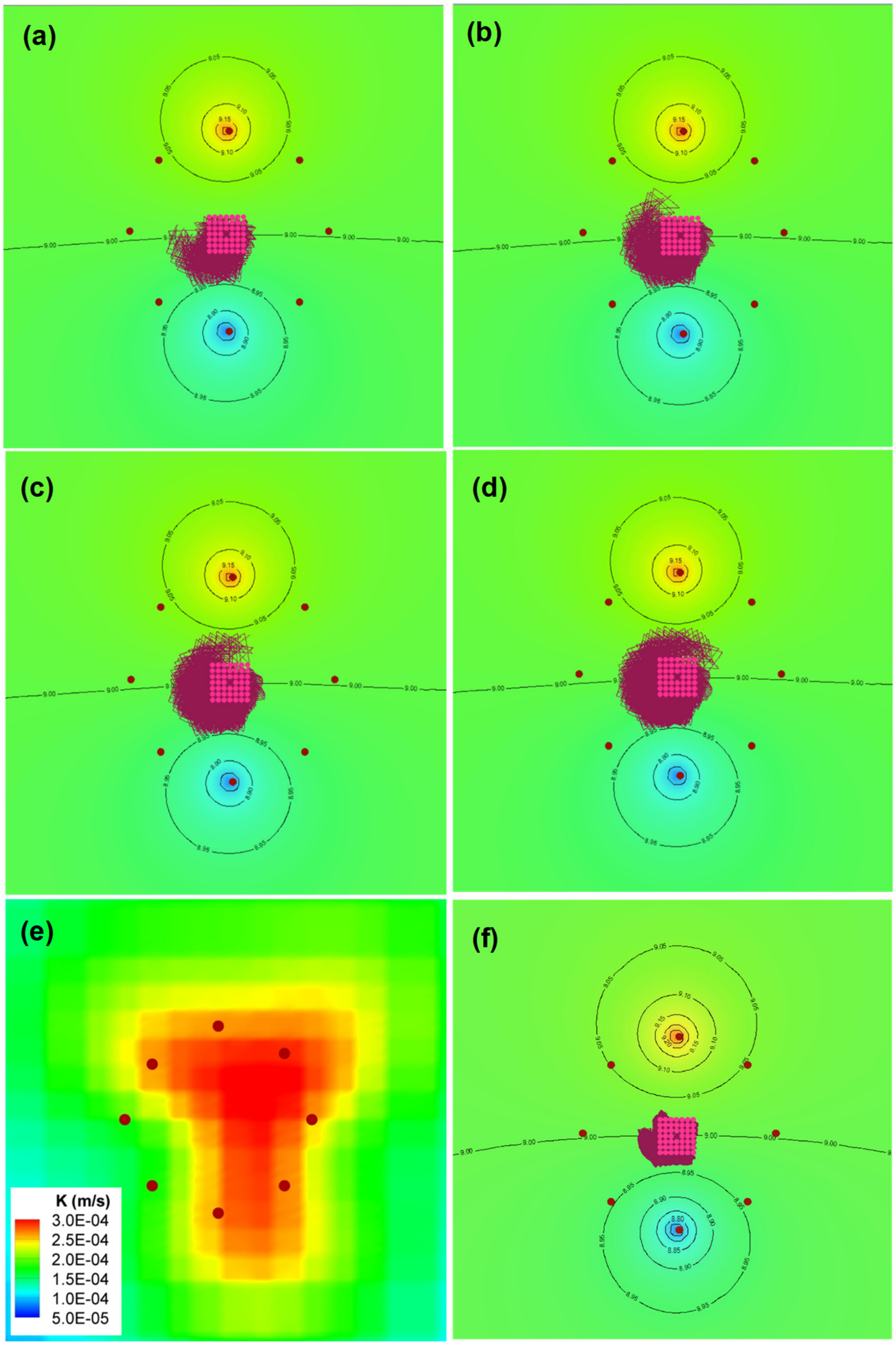

Figure 3.8. Hydraulic head contours (black lines) at t = 45 minutes for illustration purposes, and simulated particle trajectories (purple lines) at the depth corresponding to the midpoint of the well screen produced by the SSHT scenario (a-d) after 1 day, 2 days, 3 days and 4 days of RPM flows, respectively, with the K field of the layer in which the particles were assigned (e), and by the K_{eff} scenario (f) at the end of the simulation (for $\theta = 135°$ or $3\pi/4$, t_p = 45 minutes, $Q = 4$ m^3/d, d = 1.75 m and N = 18). Red symbols indicate the location of the IE wells, and the pink symbols indicate initial position of particles.

Table 3.1. Injection/extraction well pairs involved in the independent dipole pumping tests (Stage-1 of the hydraulic tomography survey).

Test ID	**Injection Well**	**Extraction Well**
A	1	5
B	2	6
C	3	7
D	4	8
E	5	1
F	6	2
G	7	3
H	8	4

Table 3.2. Summary of input parameters used in the SSLE model for the SSHT analysis.

Input Parameter	**Assigned Value**
Effective porosity [a]	0.33[a]
Bulk density (g/m^3) [a]	1.81[a]
Hydraulic conductivity (m/s) [b]	7x10^{-5}
Correlation length, λ_x, λ_y (m) [b]	4.75
Correlation length, λ_z (m) [b]	0.2
Variance of lnK, $\sigma^2_{\ln K}$ [b]	0.6

[a] Mackay et al., 1986

[b] Represents an average of the values reported in Sudicky, 1986; Woodbury & Sudicky, 1991; Rivett et al., 1994; Turcke & Kueper, 1996; Tomlinson, 2003

Table 3.3. Summary of K estimates from the single well pumping and slug tests.

Well ID	**K (m/s)**	
	Single Well Pumping Test	Slug Test
IE-1	5.90x10^{-5}	4.67x10^{-5}
IE-2	5.83x10^{-5}	5.37x10^{-5}
IE-3	6.56x10^{-5}	6.18x10^{-5}
IE-4	6.52x10^{-5}	5.60x10^{-5}
IE-5	6.89x10^{-5}	7.13x10^{-5}
IE-6	5.30x10^{-5}	5.23x10^{-5}
IE-7	7.60x10^{-5}	4.12x10^{-5}
IE-8	5.95x10^{-5}	5.55x10^{-5}
Geometric mean	6.28x10^{-5}	5.42x10^{-5}

Table 3.4. Best-fit linear regression parameters, and L_1 and L_2 norms of observed versus simulated steady-state hydraulic head estimates produced by the SSHT and K_{eff} scenarios for the independent pumping tests. For the SSHT scenario, Tests G and B represent model calibration data, and the other six tests (A, C, D, E, F and H) represent model validation. All eight tests (A to H) represent model validation data for the K_{eff} scenario.

Test ID	**SSHT**					**K_{eff}**				
	slope	intercept	r^2	L_1	L_2	slope	intercept	r^2	L_1	L_2
G	0.83±.05	0.00±.01	0.98	0.025	0.001	0.70±.04	0.00±.01	0.99	0.033	0.002
B	1.14±.08	-0.01±.02	0.97	0.038	0.002	0.98±.06	0.00±.01	0.97	0.024	0.001
A	1.06±.09	-0.01±.02	0.96	0.042	0.003	0.99±.11	0.00±.02	0.93	0.049	0.003
C	0.96±.06	-0.02±.01	0.98	0.035	0.002	0.82±.05	-0.02±.01	0.98	0.038	0.003
D	0.97±.07	0.00±.02	0.97	0.031	0.001	0.92±.07	-0.01±.02	0.96	0.037	0.002
E	0.94±.08	-0.01±.02	0.95	0.035	0.002	0.88±.10	-0.01±.02	0.92	0.043	0.003
F	0.97±.06	0.00±.01	0.97	0.029	0.001	0.83±.06	-0.01±.01	0.97	0.041	0.002
H	0.81±.05	0.00±.01	0.97	0.028	0.001	0.77±.06	0.00±.01	0.97	0.029	0.002

Table 3.5. Best-fit linear regression parameters, values of L_1 and L_2 norms, *R,* and percentage of outliers in the observed versus simulated transient hydraulic head estimates produced by the SSHT and K_{eff} scenarios during RPM flow.

	slope	**intercept**	r^2	L_1	L_2	***R***	**% outliers**[1]
SSHT	1.20±.02	-0.06±.00	0.84	0.093	0.027	0.914	9.9
K_{eff}	0.75±.01	-0.04±.00	0.84	0.076	0.022	0.916	10.3

[1] Represents the number of data points that were statistically identified as an outlier divided by the total number of data points.

Chapter 4

The Role of Rotated Potential Mixing Protocols on the Behavior of a Conservative Reagent

Abstract

Chaotic advection is defined as the generation of "small-scale structures” from the repeated stretching and folding of fluid elements in a laminar flow regime that has the potential to enhance mixing in the subsurface and improve effectiveness of *in situ* treatment. Rotated potential mixing (RPM) flow is one configuration which has been used to invoke chaotic advection in porous media. An RPM flow system involves periodically re-oriented dipole flow through the transient switching of pressures at a series of radial wells. In this study, we relied on a conventional modeling approach (e.g., MODFLOW, MODPATH and MT3DMS) to represent the expected flow and transport behavior of a conservative reagent subjected to chaotic advection by an RPM flow system, and then used this approach to explore the impact of specific engineering controls of an RPM flow system on reagent mixing behavior. The multiple lines of evidence assembled in this study demonstrated that this modeling approach captured the key features of the expected transport behavior reported in other studies of chaotic advection (e.g., theory, laboratory and field). Visual observations from the reagent distribution produced, and the results from the quantitative metrics of mixing behavior highlighted the different responses that are possible by the various combinations of RPM flow parameters explored. For example, the flow rate and pumping duration were identified as key parameters of an RPM flow system that have direct consequences on the degree of reagent spreading and mixing. The use of the same RPM flow protocol in a heterogeneous *K* field led to significantly greater degree of reagent mixing than in a homogeneous *K* setting. The findings demonstrated the importance of combining theoretical considerations with practical limitations when designing an RPM flow system. To the best of our knowledge, this study is the first attempt to use a conventional modeling approach to simulate the transport behavior of a conservative reagent specifically for an RPM flow system. The findings represent a significant step towards the development of a modeling approach for the design of an effective RPM flow system that can support field implementation of chaotic advection and promote enhanced reagent mixing.

4.1 INTRODUCTION

In situ treatment commonly involves the creation of a reactive zone by injecting a reagent into the subsurface, which leads to the mass destruction of contaminants. Examples of such *in situ* treatment methods include chemical oxidation (Siegrist et al., 2016) and enhanced bioremediation (Reinhard et al., 1997). In these injection-driven remedial technologies, the design of an effective delivery system is a key requirement for success. Following the injection of a reagent solution into the subsurface, contact between the injected reagent and contaminant(s) must be achieved by transport processes for desired chemical or biological transformations to occur. This contact between the injected reagent and contaminant is the desired outcome of an effective delivery system; however, it remains a significant challenge to achieve (Kitanidis and McCarty, 2012).

In relevant literature, mixing and spreading are understood to be distinct processes. *Spreading* is associated with the deformation of a reagent plume that provides additional opportunities for contact with the contaminant, while *mixing* (or dilution) is a result of various mechanisms (e.g., sorption/desorption, diffusion) that cause the reagent and contaminant to overlap and produce uniform concentrations (Kitanidis, 1994; Aref et al., 2017). Spreading contributes to an increase in the overall zone across which the reagent and contaminant can come into contact (Jose and Cirpka, 2004); however, preferential flow pathways exist at a range of spatial scales due to subsurface heterogeneities (Dagan, 1986; Scheibe and Yabusaki, 1998), and lead to uneven spatial distribution of the injected fluid. For conventional injection methods using vertical wells, the reagent follows the path of least resistance from the wellbore into the porous medium. As a result, the reagent distribution will be greater in zones of higher hydraulic conductivity (K) and bypass adjacent areas of lower K (Saenton et al., 2002; Payne et al., 2008; Zhong et al., 2011). While molecular diffusion ($D^* \sim 10^{-9}$ m^2/s) is possibly the primary transport mechanism that can bring the injected reagent and contaminant together in these lower K zones (Jose and Cirpka, 2004; Gale et al., 2015), diffusion is a slow process and contributes to inefficient mixing (Kitanidis and McCarty, 2012). Partial removal of the contaminant mass is one possible consequence of ineffective reagent delivery in source zones, which can eventually lead to rebound in contaminant levels and persistence of plumes (Thomson et al., 2008). In light of these challenges associated with injection-driven *in situ* remediation efforts, there is a need for a novel approach that can enhance mixing.

The concept of chaotic advection (Trefry et al., 2012; Aref et al., 2017) has the potential to overcome preferential flow paths and enhance mixing in the subsurface. Chaotic advection has been defined as the generation of "small-scale structures” from the repeated stretching and folding of fluid elements in a laminar flow regime (Ottino, 1989; Aref et al., 2017). This stretching and folding of individual fluid elements produces complex, intersecting particle trajectories which have been theorized to enhance solute spreading in porous media and increase the zone of contact across which reactions can occur (Ottino, 1989; Bagtzoglou and Oates, 2007; Lester et al., 2009; Metcalfe et al., 2011; Mays and Neupauer, 2012). The “small-scale structures” are equivalent to fluid elements that are stirred and stretched into a length scale small enough for diffusion to produce efficient mixing (Aref et al., 2017). Thus, reagent delivery and treatment effectiveness may be significantly improved if chaotic advection can be invoked and controlled *in situ* (Bagtzoglou and Oates, 2007).

One configuration which has been theoretically and experimentally used to invoke chaotic advection in porous media is termed rotated potential mixing (RPM) flow (Metcalfe et al., 2008). A conventional RPM flow system involves periodically re-oriented dipole flow through the transient switching of pressures at a series of radial wells in a completely closed flow system in which the fluid removed at the extraction well is immediately re-injected into the injection well (Trefry et al., 2012). In an RPM flow protocol, a dipole involving one injection and one extraction well separated by 180°, operates for a fixed time (t_p). This dipole is then instantaneously changed by a reorientation angle (Θ) and resumes pumping for t_p. A repeated sequence of this transient, re-oriented dipole pumping will eventually cause the flow regime to become chaotic (Lester et al., 2009; Metcalfe et al., 2010). The pumping duration (t_p), reorientation angle (Θ), and flow rate (Q) are key parameters in an RPM flow system (Metcalfe et al., 2010), which can be used to create either zones of enhanced mixing or confinement (Trefry et al., 2012).

Since its introduction by Aref (1984) and Ottino (1989) who mathematically demonstrated that chaotic advection can be achieved in a laminar flow regime by introducing time-dependence to the flow field, several peer-reviewed studies have theoretically investigated chaotic advection in porous media. Using particle tracking methods, Trefry et al. (2012) showed that chaotic advection can be generated using an RPM flow system to produce both regions of enhanced mixing and confinement in a synthetic aquifer while withstanding the impact of a local hydraulic gradient. Their work also reported that aquifer heterogeneities contribute to enhanced mixing of reagents; however, a highly heterogeneous aquifer ($\sigma^2_{lnK} > 4$) led to the solute eventually moving outside the network of injection/extraction wells. Sposito (2006) used a particle tracking approach to demonstrate that chaotic advection can be generated near a vertical recirculation well with a time-dependent flow field, which led to enhanced solute spreading. Bagtzoglou and Oates (2007) used the random walk particle tracking method to show that chaotic advection can be achieved using a system of three wells oscillating between injection and extraction with flow rates that vary over time. Mays and Neupauer (2012) used MODFLOW-2000 (Harbaugh et al., 2000) coupled with MODPATH (Pollock, 1994) to simulate an engineered sequence of injections and extractions as an example of a time-dependent flow field in a synthetic aquifer, and observed chaotic advection and enhanced solute spreading. Neupauer et al. (2014) also used MODFLOW-2000 coupled with MODPATH to simulate an engineered injection-extraction sequence (Mays and Neupauer, 2012) in a synthetic heterogeneous aquifer. Their results demonstrated that plume spreading is significantly enhanced when chaotic advection is combined with a heterogeneous *K* field. Rodriguez-Escales et al. (2017) simulated the engineered injection-extraction sequence reported by Mays and Neupauer (2012) using MODFLOW-2005 (Harbaugh, 2005) and PHT3D (Prommer and Post, 2010), which couples the transport engine of MT3DMS (Zheng and Wang, 1999) with the geochemical model PHREEQC-2 (Parkhurst and Appelo, 1999). These results showed that their engineered injection-extraction sequence is capable of generating chaotic advection in a synthetic aquifer with a heterogeneous *K* field which leads to enhanced reagent spreading.

Several peer-reviewed studies have demonstrated the use of various modeling methods to provide theoretical evidence of chaotic advection in porous media and its impacts on solute mixing. Most of these studies have focused on advective particle tracking approaches to gain insight into chaotic mixing behavior, and there are limited efforts to perform transport simulations for an RPM flow system using conventional modeling methods based on mass balance considerations. The objectives of this study were to (1) investigate whether a conventional modeling method can capture the transport behavior of a conservative reagent in the presence of chaotic advection using an RPM flow system, and then (2) use this model to explore the impact of specific engineering controls associated with an RPM flow system on reagent mixing. To the best of our knowledge, this is the first attempt to simulate the transport behavior of a conservative reagent specifically for an RPM flow system. The findings from this study represent a critical step in the development of a modeling tool to provide insight into the engineering controls of an RPM flow system that can generate chaotic advection and enhance reagent mixing.

4.2 MODELING APPROACH

The transport behavior of a conservative reagent subjected to chaotic advection was simulated within an area of interest as defined by the limits of eight injection/extraction wells placed in a circular array (Figure 4.1). This area of interest was chosen to represent a target treatment zone within a shallow aquifer system that is hydraulically isolated from the ambient groundwater flow. An integrated two-dimensional (2D) model was assumed sufficient to represent the spatial domain, thus providing an opportunity to perform focused, in-depth investigations of the engineering controls associated with an RPM flow system. Transport simulations consisted of an initial injection of a conservative reagent in the center of the circular array of wells, followed by the activation of an RPM flow protocol. Breakthrough curves (BTCs) at a series of observation well locations, and the spatial distribution of the reagent concentration within the area of interest were generated using a set of RPM flow parameters representing the baseline scenario. Various scenarios were simulated to explore the impact of specific engineering controls associated with an RPM flow system (e.g., pumping duration (t_p), reorientation angle (Θ), and flow rate (Q)) on reagent mixing within the area of interest. Results from each scenario were visually compared using the simulated reagent concentration contours, and quantitatively using metrics adopted to establish reagent mixing behavior (Cho et al., 2018). Particle tracking was performed for the baseline scenario and observations compared to the expected behavior of theoretical diagnostic tools that have been reported in other studies to demonstrate the presence of chaotic advection.

4.2.1 Groundwater Flow and Transport Simulations

Groundwater flow was simulated using the MODFLOW-2005 engine in Visual MODFLOW® Flex (Version 2015.1; Waterloo Hydrogeologic, Kitchener, Ontario, Canada). The Conjugate Gradient Solver (CGS) was used with a convergence criterion of 10^{-6} m. The cell-by-cell flow budget file generated by MODFLOW was subsequently used in MT3DMS (Zhang and Wang, 1999) to simulate the transport of the conservative reagent under chaotic flow conditions. The

Method of Characteristics (MOC) was implemented as the solution technique in MT3DMS since it has been shown to minimize issues of numerical dispersion typically observed in advection-dominated systems with temporally evolving complex-flow patterns (Garder et al., 1964; Zhang and Wang, 1999). The MOC method was combined with the implicit Generalized Conjugate Gradient Solver (GCG) package using a convergence criterion of 10^{-6}.

A rectangular spatial domain (8 m wide by 11 m long) was chosen to represent the shallow aquifer system with a thickness of 1 m. The central portion of the domain corresponding to the area of interest, and where the pumping wells were located, was discretized with 0.01 m by 0.01 m grid blocks. Outside this central portion, the size of the grid blocks was increased to 0.02 m by 0.02 m. The resulting finite difference grid was composed of 650 rows and 850 columns, and was considered to provide appropriate spatial resolution to satisfy the objectives of this investigation.

No-flow boundary conditions were assigned to the bottom and along the outer boundaries of the model domain to represent a hydraulically isolated condition. Eight (8) injection/extraction pumping wells (identified as IE-1 to IE-8; Figure 4.1) were assigned in a circular array with a diameter of 5 m, and a time-dependent pumping schedule that corresponds to the well pair involved in the RPM flow protocol. One additional well (identified as IW) was also assigned at the center of the circular network of IE wells for the initial injection of the conservative reagent solution into the model domain (Figure 4.1). Uniform values of hydraulic conductivity ($K_{xx} = K_{yy} = 8.5\text{x}10^{-5}$ m/s) and specific yield ($S_y = 0.33$) were assigned across the entire spatial domain. At the beginning of each simulation the reagent concentration in the model domain was assigned to be zero.

Each transport simulation began with the injection of a conservative reagent (C_o = 1 g/L) into the model domain using IW with an injection rate of 3.5 L/min. The injection volume (1250 L) was selected to achieve a coverage within the area of interest representing ~60% of the pore volume in the center if the network of IE wells. Following injection, an RPM flow protocol was initiated using the IE wells. Transport simulations were performed using an initial set of RPM flow parameters representing the baseline scenario in which an IE well pair was operated for t_p = 4 hours at Q_{RPM} = 5 m^3/d. After duration t_p, the active dipole was turned off and rotated by the reorientation angle (Θ = 45°) before pumping resumed at the new dipole using the same t_p and

Q_{RPM}. This periodically re-oriented dipole pumping was repeated around the IE well network 12 times ($N = 12$), which corresponds to a simulation duration of 384 hours (or 16 days). Additional scenarios (identified as S1 to S6 in Table 4.1) were then simulated to explore the impact of specific engineering controls of an RPM flow system (e.g., t_p, Θ, and Q) on the reagent mixing behavior. For all scenarios designed to demonstrate enhanced mixing, the specific RPM flow protocol was determined based on the theoretical parameter, q, reported by Lester et al. (2010) which provides an estimate of the degree of mixing possible in a system for a given set of Θ, t_p and Q (Figure E-1).

All scenarios are based on the same configuration of IE wells (i.e., eight IE wells with $D = 5$ m), but with changes to specific RPM flow parameters to demonstrate the impact on the spatial distribution and mixing behavior of the reagent. For example, Scenarios S1 and S2 explore the impact of the reorientation angle, Θ, while Scenarios S3 and S4 investigate pumping duration, t_p. In addition, Scenario S5 explores whether a specific set of RPM flow parameters can produce confinement of the reagent within the area of interest. Scenario S6 uses the same set of RPM flow parameters as Scenario S2, but instead of a homogenous K distribution, the influence of a spatially correlated K distribution on chaotic flow and transport behavior was investigated. Two mildly heterogeneous K fields (geometric mean of 8.5×10^{-5} m/s, variance of the $\ln(K)$ of 0.5) generated with FGEN92 (Robin et al., 1993) were employed for comparison. The K field for Scenario S6-A was generated with a *x*- and *y*-correlation length of 0.5 m, while the K field for Scenario S6-B was generated with a *x*- and *y*-correlation length of 0.1 m (Figure E-2).

The transport simulation results were post-processed to generate BTCs at six (6) hypothetical observation wells (OBS-1 to OBS-6) within the area of interest. The location of these observation wells (Figure 4.1) were chosen to capture the transient changes in the spatial distribution of the reagent. Simulated concentrations were imported into Tecplot 360 (Tecplot Inc., Bellevue, Washington, USA) for visualization and analysis. Contours of the reagent concentrations were generated by using the inverse distance weighting scheme (exponent of 3.5, and 8 neighboring data points distributed throughout the surrounding 8 octants) to interpolate the simulated concentrations in the model domain to a uniform grid consisting of 600 by 600 rows and columns, respectively.

To assess the ability of this model to capture key features of the expected transport behavior, the simulation results must be supported by the presence of chaotic advection in the system as indicated by the theoretical methods reported in relevant literature. Since the published diagnostic tools typically used to characterize chaotic advection are applied by analyzing individual particle trajectories over time and space (Ottino 1990), the groundwater flow model was extended to include particle tracking using the MODPATH engine (Pollock, 1994). 2500 forward-tracking particles were assigned to the cells adjacent to the center of the circular network of IE wells. These initial particle positions are representative of the approximate location of the hypothetical reagent solution injected by IW.

4.2.2 Model Post-Processing

4.2.2.1 Theoretical Diagnostic Tools of Chaotic Advection

To demonstrate whether chaotic advection is present in this system, two diagnostic methods were used to analyze the particle tracking simulation results for the baseline scenario: the Poincaré section and Lyapunov exponent. The Poincaré section displays particle positions at discrete time intervals and provides a visual representation of chaotic advection based on the patterns that emerge (Ottino, 1989; Lester et al., 2009). The discrete time interval was chosen to be multiples of the RPM flow period, expressed as one complete cycle around the circular injection/extraction well network (Trefry et al., 2012). Poincaré sections were constructed by plotting the superimposed particle coordinates generated from the MODPATH engine after each iteration of the RPM flow period for the entire simulation duration ($N = 12$).

Chaotic advection can also be characterized by the exponential divergence of particles from their initial conditions (Ottino, 1989), which is observed as a growth in the distance between a pair of initially nearby particles (Mays and Neupauer, 2012). This exponential rate of stretching is quantified by the finite-time Lyapunov exponent given by

$$\lambda = \left(\frac{1}{N}\right) \ln \left[\frac{d(N)}{d(0)}\right] \tag{4.1}$$

where $d(N)$ is the separation distance of a pair of particles after N iterations of the RPM flow period, and $d(0)$ is the initial separation distance (Tabor, 1989; Jones and Aref, 1988). Since the

Lyapunov exponent is zero in steady flows, values of $\lambda > 0$ would indicate the presence of chaotic advection (Dentz et al., 2017; Trefry et al., 2018).

4.2.2.2 Quantitative Metrics of Mixing

To assess the impact of specific RPM flow parameters on the mixing behavior of the reagent, two quantitative metrics were used to analyze the simulated concentrations within the network of IE wells: (1) the second spatial moments of the reagent concentration distribution ($s_x^2,\ s_y^2$), and (2) the concentration variance (s_C^2) (Cho et al., 2018a). The first spatial moment of a reagent concentration distribution represents the mean location of the centroid of the reagent mass, and the second spatial moment provides an estimate of the degree of spreading around the centroid (Kitanidis, 1988; Le Borgne et al., 2010). As mixing progresses, it is expected that the centroid ($\overline{x}_c$, $\overline{y}_c$) of the reagent distribution would remain near IW (the origin), and increases in the second moment ($s_x^2,\ s_y^2$) would be indicative of an enhanced spatial distribution of the reagent within the area of interest. The spatial concentration variance is a measure of mixing that describes the variability across the concentration field, and can be used to quantify the degree of mixing in a system (Kapoor and Kitanidis, 1998; Pannone and Kitanidis, 2001; Dentz et al., 2017). As the system becomes well-mixed and uniform concentrations are achieved across the area of interest, s_C^2 is expected to approach zero (Sposito, 1998).

4.3 RESULTS AND DISCUSSION

4.3.1 Reagent Transport Behavior for the Baseline Scenario

Figure 4.2 shows the simulated reagent spatial distribution at 6 different times during the 384 hour simulation of the RPM flow system used for the baseline scenario. After injection ($N = 0$), as expected, the reagent distribution manifests as a circle in the center of the IE well network, with a concentration of ~1 g/L (indicated by the red region on Figure 4.2). With the implementation of the RPM flow system, the reagent distribution undergoes significant stretching and spreading asymmetrically. The reagent distribution shows a skew towards the extraction wells involved in the first three dipoles of the RPM flow sequence (Table 4.3), with three "tails" that form towards IE-5, IE-6 and IE-7 after one complete cycle of RPM flow ($N = 1$ on Figure 4.2). As the number of RPM flow cycles increase ($N = 2$ and 5 on Figure 4.2), these "tails" become more pronounced and the overall shape of the reagent distribution becomes stretched diagonally. At the end of the simulation (*N* = 12 on Figure 4.2), eight "tails" are visible corresponding to each extraction well in this RPM flow protocol, and lower levels of concentrations (yellow to green) are observed across the reagent distribution. The central red region initially present at the end of injection is reduced to a small orange area at the core of the reagent distribution.

The simulated BTCs at all six observation wells, OBS-1 to OBS-6 (Figure 4.3) show an oscillatory behavior as a result of the periodic switching in the RPM flow system that causes the reagent mass to move in and out of the observation well vicinity. This oscillatory BTC behavior has previously been observed in other laboratory and field investigations using an RPM flow system, and identified to be a necessary precursor of chaotic advection (Lester et al., 2010; Cho et al., 2018(a)). A Fourier transform of the simulated breakthrough concentrations at these observation wells (Figure 4.4) reveal a continuous frequency spectrum composed of many smaller, irregular peaks rather than a few distinguishable dominant frequencies. Since a chaotic signal has many different frequency components that persist across the spectrum (Moon, 2008), these results suggest the presence of chaos as a result of the imposed RPM flow.

At the observation well adjacent to IW (OBS-1), C/C_o is initially at unity after injection ($t = 0$ on Figure 4.3) and decreases in an oscillating manner to a peak amplitude of 0.8 at the end of the simulation duration ($t = 16$ days). Similarly, at OBS-2 and OBS-4, located 1.1 m away from IW, C/C_o begins at unity and declines to a final peak amplitude of 0.62 and 0.76, respectively. At the observation wells located 1.7 m from IW (OBS-3, OBS-5, and OBS-6), the simulated BTCs show variability in the breakthrough behavior. At OBS-5, C/C_o begins at 0.76 and declines to a final peak amplitude of 0.32, which is reflective of the elongated "tails" that form towards the left side of the circular array of IE wells from the imposed RPM flow (discussed above). In contrast, the peak amplitude of C/C_o at OBS-3 remains at ~0.30 for the simulation duration, while at OBS-6, C/C_o increases from an initial value of zero to a final peak amplitude of 0.16. The variability in the breakthrough behavior across the observation wells with the same separation distance from IW suggests that the transport behavior of the reagent solution does not directly correspond to distance, but rather driven by the stretching and spreading of the reagent plume as a result of the complex flow fields generated by the RPM flow system.

The visual observations of the simulated reagent distribution (Figure 4.2) are consistent with the fluorescence images of an injected and emplaced fluid captured from a laboratory-scale experimental cell designed to generate chaotic advection using the same reorientation angle but at a smaller spatial scale (Metcalfe et al., 2010). The simulated reagent distribution also demonstrates similarities to the topology of the corresponding Poincaré section (Figure 4.5) which shows superimposed particle positions after each iteration of the RPM flow period for 12 complete cycles around the IE well network (N = 12). The Poincaré section for this baseline scenario illustrates particle positions that manifest as well-defined "boundaries", corresponding to outer limits of the reagent distribution. Similar to the simulated reagent distribution (Figure 4.4), the Poincaré section shows elongated "tails" in the direction of the first three extraction wells of the RPM flow sequence. While the Poincaré section shows less number of "tails" which are more stretched out in the direction of the extraction wells than the simulated reagent distribution, this is a direct result of the advective particle tracking engine used to generate the Poincaré section. Conversely, the reagent distribution is determined using simulated concentrations that are a product of advection and dispersion. The overall similarities observed between the simulated reagent distribution, the Poincaré section and the results from a previous laboratory experiment strongly suggest that this model is able to reproduce the key characteristics of the reagent transport behavior in an RPM flow system.

The interpretation of the transport simulation results is supported by the presence of chaotic advection using theoretical diagnostic methods. For instance, a closer look at the Poincaré section (Figure 4.5, inset) illustrates particles that deviate from their positions at the previous RPM flow cycle, and produce a distribution around the "boundaries". This observation is consistent with the expected behavior reported by Trefry et al. (2012) where they identified two different regions in the Poincaré section that can be generated by an RPM flow system: a "chaotic sea of particles" and/or "boundaries", corresponding to zones of enhanced mixing and confinement, respectively. The Lyapunov exponents determined for 50 particle pairs arbitrarily chosen with initial separation distances ≤ 0.02 m also demonstrate the expected behavior in the presence of chaotic advection. For illustration, a typical simulation result showing the Lypunov exponents for six out of the 50 particle pairs are presented in Figure 4.6. After injection ($N = 0$), the values of λ are large, indicating that the particle pairs initially close together near IW become separated to various positions within the area of interest. As the RPM flow protocol proceeds, the

Lyapunov exponents fluctuate non-linearly to a final value of ~0.12 which is consistent with the estimates of 0.12 and 0.15 for λ determined by Lester et al. (2013) and Trefry et al. (2018), respectively. Furthermore, the Lyapunov exponents are positive for the entire duration, indicating the presence of chaos (Jones and Aref, 1988; Dentz et al., 2017). Both the Poincaré section and Lyapunov exponents demonstrate features that are consistent with the theoretical behavior, which strongly suggest the presence of chaotic advection in this system.

The simulated BTCs demonstrate an oscillatory behavior that has been identified to be consistent with an RPM flow system. The topology and behavior of the reagent distribution, as determined by the contours of the simulated concentrations, illustrate strong similarities to those observed from a laboratory-scale experiment of chaotic advection, as well as the Poincaré section. The Poincaré section and the Lyapunov exponents determined by analyzing the particle tracking simulation results show characteristics that are consistent with the theoretical behavior in the presence of chaotic advection. Collectively, these findings indicate that this modeling approach can reproduce the key features of the expected behavior reported in other studies of chaotic advection over a range of scales (e.g., theory, laboratory and field). These results provide confidence that this modeling approach is able to capture the transport behavior of a conservative reagent in the presence of chaotic advection generated by an RPM flow system.

4.3.2 Impact of RPM Flow Parameters on Mixing Behavior

To provide insight into the role specific RPM flow parameters have on the mixing behavior of a conservative reagent, additional scenarios were explored (Table 4.1). Figure 4.7 illustrates the reagent distribution after 12 complete cycles of RPM flow ($N = 12$) for Scenarios S1 to S6, as represented by the contours of the simulated concentrations (see Figures E-3 to E-9 for snapshots of the reagent distribution at select times).

In all scenarios except S5 and S6, the simulated reagent distributions show a skew towards the first few extraction wells of the RPM flow sequence (Table 4.3), as observed in the baseline scenario. This skew at early RPM flow cycles leads to a reagent distribution that is asymmetric at the end of the simulation period ($N = 12$). While reagent spreading is visually observed in the reagent distributions produced for Scenario S1, S2, S3, S4 and S6, each set of RPM flow parameters yields different shapes and patterns. For instance, the reagent distribution produced by the four wells in Scenario S1 (IE-1, IE-3, IE-5 and IE-7 with $\Theta = 90°$) shows a diamond shape with four "tails" that become increasingly stretched out toward the IE wells as mixing progresses. In contrast, the reagent distribution in Scenario S2 is irregular in shape based on the reorientation angle of 135° used, and shows the largest outer region (green) across all the scenarios explored. The reagent distribution for Scenario S3 is similar to that of the baseline scenario, with eight "tails" corresponding to each IE well and a skew in the direction of the first three extraction wells in the RPM flow sequence, as expected; however, the shorter t_p used in Scenario S3 yields a reagent distribution that is more circular in shape, and less stretched out diagonally than the baseline scenario. The sequence of t_p used in Scenario S4 (Table 4.2) produces an irregular reagent distribution that becomes more diagonally elongated over time until by $N = 12$, the reagent mass is captured at the extraction well (denoted by E on Figure 4.7).

In Scenario S6-A, heterogeneities in the *K* field lead to significant deviations from the smooth, circular plume observed in the homogeneous aquifer immediately after injection (see $N = 0$ on Figure E-7). As the number of RPM flow cycles increase, the reagent distribution in Scenario S6-A shows highly irregular structures that are stretched out into thin filaments (Figure 4.7). These irregular structures are a product of the velocity variations due to the heterogeneous *K* field and the complex chaotic flow fields generated by the RPM flow system. At early times ($N = 0$ to $N = 2$ on Figure E-7), the reagent distribution follows the areas of higher *K,* and bypasses the pockets of lower *K* evident in the *K* field (Figure E-2) to produce a long and narrow plume that is stretched along the *x*-axis. As RPM flow continues, the reagent distribution becomes more rotated, and is eventually able to overcome these preferential flow paths to move into the lower *K* regions ($N = 5$ and $N = 12$ on Figure E-7). Furthermore, the central red region initially present after injection is no longer observed (Figure 4.7). The reagent distribution from Scenario S6-B also shows the formation of highly irregular structures; however, the reagent distribution in Scenario S6-B is more broad in shape, with an even spreading around IW than the narrow plume observed in Scenario S6-A. The initial red region near IW is pulled into jagged, thin filaments, until it becomes no longer visible after 12 cycles of RPM flow (see Figure E-9). Differences are observed in the overall shape of the reagent distribution, corresponding to the variability in the *K* field between Scenarios S6-A and S6-B. The correlation length of 0.1 m (in both the *x*- and *y*-directions) used in Scenario S6-B generates a *K* field comprised of many small-scale lower *K* zones embedded within the overall *K* distribution, whereas Scenario S6-A shows relatively large, distinguishable lower *K* pockets/patches corresponding to a correlation length of 0.5 m.

Furthermore, Scenarios S6-A and S6-B which use the same RPM flow parameters as Scenario S2 both yield reagent distributions that are distinctly different from those produced by Scenario S2, further highlighting the impact of the *K* field on the reagent transport behavior.

In contrast to the results from the five scenarios discussed above, the reagent distribution produced by Scenario S5 illustrates minimal change in shape within the area of interest over the simulation duration. At $N = 12$, the reagent distribution resembles the circle initially observed after injection (Figures 4.7 and E-6); however, the central red region initially present at the end of injection is visibly reduced in size, and surrounded by an outer green region indicative of lower reagent concentrations. The reagent distribution produced by Scenario S5 suggests that the RPM flow protocol confines the reagent mass in the vicinity of IW, and that mixing occurs inside this confined mass. It is expected that with additional number of RPM flow cycles (i.e., $N > 12$), the reagent distribution would eventually become well-mixed, as indicated by a green to cyan circle in the area of interest.

After 12 cycles of RPM flow, the center of the reagent mass ($\bar{x}_c$, $\bar{y}_c$) for the baseline scenario, as estimated from the first spatial moment, had moved 14 cm in the *x*-direction and 9 cm in the *y*-direction. In Scenarios S1, S2, S4 and S6 the center of the reagent mass show displacements ranging from -20 to 11 cm, and 3 to 30 cm in the *x*- and *y*- directions, respectively. This displacement, in both the *x*- and *y*- directions, is a result of the skew towards the first few extraction wells of the RPM flow sequence (Table 4.3) that lead to asymmetry in the reagent distributions, as discussed above (Figures 4.2 and E-3 to E-9). The magnitude of the displacements suggests significant movement and spreading of the reagent mass in Scenarios S1, S2, S4 and S6. In contrast, the center of reagent mass in Scenarios S3 and S5 show a displacement of 1 cm and 0 cm in both the *x*- and *y*- directions, respectively, indicating that the tracer distribution remained near IW at the end of the simulation.

The visual observations from the reagent distributions and the displacements of the center of mass across the scenarios are supported by the second spatial moments (s_x^2, s_y^2) which describe the degree of spreading around the centroid (Figure 4.8). For mixing scenarios explored (S1 to S4 and S6), the second spatial moment in the *x*- and *y*- directions increase non-linearly to normalized values of >1 after 12 cycles of RPM flow. For illustration, a typical result showing the temporal changes in the normalized second spatial moments for the baseline scenario is provided in Figure 4.8(a) (see Figure E-10 for all the other scenarios). The increase in the second spatial moments suggest that the RPM flow parameters used in all scenarios lead to enhanced lateral spreading of the reagent. Comparing the second spatial moments from Scenarios S1 to S6 to those from the baseline scenario after 12 cycles of RPM flow (s_x^2 = 1.46, and s_y^2 = 1.68, as indicated by the dashed lines on inset of Figure 4.8(b)), Scenario S2 using eight IE wells with Θ = 135° shows the most significant lateral spreading of the reagent in the homogeneous aquifer with normalized values of 1.93 and 1.72 in the *x*- and *y*- directions, respectively. The second spatial moments produced by the sequence of t_p in Scenario S4 indicate a greater degree of reagent spreading in *y*-direction (s_y^2 = 1.80) than both the baseline scenario and Scenario S2; however, spreading in the *x*-direction is not as significant (s_x^2 = 1.45). This skew in the *y*-direction is a result of the diagonally elongated reagent distribution observed in the spatial distribution of simulated concentrations (Figure 4.7). Using the minimum number of IE wells required for chaotic advection (four IE wells with Θ = 90°), Scenario S1 shows a similar range of second spatial moments as the baseline scenario, with normalized values of 1.50 and 1.62 in the *x*- and *y*- directions, respectively. Conversely, Scenario S3 which uses the same RPM flow parameters as the baseline scenario but with t_p = 2 hours, produces lower values of the normalized second spatial moments (s_x^2 = 1.42, and s_y^2 = 1.58) than the baseline scenario, suggesting that less reagent spreading is achieved with a shorter pumping duration. Scenario S5 yields the lowest second spatial moments with final normalized values of 1.24 and 1.32 in the *x*- and *y*- directions, respectively, which indicates minimal lateral spreading and confirms that the reagent mass remains confined within the network of IE wells. As expected, the degree of spreading was significantly greater for Scenarios S6-A and S6-B in comparison to the other scenarios because of the heterogeneous *K* fields used. For Scenario S6-A the final normalized s_x^2 and s_y^2 values are 4.17 and 4.67, while for Scenario S6-B the final normalized s_x^2 and s_y^2 values are 5.41 and 3.72.

Since spreading provides a description of the spatial extent of the reagent distribution using average concentrations rather than its distribution within the plume (Dentz et al., 2017), concentration variance (s_C^2) was used to indicate the degree of mixing in this system (Kitanidis, 1994; Kapoor and Kitanidis, 1998; Dentz et al., 2011; Le Borgne et al., 2011) based on the potential for chaotic advection to enhance both spreading and mixing. Normalized values of s_C^2 for all scenarios begin at unity and decrease non-linearly (Figure 4.9). This suggests that the RPM flow system promotes enhanced reagent mixing to produce a similar range of concentrations within the network of IE wells. This interpretation is consistent with the behavior expected from a well-mixed system which would produce a s_C^2 value of zero with uniform concentrations across the area of interest (Sposito, 1998). The various combinations of RPM flow parameters explored in the scenarios produce a range in the degree of mixing. For example, Scenario S2 which showed the greatest degree of lateral spreading in the homogeneous *K* field as indicated by the second spatial moments also produces the greatest decrease in s_C^2 and thus, enhanced mixing, with a final value of 0.35 after 12 cycles of RPM flow. A similar trend was observed in Scenario S4 with a final s_C^2 value of 0.38. The overall degree of mixing observed in Scenarios S2 and S4 is comparable to the baseline scenario (s_C^2 = 0.33) which is expected given the similar spreading behavior of the reagent for these three sets of RPM flow parameters. The concentration variance produced by Scenarios S1 and S3 both demonstrate moderate mixing with s_C^2 values of 0.52 and 0.55, respectively. The final s_C^2 value of 0.06 produced by Scenarios S6-A and S6-B demonstrate that mixing is significantly enhanced in the presence of *K* heterogeneities. While Scenario S5 demonstrates the lowest degree of mixing with a s_C^2 value of 0.70 after 12 cycles of RPM flow, it is important to distinguish this confinement scenario from the Scenarios S1 to S4, and S6, which were designed to enhance reagent mixing. The decrease in s_C^2 values produced by Scenario S5 suggests that some mixing occurs within the confined reagent mass which occurs primarily at the fringes of the plume. It is expected that a greater degree of mixing can be achieved within the confined reagent plume with additional number of RPM flow cycles (i.e., $N > 12$).

Furthermore, the normalized concentration variance determined from the reagent concentrations are inversely proportional to the theoretical mixing parameter, *q*, reported by Lester et al. (2010), but within a range that is expected for the degree of mixing observed. For example, s_C^2 values of 0.70 and 0.33 after 12 cycles of RPM flow correspond to *q* of ~1.4 and ~2.1 for Scenario S5 and the baseline scenario, respectively. For the scenarios that show moderate mixing (i.e., Scenarios S1 and S3 with s_C^2 value of ~0.5 after 12 cycles of RPM flow), *q* is estimated to be ~1.8. This is expected since q describes how much mixing is theoretically possible for a specific time duration (as a ratio of the mixing rate associated with an RPM flow with that of a purely dispersive system under steady flow), while s_C^2 is a measure of the variability across the concentration field within the area of interest. In other words, for higher estimates of q, we would expect lower s_C^2 values in a shorter period of time, leading to uniform reagent concentrations to be established within the network of IE wells. In the confinement scenario, mixing is expected to occur within the confined reagent mass which eventually leads to uniform concentrations, but over a longer duration (i.e., lower q). While a relationship between s_C^2 and q is not investigated, this empirical comparison indicates that this theoretical parameter reported by Lester et al. (2010) provides a basis for the initial estimate of the RPM flow parameters to achieve the desired degree of mixing.

The visual observations from the spatial distribution of the reagent concentration, combined with the results from the second spatial moments and concentration variance highlight the range of responses and behavior possible by the combinations of RPM flow parameters explored. As expected, the selection of RPM flow parameters governs reagent mixing behavior. Collectively, these simulations results have important implications for the design of an RPM flow system. Key findings are:

- The simulation results support the theoretical work reported in other studies regarding the generation of chaotic advection using an RPM flow system. For example, the time-dependent flow field produced by the RPM flow system led to the generation of chaotic advection in all scenarios, and produced either zones of enhanced mixing and/or confinement. More specifically, the observations from Scenario S1 confirm that it is possible to invoke chaotic advection and promote enhanced mixing using a minimum of two dipoles (Lester et al., 2010). Furthermore, the results from Scenario S5 demonstrate the potential of an RPM flow system with a lower Q and t_p to produce reagent confinement (Trefry et al., 2012).

- The use of the same RPM flow protocol in a heterogeneous K field led to significantly greater degree of reagent spreading and mixing than in a homogeneous K setting. This observation is consistent with the theoretical work of Trefry et al. (2012), Neupauer et al. (2014) and Rodriguez-Escales et al. (2017) that demonstrated solute mixing and spreading by chaotic advection is significantly enhanced when K heterogeneities are considered.

- The reagent distributions and the quantitative metrics indicate that the degree of spreading and mixing is not necessarily the same. For example, Scenario S1 yields a similar degree of spreading as the baseline scenario, but not as much mixing. Conversely, Scenario S2 shows significant lateral spreading in comparison to the baseline scenario especially in the y-direction, but the overall degree of mixing achieved by both scenarios is similar. This observation highlights the important distinction between spreading and mixing which must be considered in the design of an effective RPM flow system to achieve the desired outcomes.
- While the RPM flow protocol in the baseline scenario, and Scenarios S2 and S3 involved the use of all eight IE wells, variable spreading and mixing behavior is observed across these three scenarios. For example, the results from Scenario S2 show a greater degree of spreading than from the baseline scenario because of the different re-orientation angle used. In contrast, Scenario S1 (four IE wells) and Scenario S3 (eight IE wells) produced a similar range of the second spatial moments and concentration variance. These observations suggest that having more IE wells in the RPM flow protocol is not a requirement for a greater degree of reagent spreading and mixing. Instead, the overall degree of reagent spreading and mixing relies on a specific combination of the RPM flow parameters, which can be determined, in part, from theoretical considerations (i.e., q) to achieve the desired outcomes.
- As expected, a decrease in the flow rate, Q and/or the pumping duration, t_p in Scenarios S3 and S5 led to reduced reagent spreading and mixing. This observation indicates that both the flow rate and pumping duration are key parameters of an RPM flow system that have direct consequences on the degree of reagent spreading and mixing. While an increase in Q and t_p may theoretically contribute to a greater degree of mixing, practical design limitations must also be considered (discussed below).
- While theoretical considerations provide an initial estimate to achieve enhanced spreading and mixing practical design limitations related to the pumping duration and flow rate are also important. For example, while Scenario S4 achieves significant

reagent spreading and mixing based on the quantitative metrics alone, the reagent distribution, as represented by the contours of the simulated concentrations, indicate that the reagent mass is captured at the extraction wells. This observation highlights the importance of combining theoretical considerations with practical limitations when designing an RPM flow system in order to promote enhanced spreading and mixing, while minimizing the reagent mass captured by the IE wells.

4.4 CLOSURE

The results from this investigation demonstrated that a conventional transport modeling method (i.e., Method of Characteristics in MT3DMS coupled with MODFLOW) can represent chaotic flow and transport behavior associated with an RPM flow system. The simulated BTCs showed an oscillatory behavior that was identified to be consistent with an RPM flow system. A Fourier transform of the simulated breakthrough concentrations also revealed a continuous spectrum of frequencies composed of many smaller peaks that is consistent with the expected behavior of a chaotic signal. The corresponding Poincaré section and the Lyapunov exponents determined by analyzing the particle tracking results showed characteristics of the expected behavior in the presence of chaotic advection. Collectively, these results strongly suggest that this modeling approach is able to capture the key features of the chaotic flow and transport behavior expected in an RPM flow system.

Using this transport model, various scenarios were then explored to improve our understanding of the impact of specific RPM flow parameters on the mixing behavior of a conservative reagent. Visual observations of the reagent distribution produced by this transport model, and the quantitative metrics of mixing behavior (i.e., second spatial moments and concentration variance) highlighted the different responses that are possible by various combinations of RPM flow parameters within the area of interest. For example, the results demonstrated that it is possible to promote enhanced reagent mixing by chaotic advection using the minimum of two dipoles. Both the flow rate and pumping duration were identified as key parameters of an RPM flow system that have direct consequences on the degree of reagent mixing. Furthermore, the use of the same RPM flow protocol in a heterogeneous *K* field led to significantly greater degree of reagent mixing than in a homogeneous *K* setting. The scenarios also highlighted the importance of combining theoretical considerations with practical limitations when designing an RPM flow system that can both enhance reagent mixing and minimize the mass captured at the IE wells.

The findings provided insights into the engineering controls of an effective RPM flow system that can achieve the desired outcomes. While the modeling results presented in this study makes significant advancement in our growing understanding of chaotic advection in porous media, ongoing efforts are needed to incorporate a *K* field specific to the target treatment zone in a 3D model for improved representation of the flow and transport behavior of a conservative reagent, which can be used in conjunction with field-scale implementation of an RPM flow system.

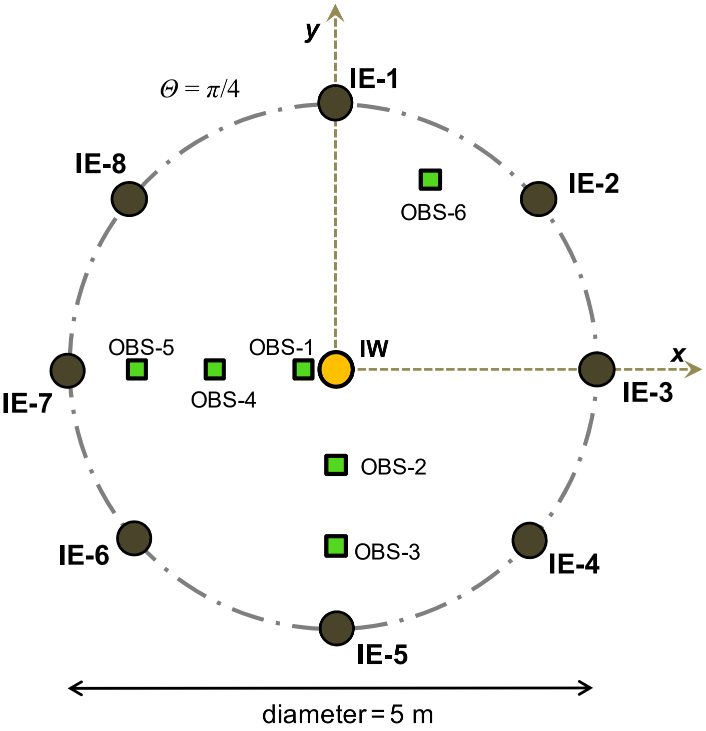

Figure 4.1. Plan view of the circular system of injection/extraction wells (IE-1 to IE-8), central reagent injection well (IW), and location of six hypothetical observation wells (OBS).

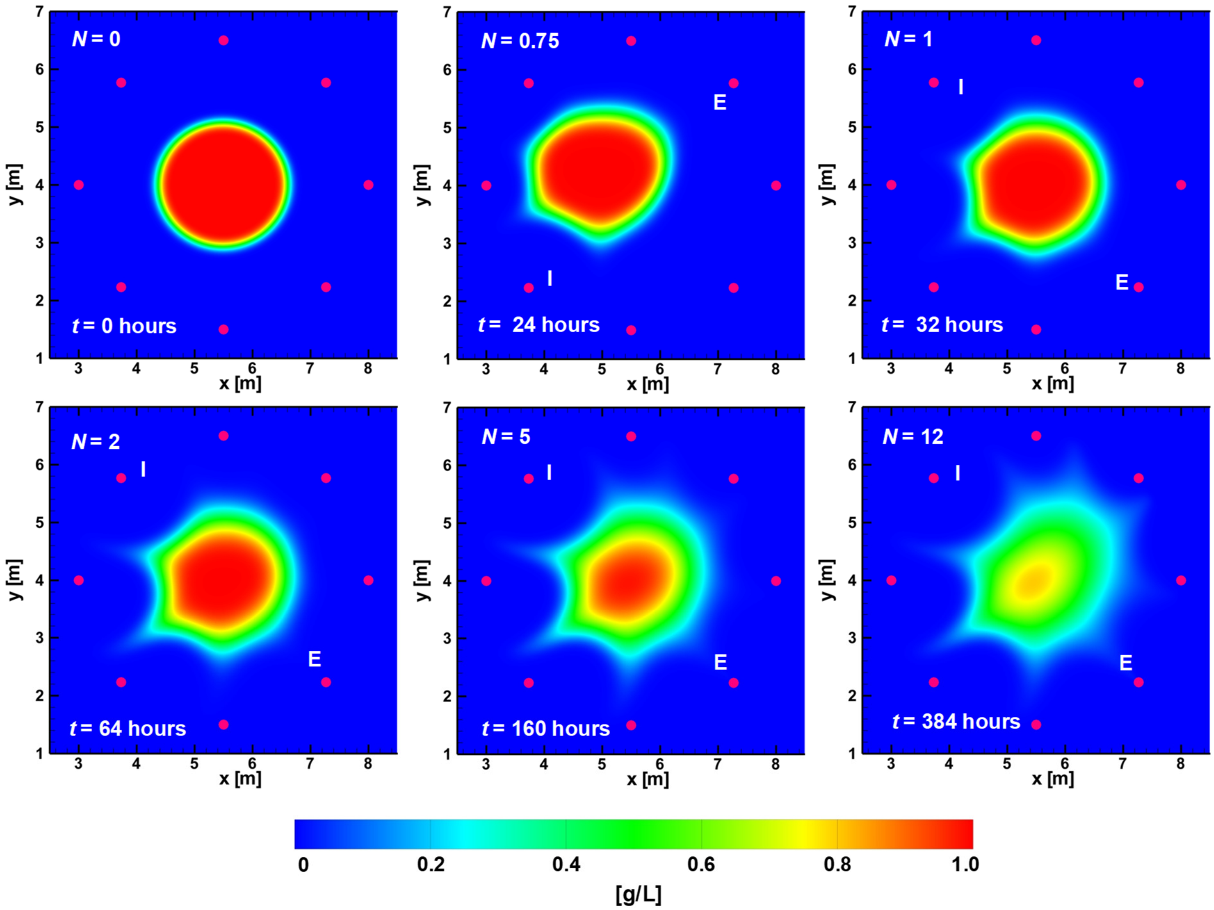

Figure 4.2. Contours of simulated reagent concentrations for the baseline scenario during RPM flow ($\Theta = 45°$, $Q_{RPM} = 5$ m^3/d, $t_p = 4$ hours, $D = 5$ m, and $N = 12$) at select times, t. The pink solid circles indicate IE well locations used for the RPM flow system, with "I" and "E" on each panel denoting the location of the active injection and extraction well at the select time, respectively, and N is the number of complete RPM flow cycles.

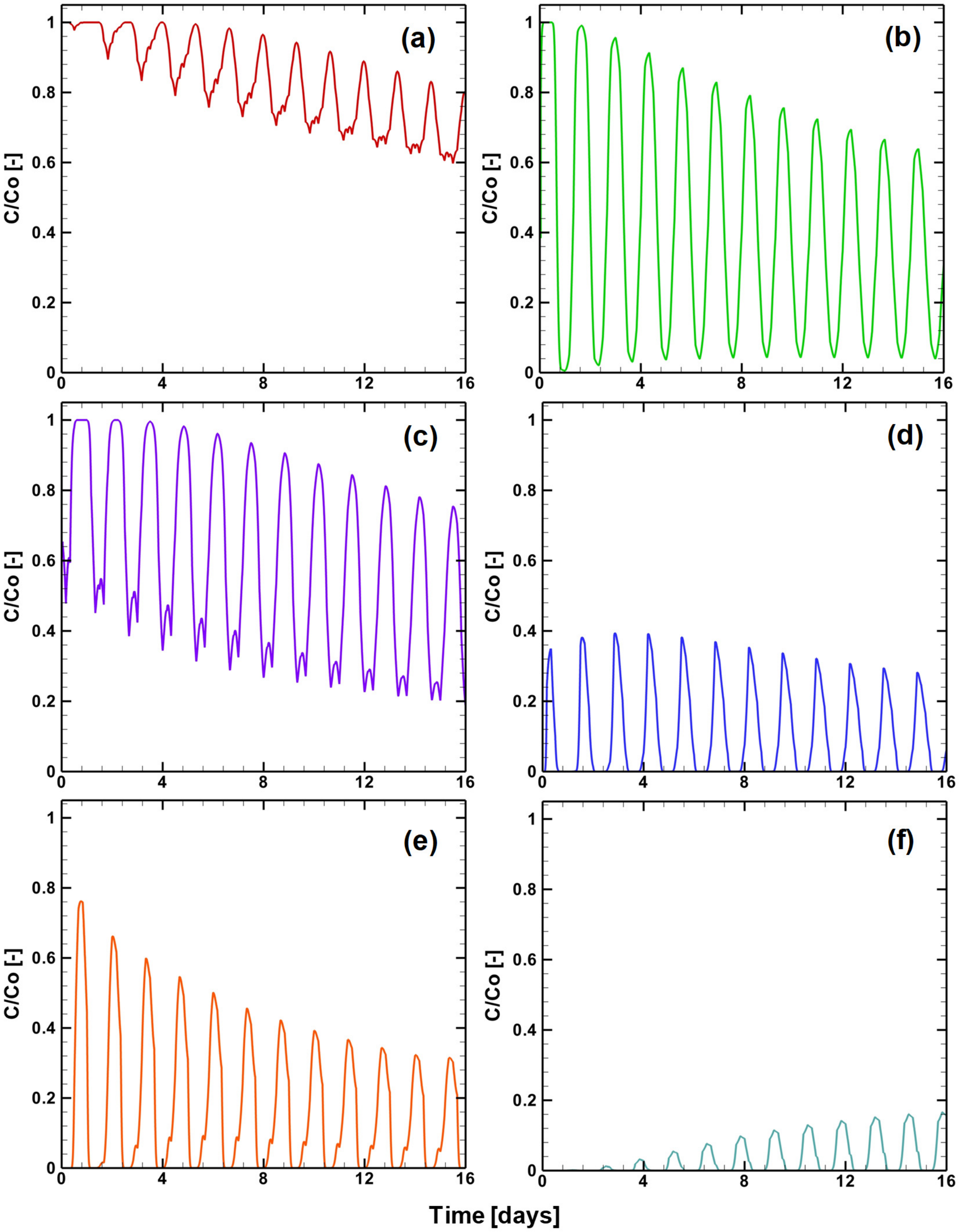

Figure 4.3. Reagent breakthrough curves during RPM flow ($\Theta = 45°$, $Q_{RPM} = 5$ m^3/d, $t_p = 4$ hours and $D = 5$ m) at observation well: (a) OBS-1, (b) OBS-2, (c) OBS-3, (d) OBS-4, (e), OBS-5, and (f) OBS-6.

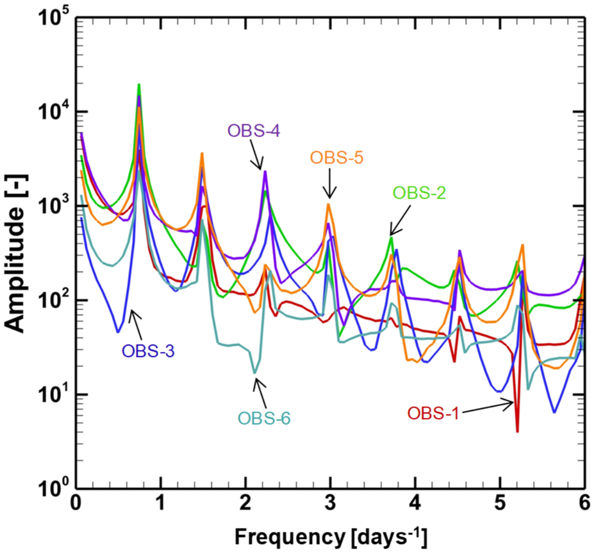

Figure 4.4. Frequency spectrum of the Fourier transform of the simulated breakthrough data at all hypothetical observation wells (OBS-1 to OBS-6).

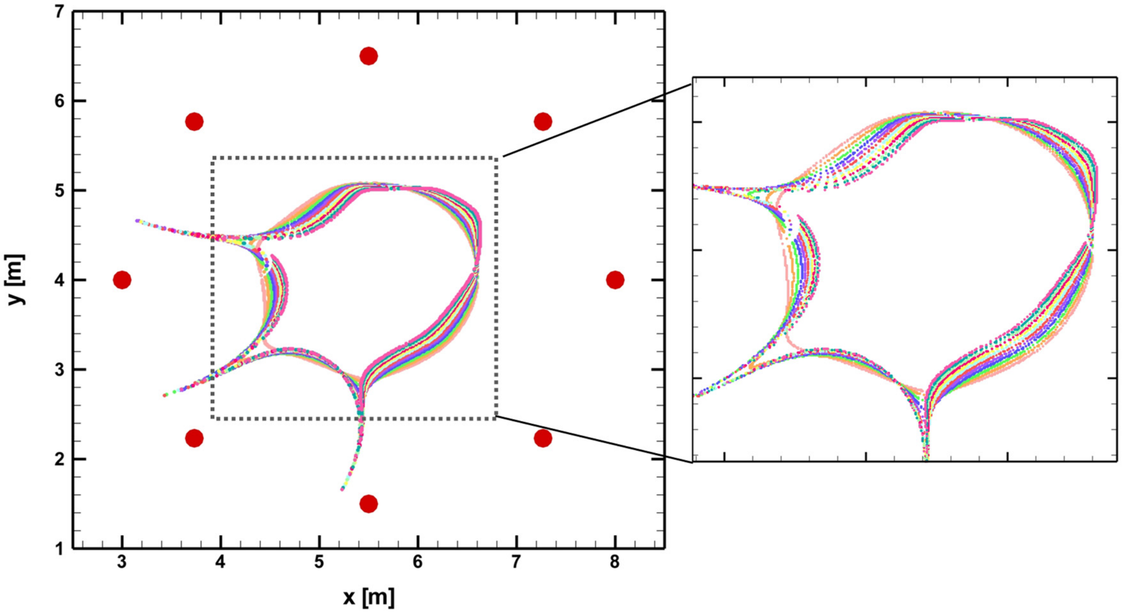

Figure 4.5. Poincaré section showing particle positions after each iteration of RPM flow for the baseline scenario ($\Theta = 45°$, $t_p = 4$ hours and $Q_{RPM} = 5$ m^3/d), superimposed for 12 RPM flow periods. The red solid circles indicate IE well locations used for the RPM flow system, and each color used for the particle positions represents an iteration of RPM flow. Inset represents a close-up view at the boundaries of the Poincaré section.

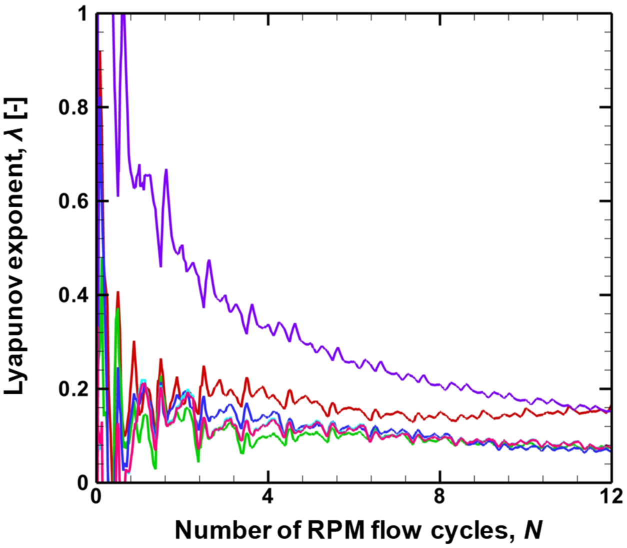

Figure 4.6. Lyapunov exponents (λ) for 6 particle pairs arbitrarily chosen for illustration with an initial separation distance ≤ 0.02 m. Solid lines indicate values of λ for the different particle pairs, and the dashed line represents the ensemble mean (determined as an average between 50 particle pairs).

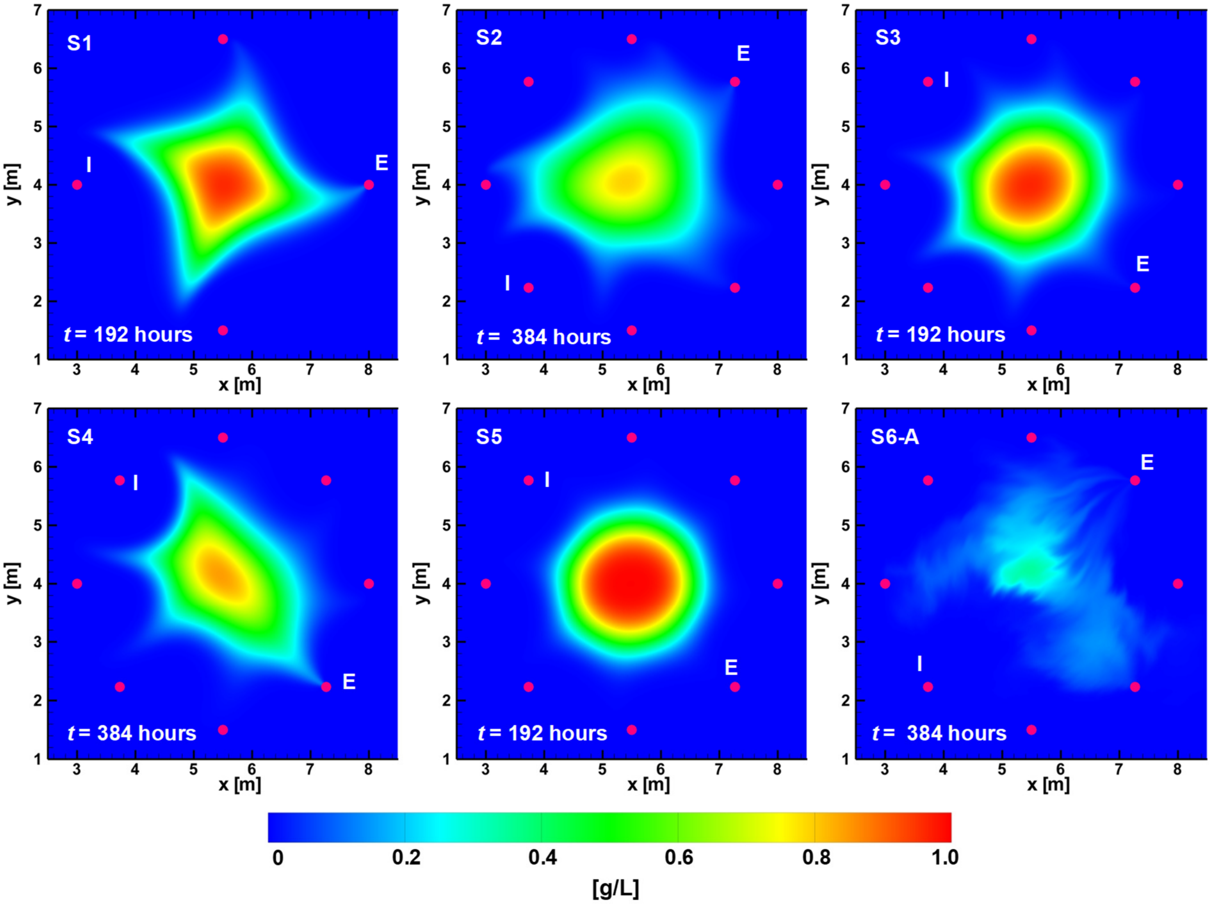

Figure 4.7. Contours of simulated reagent concentrations for Scenarios S1 to S6-A at $N = 12$. The pink solid circles indicate IE well locations used for the RPM flow system, with "I" and "E" on each panel denoting the location of the active injection and extraction well at the select time, respectively (See Figure E-9 for Scenario S6-B).

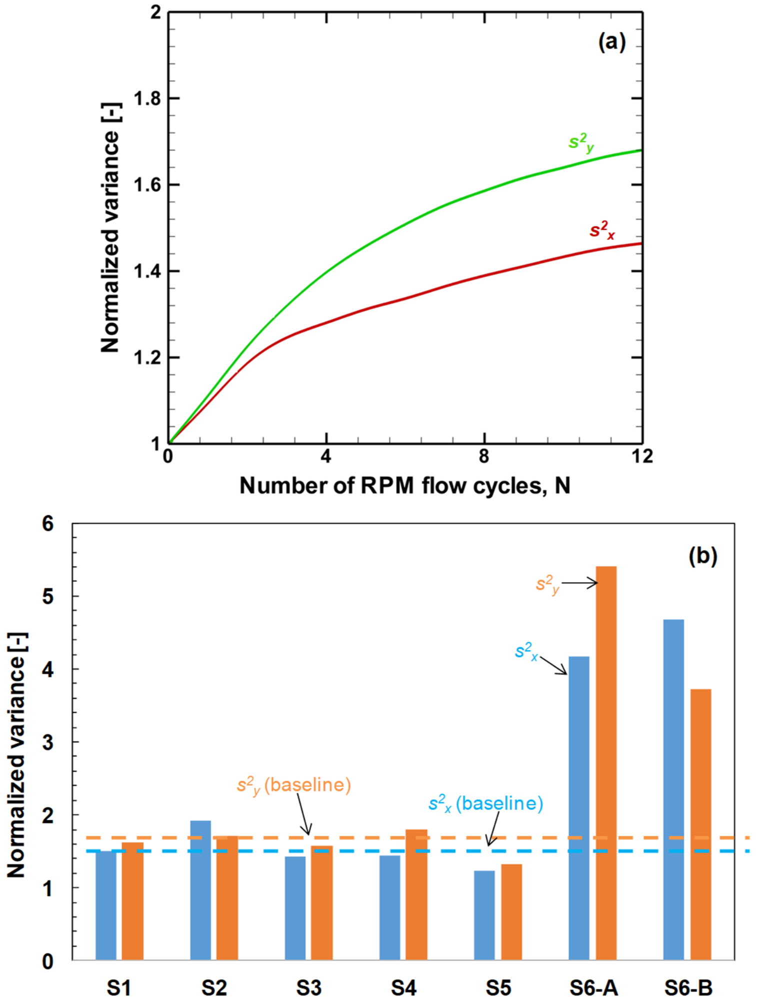

Figure 4.8. (a) Temporal profile of normalized spatial variance (s_x^2, s_y^2) for the baseline scenario, and (b) a comparison of the normalized spatial variance for Scenarios S1 to S6 after N = 12 of RPM flow. Variances were normalized to values estimated from the reagent spatial distribution immediately after injection.

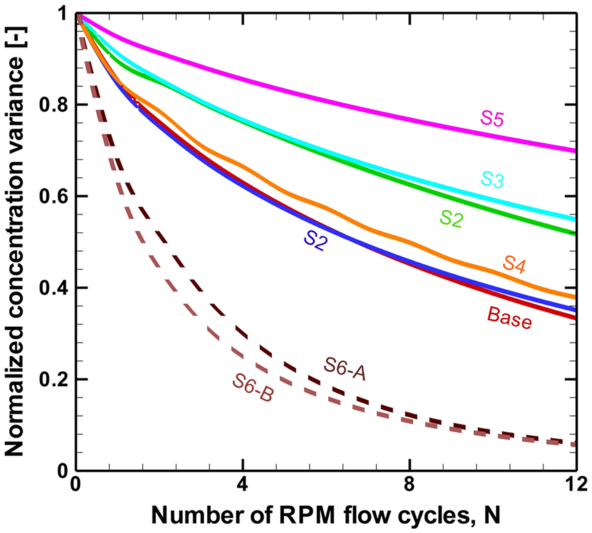

Figure 4.9. Temporal profile of normalized concentration variance (s_C^2) for the various scenarios (baseline, and S1 to S6) over the area of interest (i.e., the limits of eight injection/extraction wells). Variances were normalized to the initial variance immediately after reagent injection.

Table 4.1. Summary of RPM flow parameters used in the various scenarios.

Parameters	**Scenario ID**						
	Baseline	**S1**	**S2**	**S3**	**S4**[a]	**S5**	**S6**[b]
Number of wells	8	4	8	8	8	8	8
Re-orientation angle, Θ (degrees)	45	90	135	45	45	45	135
Pumping rate, Q_{RPM} (m^3/d)	5	5	5	5	5	2.5	5
Pumping duration, t_p (hours)	4	4	4	2	4[a]	2	4
Total duration, t_{RPM} (hours)	384	192	384	192	384	192	384

[a] Simulations performed using the same parameters as the baseline, but select IE well pairs were set to switch on and off between each iteration of the RPM flow period, see Table 4.2.

[b] Same RPM flow parameters as Scenario S2, but with a mildly heterogeneous K field assigned to the model domain

Table 4.2. The t_p sequence used in Scenario S5 during each cycle of RPM flow.

RPM flow cycle, *N*	**Active IE Well Pairs**							
	IE-1(I) IE-5(E)	IE-2(I) IE-6(E)	IE-3(I) IE-7(E)	IE-4(I) IE-8(E)	IE-5(I) IE-1(E)	IE-6(I) IE-2(E)	IE-7(I) IE-3(E)	IE-8(I) IE-4(E)
1	o	o	o	o	o	o	o	o
2	x	o	o	o	o	o	o	o
3	o	o	o	o	o	o	o	o
4	x	o	o	o	o	o	o	o
5	o	o	o	o	o	o	o	o
6	x	o	o	o	o	o	o	o
7	o	o	o	o	o	o	o	o
8	x	o	o	o	o	o	o	o
9	o	o	o	o	o	o	o	o
10	x	o	o	o	o	o	o	o
11	o	o	o	o	o	o	o	o
12	x	o	o	o	o	o	o	o

Note: The “o” symbol denotes when the IE well pair was operational and the “x” symbol denotes when the IE well pair was turned off.

Table 4.3. Sequence of the active IE well pairs during each cycle of RPM flow.

Scenario ID	**Active IE Well Pairs**							
	IE-1(I) IE-5(E)	IE-2(I) IE-6(E)	IE-3(I) IE-7(E)	IE-4(I) IE-8(E)	IE-5(I) IE-1(E)	IE-6(I) IE-2(E)	IE-7(I) IE-3(E)	IE-8(I) IE-4(E)
Baseline	1	2	3	4	5	6	7	8
S1	1	x[a]	2	x	3	x	4	x
S2	1	4	7	2	5	8	3	6
S3	1	2	3	4	5	6	7	8
S4[b]	1	2	3	4	5	6	7	8
S5	1	2	3	4	5	6	7	8
S6[c]	1	4	7	2	5	8	3	6

Notes:

[a] The "x" symbol denotes when the IE well pair was turned off.

[b] Simulations performed using the same parameters as the baseline, but select IE well pairs were set to switch on and off between each iteration of the RPM flow period, see Table 4.2.

[c] Same RPM flow parameters as Scenario S2, but with a mildly heterogeneous *K* field assigned to the model domain

Chapter 5

Closure

5.1 CONTRIBUTIONS AND CONCLUSIONS

The primary goal of this research was to investigate if chaotic advection can be invoked using an RPM flow protocol in a natural aquifer system. The field investigations were supported by a suite of quantitative metrics and modeling tools that can aid the design and interpretation process. A series of solute tracer experiments were conducted using an RPM flow system in a natural aquifer, and various quantitative metrics were subsequently used to evaluate the presence of chaotic advection and its impact on tracer mixing. Hydraulic observations collected from the same well system used to invoke chaotic advection were applied in a steady-state hydraulic tomography (SSHT) analysis to provide information about the *K* field. The consequence of using this *K* tomogram (i.e., image of the *K* field) on the spatial distribution of a hypothetical reagent in a target treatment zone was then investigated. Transport simulations were performed to explore the role that specific RPM flow parameters have on the reagent mixing behavior and to identify implications for the design of an effective RPM flow system.

The significant contributions from this research are summarized below:

- The suite of quantitative metrics and numerical modeling efforts provide various tools for the design of an RPM flow system and subsequent data interpretation. The combination of experimental and supportive modeling efforts provides insights into the design of an effective RPM flow system that can generate chaotic advection and promote enhanced reagent mixing in the subsurface. The lessons learned are useful for remediation engineers and scientists who intend to implement this system for improved effectiveness during *in situ* treatment.
- The proof-of-concept study (Chapter 2) is the first field-scale investigation to extend on the established theoretical underpinnings and observations from bench-scale experiments of chaotic advection, and to provide comprehensive information about chaotic advection as an approach to enhance reagent mixing in a natural aquifer system.

- A suite of quantitative metrics were developed to demonstrate the presence of chaotic advection and its impacts on tracer mixing based on the spatial and temporal resolution of field data. These metrics include: integrated volume under the three-dimensional contours of tracer concentration data, variance of tracer concentrations, spatial concentration gradients, and the first two spatial moments of the tracer concentration distribution.
- A unique approach was presented to support RPM design which involved the use of the same well system required to invoke chaotic advection in a 3D SSHT analysis to delineate the spatial variability of the *K* field (Chapter 3). Using *K* information applicable to a specific target treatment zone has significant implications for the development of a model that can adequately represent the groundwater flow within an aquifer undergoing periodically re-oriented dipole pumping. This groundwater flow model is an important design tool for the determination of an RPM flow protocol that can achieve the desired outcomes.
- The numerical study described in Chapter 4 is the first effort to use a conventional modeling method (Method of Characteristics in MT3DMS) to simulate the transport behavior of a conservative reagent specifically for an RPM flow system. This transport model is significant because it can provide a platform to explore the impacts that specific engineering controls of an RPM flow system have on the reagent mixing behavior. This transport model is a critical supportive tool for field implementation of chaotic advection that can be used to design an effective RPM flow system for enhanced reagent mixing.

The above contributions are based on the following conclusions emerging from this research effort:

- The multiple lines of evidence assembled in the field-scale investigations suggested that chaotic advection can be engineered in a natural porous medium using a series of eight injection/extraction wells and a dipole pumping system designed to perform a RPM flow protocol. Comparison to observations from a previous laboratory experiment using RPM flow, and the Fourier spectrum of the temporal tracer data suggested the presence of chaos. Results from the various quantitative metrics indicated that RPM flow produced lateral spreading and enhanced mixing which led to uniform concentrations across the monitoring network. These findings demonstrated that chaotic advection is a viable and efficient alternative for reagent delivery in injection-driven *in situ* treatment systems.

- The *K* tomogram determined from the inversion of hydraulic observations collected from the same well system required to achieve chaotic advection produced estimates of steady-state and transient hydraulic heads that showed good correlation to those observed in the target treatment zone. This result demonstrated that the well system used to invoke chaotic advection can be applied in a hydraulic tomography (HT) analysis, providing a viable site characterization tool to delineate the spatial variability of *K* in the area of interest.
- Using the *K* tomogram in a 3D groundwater flow model (MODFLOW) coupled with a particle tracking engine (MODPATH) significantly enhanced the spatial distribution of particle trajectories within the target treatment zone. The *K* tomogram generated more spatially and densely distributed particle trajectories indicative of enhanced reagent mixing than those produced by the effective parameter approach in which all particles showed minimal change from their initial positions for the entire simulation duration. The particle tracking results suggested that improved representation of the variability in the *K* field has important implications on the reagent mixing behavior.
- The transport simulation results indicated that the modeling approach (Method of Characteristics in MT3DMS) can reproduce the key features of the expected behavior of chaotic advection. The simulated breakthrough curves showed an oscillatory behavior at all observation locations that has been identified to be consistent with an RPM flow system. The transport simulation results were supported by the presence of chaotic advection using theoretical diagnostic methods based on the analysis of individual particle trajectories (e.g., Poincare section and Lyapunov exponent). The findings provided confidence to this modeling approach to be able to capture the transport behavior of a conservative reagent subjected to an RPM flow system.
- The reagent distributions, as represented by the contours of the simulated concentrations, and the various metrics adopted to demonstrate mixing behavior

highlighted the range of responses possible by the combinations of RPM flow parameters explored. The RPM flow protocol (e.g., re-orientation angle, flow rate and pumping duration) governed the transport behavior across all the scenarios investigated, which produced zones of enhanced mixing and/or confinement in the area of interest. Furthermore, a heterogeneous *K* field as the representation of the *K* distribution in the spatial domain generated significantly greater degree of reagent mixing than the homogeneous *K* setting. The findings provided important implications on the role that specific RPM flow parameters have on the reagent transport behavior, and considerations for the design of an effective RPM flow system.

5.2 RECOMMENDATIONS FOR FUTURE WORK

While significant contributions were achieved in this research, limitations associated with the RPM flow system were also identified. Since this proof-of-concept study was conducted in a relatively homogeneous system (Borden aquifer), the practical impact of *K* heterogeneities on the design of an RPM flow system, and ultimately, on the flow and mixing behaviour were not explored. As a result, all injection/extraction wells used in this study were installed in zones of similar *K* (within an order of magnitude); however, this is typically not the situation at most sites. Furthermore, it is expected that for larger target treatment areas, higher pumping rates or longer pumping durations will be needed to achieve enhanced mixing. In these situations, careful optimization of the RPM flow parameters will be required to enhance mixing while minimizing or preventing the extraction of reagent mass.

It is also important to recognize that despite efforts to characterize and incorporate a *K* field into a model domain, it will be challenging to develop a modeling tool that can be used to predict reagent transport and reaction within a given target treatment area. Enhanced mixing is driven by the exponential stretching and folding of the reagent plume; however, based on our current level of understanding and the monitoring tools available, it is likely impossible to specify within a model the conditions that would give rise to this chaotic behaviour at the field scale. Despite this concern, appropriate modeling efforts can be used to provide an indication of the degree of mixing that may be achieved in a target treatment area, albeit not in a predictive capacity.

In light of these limitations, the need for additional research efforts were raised during the course of this endeavor. The opportunities for further research are summarized in the following:

- For this pilot-scale study, the field tracer experiments of chaotic advection were conducted in a small area of a relatively homogeneous aquifer system. For deeper insight and improved robustness of the RPM flow system that can achieve chaotic advection and promote enhanced reagent mixing, additional field-scale investigations are recommended. These investigations should be completed in natural aquifer systems of higher K heterogeneity with a spatial scale that represents a larger target treatment zone (e.g., network of injection/extraction wells with a diameter up to ~5 m). The robustness of the supportive quantitative metrics should also be examined based on the data collected from the additional field investigations. The transport model presented in this study should be extended to incorporate the K field specific to this larger target treatment zone for the determination of an RPM flow protocol that can achieve the desired outcomes in this new aquifer setting.
- To estimate the K field in this new target treatment zone of a larger spatial scale and greater K heterogeneity as discussed above, a HT survey should be conducted. A series of dipole pumping tests should be performed in the new aquifer setting using the same well system which is applied to generate chaotic advection during the tracer experiments. The hydraulic observations collected from these dipole pumping tests should be used in a 3D SSHT and THT analyses to extend on the findings presented in this research effort. Additional investigations of HT present opportunities to test the robustness of the modeling tool presented in this research effort, particularly in consideration of the varying degrees of the K heterogeneities in the target treatment zone. The results from this HT analysis should be used to assess whether the larger spatial scale and greater K heterogeneity in the target treatment zone can generate a K tomogram that yields predictions of the hydraulic heads that are superior to those produced by the effective parameter approach.
- The primary focus of this research effort was to generate chaotic advection with enhanced mixing as the desired outcome; however, confinement is another possible consequence of the RPM flow system that may be beneficial in other *in situ* remedial applications. To expand our understanding of the range of potential applications for chaotic advection during *in situ* treatment, it is recommended that field tracer

experiments be performed for the design of an RPM flow system that can achieve a region of confinement.

- To examine whether enhanced mixing of a remedial reagent by an RPM flow system leads to improved treatment performance in a target treatment zone, a pilot-scale treatability study is recommended. Prior to implementation of the field-scale testing, the transport model should be used to determine an RPM flow protocol. In addition to the dipole pumping device and monitoring tools used in this study, the field-scale treatability tests will likely require novel methods for source zone characterization. The supportive quantitative methods presented in this research should also be extended to include metrics that can assess treatment performance (e.g., mass flux at a pre-determined monitoring locations based on dissolved phase concentrations and plume velocity estimates). The data collected from the field-scale treatability experiments should be used to refine the groundwater flow and transport model presented in this research.

References

Chapter 1

Aref, H. 1984. Stirring by chaotic advection. *Journal of Fluid Mechanics* 143: 1-21.

Aref, H., J.R. Blake, M. Budisic, S.S.S. Cardoso, J.H.E. Cartwright, H.J.H. Clercx, K. El Omari, … I. Tuval. 2017. Frontiers of chaotic advection. *Reviews of Modern Physics* 89, no. 2: 025007.

Bagtzoglou, A.C., and P.M Oates. 2007. Chaotic advection and enhanced groundwater remediation. *Journal of Materials in Civil Engineering* 19, no. 1: 75-83.

Conrad, S.H., J.L. Wilson, W.R. Mason and W.J. Peplinski. 1992. Visualization of residual organic liquid trapped in aquifers. *Water Resources Research* 28, no. 2: 467-478.

Dagan, G. 1986. Statistical theory of groundwater flow and transport: Pore to laboratory, laboratory to formation, and formation to regional scale. *Water Resources Research* 22, no. 9: 120-134.

Environment Canada. 2013. *Groundwater.* Retrieved September 2018, from: https://www.canada.ca/en/environment-climate-change/services/water-overview/sources/groundwater.html

Environment Canada. 2017. *Groundwater contamination.* Retrieved September 2018, from: https://www.canada.ca/en/environment-climate-change/services/water-overview/pollution-causes-effects/groundwater-contamination.html

Gale, T., N.R. Thomson, and J.F. Barker. 2015. An investigation of the pressure pulsing reagent delivery approach. *Groundwater Monitoring and Remediation* 35, no. 2: 39-51.

Jose, S.C., and O.A. Cirpka. 2004. Measurement of mixing-controlled reactive transport in homogeneous porous media and its prediction from conservative tracer test data. *Environmental Science and Technology* 38, no. 7: 2089-2096.

Kavanaugh, M. C., S.C. Rao, L. Abriola, J.A. Cherry, G. Destouni, R. Falta, et al. 2003. The DNAPL remediation challenge: Is there a case for source depletion? Ada, OK: National Risk Management Research Laboratory.

Kitanidis, P.K. 1994. The concept of the dilution index. *Water Resources Research* 30, no. 7: 2011-2026.

Kitanidis, P.K. and P.L. McCarty. 2012. *Delivery and mixing in the subsurface: Processes and design principles for in situ remediation*. New York, NY: Springer.

Lester, D.R., G. Metcalfe, M.G. Trefry, A. Ord, B. Hobbs, and M. Rudman. 2009. Lagrangian topology of a periodically reoriented potential flow: Symmetry, optimization, and mixing. *Physical Review E* 80, no. 3: 036208.

Liebeg, E.W., and T.J. Cutright. 1999. The investigation of enhanced bioremediation through the addition of macro and micro nutrients in a PAH contaminated soil. *International Biodeterioration and Biodegradation* 44: 55-64.

Lowe, K.S., F.G. Gardner, and R.L. Siegrist. 2002. Field evaluation of in situ chemical oxidation through vertical well-to-well recirculation of $NaMnO_4$. *Ground Water Monitoring and Remediation* 22, no. 1: 106-115.

Luo, J., W-M. Wu, J. Carley, C. Ruan, B. Gu, P.M. Jardine, C.S. Criddle, and P.K. Kitanidis. 2007. Hydraulic performance analysis of a multiple injection-extraction well system. *Journal of Hydrology* 336: 294-302.

Mays, D.C., and R.M. Neupauer. 2012. Plume spreading in groundwater by stretching and folding. *Water Resources Research* 48, no. 7: W07501.

Mercado, A., M. Libhaber, and M.I.M. Soares. 1988. In situ biological groundwater denitrification: Concepts and preliminary field tests. *Water Science and Technology* 20, no. 3: 197-209.

Metcalfe, G., D.R. Lester, M.G. Trefry, and A. Ord. 2008 Transport in a partially open porous media flow. In *Proceedings of SPIE: Complex systems II,* vol. 6802. Bellingham, WA.

Metcalfe, G., D.R. Lester, A. Ord, P. Kulkarni, M. Rudman, M.G. Trefry, . . . J. Morris. 2010a. An experimental and theoretical study of the mixing characteristics of a periodically reoriented irrotational flow. *Philosophical Transactions of the Royal Society A: Mathematical, Physical and Engineering Sciences* 368, no. 1918: 2147-2162.

Metcalfe, G., D.R. Lester, A. Ord, P. Kulkarni, M. Rudman, M.G. Trefry, . . . J. Morris. 2010b. A partially open porous media flow with chaotic advection: Towards a model of coupled fields. *Philosophical Transactions of the Royal Society A: Mathematical, Physical and Engineering Sciences* 368, no. 1918: 217-230.

Neupauer, R.M., J.D. Meiss, and D.C. Mays. 2014. Chaotic advection and reaction during engineered injection and extraction in heterogeneous porous media. *Water Resources Research* 50, no. 2: 1433-1447.

Nissan, A., I. Dror, and B. Berkowitz. 2017. Time-dependent velocity-field controls on anomalous chemical transport in porous media. *Water Resources Research* 53: 3760-3769.

Ottino, J.M. 1989. *The kinematics of mixing: Stretching, chaos and transport.* New York, NY: Cambridge University Press.

Ottino, J.M. 1990. Mixing, chaotic advection and turbulence. *Annual Review of Fluid Mechanics* 22: 207-253.

Parker, B.L., R.W. Gillham, and J.A. Cherry. 1994. Diffusive disappearance of immiscible-phase organic liquids in fractured geologic media. *Ground Water* 32, no. 5: 805–820.

Payne, F.C., J.A. Quinnan, and S.T. Potter. 2008. *Remediation hydraulics.* Boca Raton, FL: CRC Press.

Reinhard, M., S. Shang, P.K. Kitanidis, E. Orwin, G.D. Hopkins, and C.A. Lebron. 1997. In situ BTEX biotransformation under enhanced nitrate- and sulfate-reducing conditions. *Environmental Science and Technology* 31, no. 1: 28-36.

Rodriguez-Escales, P., D. Fernandez-Garcia, J. Drechsel, A. Folch, and X. Sanchez-Vila. 2017. Improving degradation of emerging organic compounds by applying chaotic advection in managed aquifer recharge in randomly heterogeneous porous media. *Water Resources Research* 53, no. 5: 4376-4392.

Saenton, S., T.H. Illangasekare, K. Soga, and T.A. Saba. 2002. Effects of source zone heterogeneity on surfactant-enhanced NAPL dissolution and resulting remediation end-points. *Journal of Contaminant Hydrology* 59: 27-44.

Siegrist, R.L, and T.J. Simpkin. 2016. *In situ* chemical oxidation for groundwater remediation. New York, NY: Springer.

Sposito, G. 2006. Chaotic solute advection by unsteady groundwater flows. *Water Resources Research* 42: W06D03.

Suthersan, S.S., and F.C. Payne. 2005. *In situ remediation engineering.* Boca Raton, FL: CRC Press.

Thomson, N.R., E.D. Hood, and G.J. Farquhar. 2007. Permanganate treatment of an emplaced DNAPL source. *Ground Water Monitoring and Remediation* 27, no. 4: 74-85.

Thomson, N.R, M.J. Fraser, C. Lamarche, J.F. Barker, and S.P. Forsey. 2008. Rebound of a coal tar creosote plume following partial source zone treatment with permanganate. *Journal of Contaminant Hydrology* 102: 154–171.

Trefry, M.G., D.R. Lester, G. Metcalfe, A. Ord, and K. Regenauer-Lieb. 2012. Toward enhanced subsurface intervention methods using chaotic advection. *Journal of Contaminant Hydrology* 127: 15-29.

USGS. 2018. Groundwater use in the United States. *The USGS Water Science School.* Retrieved September 2018, from: http://water.usgs.gov/edu/wugw.html

Zhang, P., S.L. Devries, A. Dathe, and A.C. Bagtzoglou. 2009. Enhanced mixing and plume containment in porous media under time-dependent oscillatory flow. *Environmental Science and Technology* 43, no. 16: 6283-6288.

Zhong, L., J. Szecsody, M. Oostrom, M. Truex, X. Shen, and X. Li. 2011. Enhanced remedial amendment delivery to subsurface using shear thinning fluid and aqueous foam. *Journal of Hazardous Materials* 191: 249-257.

Chapter 2

Aref, H. 1984. Stirring by chaotic advection. *Journal of Fluid Mechanics* 143: 1-21.

Aref, H., J.R. Blake, M. Budisic, S.S.S. Cardoso, J.H.E. Cartwright, H.J.H. Clercx, K. El Omari, … I. Tuval. 2017. Frontiers of chaotic advection. *Reviews of Modern Physics* 89, no. 2: 025007.

Bagtzoglou, A.C., and P.M Oates. 2007. Chaotic advection and enhanced groundwater remediation. *Journal of Materials in Civil Engineering* 19, no. 1: 75-83.

Conrad, S.H., J.L. Wilson, W.R. Mason and W.J. Peplinski. 1992. Visualization of residual organic liquid trapped in aquifers. *Water Resources Research* 28, no. 2: 467-478.

Cushman, J.H., and D.M. Tartakovsky. 2017. *Handbook of Groundwater Engineering*. Boca Raton, FL: CRC Press.

Dagan, G. 1986. Statistical theory of groundwater flow and transport: Pore to laboratory, laboratory to formation, and formation to regional scale. *Water Resources Research* 22, no. 9: 120-134.

Dagan, G., and S.P. Neuman. 2005. *Subsurface flow and transport: A stochastic approach.* Cambridge, UK: Cambridge University Press.

Dentz, M., T. Le Borgne, A. Englert, and B. Bijeljic. 2011. Mixing, spreading and reaction in heterogeneous media: A brief review. *Journal of Contaminant Hydrology* 120-121: 1-17.

Freeze, R.A., and J.A. Cherry. 1979. *Groundwater.* Upper Saddle River, NJ: Prentice Hall.

Gale, T., N.R. Thomson, and J.F. Barker. 2015. An investigation of the pressure pulsing reagent delivery approach. *Groundwater Monitoring and Remediation* 35, no. 2: 39-51.

Jose, S.C., and O.A. Cirpka. 2004. Measurement of mixing-controlled reactive transport in homogeneous porous media and its prediction from conservative tracer test data. *Environmental Science and Technology* 38, no. 7: 2089-2096.

Kapoor, V., and P.K. Kitanidis. 1998. Concentration fluctuations and dilution in aquifers. *Water Resources Research* 34, no. 5: 1181-1193.

Kitanidis, P.K. 1988. Prediction by the method of moments of transport in a heterogeneous formation. *Journal of Hydrology* 102*,* 453-473.

Kitanidis, P.K. 1994. The concept of the dilution index. *Water Resources Research* 30, no. 7: 2011-2026.

Kitanidis, P.K. and P.L. McCarty. 2012. *Delivery and mixing in the subsurface: Processes and design principles for in situ remediation*. New York, NY: Springer.

Le Borgne, T., M. Dentz, D. Bolster, J. Carrera, J.R. de Dreuzy, and P. Davy. 2010. Non-Fickian mixing: Temporal evolution of the scalar dissipation rate in heterogeneous porous media. *Advances in Water Resources* 33: 1468-1475.

Le Borgne, T., M. Dentz, P. Davy, D. Bolster, J. Carrera, J.R. de Dreuzy, and O. Bour. 2011. Persistence of incomplete mixing: A key to anomalous transport. *Physics Review E* 84: 015301(R).

Lester, D.R., G. Metcalfe, M.G. Trefry, A. Ord, B. Hobbs, and M. Rudman. 2009. Lagrangian topology of a periodically reoriented potential flow: Symmetry, optimization, and mixing. *Physical Review E* 80, no. 3: 036208.

Lester, D.R., M. Rudman, G. Metcalfe, M.G. Trefry, A. Ord, and B. Hobbs. 2010a. Scalar dispersion in a periodically reoriented potential flow: Acceleration via Lagrangian chaos. *Physical Review E* 81, no. 4: 046319.

Lester, D.R., G. Metcalfe, and M.G. Trefry. 2010b. Subsurface stirring for enhanced yields from *in situ* recovery operations. Internal CSIRO report: Report No. EP-104-633.

Liebeg, E.W., and T.J. Cutright. 1999. The investigation of enhanced bioremediation through the addition of macro and micro nutrients in a PAH contaminated soil. *International Biodeterioration and Biodegradation* 44: 55-64.

Mackay, D.M., D.L. Freyberg, P.V. Roberts, and J.A. Cherry. 1986. A natural gradient experiment on solute transport in a sand aquifer: 1. Approach and overview on plume movement. *Water Resources Research* 22, no. 13: 2017-2029.

Mays, D.C., and R.M. Neupauer. 2012. Plume spreading in groundwater by stretching and folding. *Water Resources Research* 48, no. 7: W07501.

Metcalfe, G., D.R. Lester, M.G. Trefry, and A. Ord. 2008 Transport in a partially open porous media flow. In *Proceedings of SPIE: Complex systems II,* vol. 6802. Bellingham, WA.

Metcalfe, G., D.R. Lester, A. Ord, P. Kulkarni, M. Rudman, M.G. Trefry, . . . J. Morris. 2010a. An experimental and theoretical study of the mixing characteristics of a periodically reoriented irrotational flow. *Philosophical Transactions of the Royal Society A: Mathematical, Physical and Engineering Sciences* 368, no. 1918: 2147-2162.

Metcalfe, G., D.R. Lester, A. Ord, P. Kulkarni, M. Rudman, M.G. Trefry, . . . J. Morris. 2010b. A partially open porous media flow with chaotic advection: Towards a model of coupled fields. *Philosophical Transactions of the Royal Society A: Mathematical, Physical and Engineering Sciences* 368, no. 1918: 217-230.

Metcalfe, G., D.R. Lester, M.G. Trefry, and K. Regenauer-Lieb. 2011. Method, system and apparatus for subsurface flow manipulation, Patent Numbers WO2011017771-A1; PCT/AU2010/001040; Australia 2009903821, Derwent Primary Accession Number: 2011-B76151.

Moon, F.C. 2008. *Chaotic and fractal dynamics: Introduction for applied scientists and engineers*. New York, NY: John Wiley and Sons.

Neupauer, R.M., J.D. Meiss, and D.C. Mays. 2014. Chaotic advection and reaction during engineered injection and extraction in heterogeneous porous media. *Water Resources Research* 50, no. 2: 1433-1447.

Nissan, A., I. Dror, and B. Berkowitz. 2017. Time-dependent velocity-field controls on anomalous chemical transport in porous media. *Water Resources Research* 53: 3760-3769.

Ottino, J.M. 1989. *The kinematics of mixing: Stretching, chaos and transport.* New York, NY: Cambridge University Press.

Ottino, J.M. 1990. Mixing, chaotic advection and turbulence. *Annual Review of Fluid Mechanics* 22: 207-253.

Pannone, M., and P.K. Kitanidis. 2001. Large-time spatial covariance of concentration of conservative solute and application to the Cape Cod tracer test. *Transport in Porous Media* 42: 109-132.

Parker, B.L., R.W. Gillham, and J.A. Cherry. 1994. Diffusive disappearance of immiscible-phase organic liquids in fractured geologic media. *Ground Water* 32, no. 5: 805–820.

Payne, F.C., J.A. Quinnan, and S.T. Potter. 2008. *Remediation hydraulics.* Boca Raton, FL: CRC Press.

Reinhard, M., S. Shang, P.K. Kitanidis, E. Orwin, G.D. Hopkins, and C.A. Lebron. 1997. In situ BTEX biotransformation under enhanced nitrate- and sulfate-reducing conditions. *Environmental Science and Technology* 31, no. 1: 28-36.

Ritchie, J.T. 1974. Atmospheric and soil water influences on the plant water balance. *Agricultural Meteorology* 14: 183-198.

Rodriguez-Escales, P., D. Fernandez-Garcia, J. Drechsel, A. Folch, and X. Sanchez-Vila. 2017. Improving degradation of emerging organic compounds by applying chaotic advection in managed aquifer recharge in randomly heterogeneous porous media. *Water Resources Research* 53, no. 5: 4376-4392.

Saenton, S., T.H. Illangasekare, K. Soga, and T.A. Saba. 2002. Effects of source zone heterogeneity on surfactant-enhanced NAPL dissolution and resulting remediation end-points. *Journal of Contaminant Hydrology* 59: 27-44.

Scheibe, T., and S. Yabusaki. 1998. Scaling of flow and transport behavior in heterogeneous groundwater systems. *Advances in Water Resources* 22, no. 3: 223-238.

Siegrist, R.L, and T.J. Simpkin. 2016. *In situ* chemical oxidation for groundwater remediation. New York, NY: Springer.

Sposito, G. 2006. Chaotic solute advection by unsteady groundwater flows. *Water Resources Research* 42: W06D03.

Sposito, G. 1998. *Scale Dependence and Scale Invariance in Hydrology*. New York: Cambridge University Press.

Stevenson, D., F. Solano, Y. Wei, N.R. Thomson, and J.F. Barker. 2018. Simple probe system for real-time in situ monitoring of reagent applications. *Manuscript in preparation.*

Sudicky, E.A. 1986. A natural gradient experiment on solute transport in a sand aquifer: spatial variability of hydraulic conductivity and its role in the dispersion process. *Water Resources Research* 22: 2069–2082.

Thomson, N.R, M.J. Fraser, C. Lamarche, J.F. Barker, and S.P. Forsey. 2008. Rebound of a coal tar creosote plume following partial source zone treatment with permanganate. *Journal of Contaminant Hydrology* 102: 154–171.

Trefry, M.G., D.R. Lester, G. Metcalfe, A. Ord, and K. Regenauer-Lieb. 2012. Toward enhanced subsurface intervention methods using chaotic advection. *Journal of Contaminant Hydrology* 127: 15-29.

Zhang, P., S.L. Devries, A. Dathe, and A.C. Bagtzoglou. 2009. Enhanced mixing and plume containment in porous media under time-dependent oscillatory flow. *Environmental Science and Technology* 43, no. 16: 6283-6288.

Zhong, L., J. Szecsody, M. Oostrom, M. Truex, X. Shen, and X. Li. 2011. Enhanced remedial amendment delivery to subsurface using shear thinning fluid and aqueous foam. *Journal of Hazardous Materials* 191: 249-257.

Chapter 3

Aref, H., Blake, J.R., Budisic, M., Cardoso, S.S.S., Cartwright, J.H.E., Clercx, H.J.H, El Omari, K., … Tuval, I., 2017. Frontiers of chaotic advection. Rev. Mod. Phys. 89 (2), 025007. https://doi.org/10.1103/RevModPhys.89.025007.

Bagtzoglou, A.C., Oates, P.M., 2007. Chaotic advection and enhanced groundwater remediation. J. Mat. Civil Eng. 19 (1), 75-83. https://doi.org/10.1061/(ASCE)0899-1561(2007)19:1(75).

Berg, S.J., Illman, W.A., 2011a. Capturing aquifer heterogeneity: Comparison of approaches through controlled sandbox experiments. Water Resour. Res. 47, W09514. https://doi.org/10.1029/2011WR010429.

Berg, S.J., Illman, W.A., 2011b. Three-dimensional transient hydraulic tomography in a highly heterogeneous glaciofluvial aquifer-aquitard system. Water Resour. Res. 47, W10507. https://doi.org/10.1029/2011WR010616.

Berg, S.J., Illman, W.A., 2013. Field study of subsurface heterogeneity with steady-state hydraulic tomography. Ground Water. 51 (1), 29-40. https://doi.org/10.1111/j.1745-6584.2012.00914.x.

Berg, S.J., Illman, W.A., 2015. Comparison of hydraulic tomography with traditional methods at a highly heterogeneous site. Ground Water. 53 (1), 71-89. https://doi.org/10.1111/gwat.12159.

Brauchler, R., Hu, R., Dietrich, P., Sauter, M., 2011. A field assessment of high-resolution aquifer characterization based on hydraulic travel time and hydraulic attenuation tomography. Water Resour. Res. 47, W03503. https://doi.org/10.1029/2010WR009635.

Cardiff, M., Barrash, W., Kitanidis, P.K., 2012. A field proof-of-concept of aquifer imaging using 3-D transient hydraulic tomography with modular, temporarily-emplaced equipment. Water Resour. Res. 48, W05531. https://doi.org/10.1029/2011WR011704.

Chatterjee, S., Hadi, A.S., 1986. Influential observations, high leverage points, and outliers in linear regression. Stat. Sci. 1 (3), 379-416.

Dagan, G., 1986. Statistical theory of groundwater flow and transport: Pore to laboratory, laboratory to formation, and formation to regional scale. Water Resour. Res. 22 (9), 120-134. https://doi.org/10.1029/WR022i09Sp0120S.

Dagan, G., Neuman, S.P., 2005. Subsurface Flow and Transport: A Stochastic Approach. Cambridge University Press, Cambridge, UK.

Freeze, R.A., Cherry, J.A., 1979. Groundwater. Prentice Hall, Upper Saddle River, USA.

Frind, E.O., Molson, J.W., Schirmer, M., 1999. Dissolution and mass transfer of multiple organics under field conditions: The Borden emplaced source. Water Resour. Res. 35 (3), 683-694. https://doi.org/10.1029/1998WR900064.

Gale, T., Thomson, N.R., Barker, J.F., 2015. An investigation of the pressure pulsing reagent delivery approach. Ground Water Monit. R. 35 (2), 39-51. https://doi.org/10.1111/gwmr.12102.

Hoaglin, D.C., Welsch, R.E., 1978. The hat matrix in regression and ANOVA. Am. Stat. 32 (1), 17-22. https://doi.org/10.2307/2683469.

Hochstetler, D.L., Barrash, W., Leven, C., Cardiff, M., Chidichimo, F., Kitanidis, P.K., 2016. Hydraulic tomography: Continuity and discontinuity of high-K and low-K zones. Ground Water. 54 (2), 171-185. https://doi.org/10.1111/gwat.12344.

Illman, W.A., Liu, X., Craig, A.J., 2007. Steady-state hydraulic tomography in a laboratory aquifer with deterministic heterogeneity: Multi-method and multiscale validation of hydraulic conductivity tomograms. J. Hydrol. 341, 222-234. https://doi.org/10.1016/j.jhydrol.2007.05.011.

Illman, W.A., Craig, A.J., Liu, X., 2008. Practical issues in imaging hydraulic conductivity through hydraulic tomography. Ground Water. 46 (1), 120-132. https://doi.org/10.1111/j.1745-6584.2007.00374.x.

Kitanidis, P.K., McCarty, P.L. Delivery & Mixing in the Subsurface: Processes & Design Principles for In Situ Remediation. Springer, New York.

Lester, D. R., Metcalfe, G., Trefry, M. G., Ord, A., Hobbs, B., Rudman, M., 2009. Lagrangian topology of a periodically reoriented potential flow: Symmetry, optimization, and mixing. Phys. Rev. E. 80 (3). https://doi.org/10.1103/PhysRevE.80.036208.

Lester, D.R., Rudman, M., Metcalfe, G., Trefry, M.G., Ord, A., Hobbs, B., 2010. Scalar dispersion in a periodically reoriented potential flow: Acceleration via Lagrangian chaos. Phys. Rev. E. 81 (4), 046319. https://doi.org/10.1103/PhysRevE.81.046319.

Liu, X., Illman, W.A., Craig, A.J., Zhu, J., Yeh, T.-C. J., 2007. Laboratory sandbox validation of transient hydraulic tomography. Water Resour. Res. 43, W050404. https://doi.org/10.1029/2006WR005144.

Mackay, D.M., Freyberg, D.L., Roberts, P.V., Cherry, J.A., 1986. A natural gradient experiment on solute transport in a sand aquifer: 1. Approach and overview of plume movement. Water Resour. Res. 22 (13): 2017-2029. https://doi.org/10.1029/WR022i013p02017.

Mays, D.C., Neupauer, R.M., 2012. Plume spreading in groundwater by stretching and folding. Water Resour. Res. 48 (7), https://doi.org/10.1029/2011WR011567.

McCuen, R.H., Snyder, W.M., 1986. Hydrologic Modeling: Statistical Methods and Applications. Prentice-Hall, New Jersey.

Metcalfe, G., Lester, D., Trefry, M., Ord, A., 2008. Transport in a partially open porous media flow. Proc. SPIE 6802. https://doi.org/10.1117/12.769319 (Article 680201).

Metcalfe, G., Lester, D., Ord, A., Kulkarni, P., Rudman, M., Trefry, M., Hobbs, B., Regenauer-Lieb, K., Morris, J., 2010. An experimental and theoretical study of the mixing characteristics of a periodically reoriented irrotational flow. Philos. Trans. R. Soc. A. 368, 2147-2162. https://doi.org/10.1098/rsta.2010.0037.

Moench, A.F., 2008. Analytical and numerical analyses of an unconfined aquifer test considering unsaturated zone characteristics. Water Resour. Res. 44, W06409. https://doi.org/10.1029/2006WR005736.

Neupauer, R.M., Meiss, J.D., Mays, D.C., 2014. Chaotic advection and reaction during engineered injection and extraction in heterogeneous porous media. Water Resour. Res. 50 (2), 1433-1447. https://doi.org/10.1002/2013WR014057.

Ottino, J.M., 1989. The Kinematics of Mixing: Stretching, Chaos and Transport. Cambridge University Press, New York.

Paradis, D., Gloaguen, E., Lefebvre, R., Giroux, B., 2016. A field proof-of-concept of tomographic slug tests in an anisotropic littoral aquifer. J. Hydrol. 536, 61-73. https://doi.org/10.1016/j.jhydrol.2016.02.041.

Payne, F.C., Quinnan, J.A., Potter, S.T., 2008. Remediation Hydraulics. CRC Press, Boca Raton.

Rivett, M.O., Feenstra, S., Cherry, J.A., 1994. Transport of a dissolved phase plume from a residual solvent source in a sand aquifer. J. Hydrol. 159 (1–4): 27–41. https://doi.org/10.1016/0022-1694(94)90247-X.

Saenton, S., Illangasekare, T.H., Soga, K., Saba, T.A., 2002. Effects of source zone heterogeneity on surfactant-enhanced NAPL dissolution and resulting remediation end-points. J. Contam. Hydrol. 59, 27-44. https://doi.org/10.1016/S0169-7722(02)00074-8.

Scheibe, T., Yabusaki, S., 1998. Scaling of flow and transport behavior in heterogeneous groundwater systems. Adv. Water Resour. 22 (3): 223-238. https://doi.org/10.1016/S0309-1708(98)00014-1.

Sudicky, E.A., 1986. A natural gradient experiment on solute transport in a sand aquifer: Spatial variability of hydraulic conductivity and its role in the dispersion process. Water Resour. Res. 22, 2069–2082. https://doi.org/10.1029/WR022i013p02069.

Sudicky, E.A., Illman, W.A., Goltz, I.K., Adams, J.J., McLaren, R.G., 2010. Heterogeneity in hydraulic conductivity and its role on the macroscale transport of a solute plume: From measurements to a practical application of stochastic flow and transport theory. Water Resour. Res. 46, W01508. https://doi.org/10.1029/2008WR007558.

Tomlinson, D., Thomson, N.R., Johnson, R.L., Redman, D., 2003. Air distribution in the Borden aquifer during in situ air sparging. J. Contam. Hydrol. 67 (1–4): 113–132. https://doi.org/10.1016/S0169-7722(03)00070-6.

Thomson, N. R., Fraser, M. J., Lamarche, C., Barker, J.F., Forsey, S.P., 2008. Rebound of a coal tar creosote plume following partial source zone treatment with permanganate. J. Contam. Hydrol. 102, 154–171. https://doi.org/10.1016/j.jconhyd.2008.07.001.

Trefry, M.G., Lester, D.R., Metcalfe, G., Ord, A., Regenauer-Lieb, K., 2012. Toward enhanced subsurface intervention methods using chaotic advection. J. Contam. Hydrol. 127 (1-4), 15-29. https://doi.org/10.1016/j.jconhyd.2011.04.006.

Turcke, M.A., Kueper, B.H., 1996. Geostatistical analysis of the Borden aquifer hydraulic conductivity field. J. Hydrol. 178 (1-4), 223-240. https://doi.org/10.1016/0022-1694(95)02805-6.

Woodbury, A.D., Sudicky, E.A., 1991. The geostatistical characteristics of the Borden aquifer. Water Resour. Res. 27 (4), 533-546. https://doi.org/10.1029/90WR02545.

Yeh, T.-C. J., Liu, S., 2000. Hydraulic tomography: Development of a new aquifer test method. Water Resour. Res. 36 (8), 2095-2105. https://doi.org/10.1029/2000WR900114.

Xiang, Y., Thomson, N.R., Sykes, J.F., 1992. Fitting a groundwater contaminant transport model by L1 and L2 parameter estimators. Adv. Water Resour. 15, 303-310. https://doi.org/10.1016/0309-1708(92)90016-U

Zhao, Z., Illman, W.A., 2018. Three-dimensional imaging of aquifer and aquitard heterogeneity via transient hydraulic tomography at a highly heterogeneous field site. J. Hydrol. 559, 392-410. https://doi.org/10.1016/j.jhydrol.2018.02.024.

Zhong, L., Szecsody, J., Oostrom, M., Truex, M., Shen, X., Li, X., 2011. Enhanced remedial amendment delivery to subsurface using shear thinning fluid and aqueous foam. J. Hazard. Mat. 191, 249-257. https://doi.org/10.1016/j.jhazmat.2011.04.074.

Zhu, J., Yeh, T.-C. J., 2005. Characterization of aquifer heterogeneity using transient hydraulic tomography. Water Resour. Res. 41, W07028. https://doi.org/10.1029/2004WR003790.

Chapter 4

Aref, H., 1984. Stirring by chaotic advection. J. Fluid Mech. 143, 1-21. https://doi.org/10.1017/S0022112084001233.

Aref, H., Blake, J.R., Budisic, M., Cardoso, S.S.S., Cartwright, J.H.E., Clercx, H.J.H, El Omari, K., … Tuval, I., 2017. Frontiers of chaotic advection. Rev. Mod. Phys. 89 (2), 025007. https://doi.org/10.1103/RevModPhys.89.025007.

Bagtzoglou, A.C., Oates, P.M., 2007. Chaotic advection and enhanced groundwater remediation. J. Mat. Civil Eng. 19 (1), 75-83. https://doi.org/10.1061/(ASCE)0899-1561(2007)19:1(75).

Cho, M.S., Solano, F., Thomson, N.R., Trefry, M.G., Lester, D.R., Metcalfe, G., 2018a. Field trials of chaotic advection to enhance reagent delivery. Manuscript submitted for publication.

Cho, M.S., Zhao, Z., Thomson, N.R., Illman, W.A., 2018b. Combining periodically re-oriented dipole pumping with 3D steady-state hydraulic tomography as a new design tool for chaotic advection. Manuscript submitted for publication.

Dagan, G., 1986. Statistical theory of groundwater flow and transport: Pore to laboratory, laboratory to formation, and formation to regional scale. Water Resour. Res. 22 (9), 120-134. https://doi.org/10.1029/WR022i09Sp0120S.

Dentz, M., Le Borgne, T., Englert, A., Bijeljic., B., 2011. Mixing, spreading and reaction in heterogeneous media: A brief review. J. Contam. Hydrol. 120-121, 1-17. https://doi.org/10.1016/j.jconhyd.2010.05.002.

Dentz, M., Le Borgne, T., Lester, D.R., de Barros, F.P.J., 2017. Mixing in groundwater, in Cushman, J.H., Tartakovsky, D.M. (Eds.), Handbook of Groundwater Engineering. CRC Press, Florida, pp. 383-411.

Gale, T., Thomson, N.R., Barker, J.F., 2015. An investigation of the pressure pulsing reagent delivery approach. Ground Water Monit. R. 35 (2), 39-51. https://doi.org/10.1111/gwmr.12102.

Garder, A.O., Peaceman, D.W., Pozzi, A.L. 1964. Numerical calculation of the multidimensional miscible displacement by the method of characteristics. SPE J. 4 (1), 26-36. https://doi.org/10.2118/683-PA.

Harbaugh, A.W., 2005. MODFLOW-2005, the U.S. Geological Survey modular ground-water model—the ground-water flow process. U.S. Geological Survey Techniques and Methods, Report 6-A16. https://doi.org/10.3133/tm6A16.

Harbaugh, A.W., Banta, E., Hill, M., McDonald, M., 2000. MODFLOW- 2000, the U.S. Geological Survey modular ground-water model: User guide to modularization concepts and the ground-water flow process. U.S. Geological Survey Open-File Report 00-92. https://doi.org/10.3133/ofr200092.

Illman, W.A., Berg, S.J., Yeh, T.-C.J., 2012. Comparison of approaches for predicting solute transport: Sandbox experiments. Ground Water. 50 (3), 421-431. https://doi.org/10.1111/j.1745-6584.2011.00859.x.

Jones, S.W., Aref, H., 1988. Chaotic advection in pulsed source sink systems. Phys. Fluids. 31 (3), 469-485. https://doi.org/10.1063/1.866828.

Jose, S. C., Cirpka, O. A., 2004. Measurement of mixing-controlled reactive transport in homogeneous porous media and its prediction from conservative tracer test data. Environ. Sci. Technol. 38 (7), 2089-2096. https://doi.org/10.1021/es034586b.

Kapoor, V., Kitanidis, P.K., 1998. Concentration fluctuations and dilution in aquifers. Water Resour. Res. 34 (5), 1181-1193. https://doi.org/10.1029/97WR03608.

Kitanidis, P.K., 1988. Prediction by the method of moments of transport in a heterogeneous formation. J. Hydrol. 102, 453-473. https://doi.org/10.1016/0022-1694(88)90111-4.

Kitanidis, P.K., 1994. The concept of the dilution index. Water Resour. Res. 30 (7): 2011-2026. https://doi.org/10.1029/94WR00762.

Kitanidis, P.K., McCarty, P.L. Delivery and Mixing in the Subsurface: Processes and Design Principles for In Situ Remediation. Springer, New York.

Le Borgne, T., Dentz, M., Bolster, D., Carrera, J., de Dreuzy, J.R., Davy, P. 2010. Non-Fickian mixing: Temporal evolution of the scalar dissipation rate in heterogeneous porous media. Adv. Water Resour. 33, 1468-1475. https://doi.org/10.1016/j.advwatres.2010.08.006.

Le Borgne, T., Dentz, M., Davy, P., Bolster, D., Carrera, J., de Dreuzy, J.R., Bour. O., 2011. Persistence of incomplete mixing: A key to anomalous transport. Phys. Rev. E. 84 (1), 015301(R). https://doi.org/10.1103/PhysRevE.84.015301.

Lester, D. R., Metcalfe, G., Trefry, M. G., Ord, A., Hobbs, B., Rudman, M., 2009. Lagrangian topology of a periodically reoriented potential flow: Symmetry, optimization, and mixing. Phys. Rev. E. 80 (3). https://doi.org/10.1103/PhysRevE.80.036208.

Lester, D.R., Rudman, M., Metcalfe, G., Trefry, M.G., Ord, A., Hobbs, B., 2010. Scalar dispersion in a periodically reoriented potential flow: Acceleration via Lagrangian chaos. Phys. Rev. E. 81 (4), 046319. https://doi.org/10.1103/PhysRevE.81.046319.

Lester, D.R., Metcalfe, G., Trefry, M.G., 2013. Is chaotic advection inherent to porous media flow? Phys. Rev. Lett. 111, 174101. https://doi.org/10.1103/PhysRevLett.111.174101.

Mays, D.C., Neupauer, R.M., 2012. Plume spreading in groundwater by stretching and folding. Water Resour. Res. 48 (7), https://doi.org/10.1029/2011WR011567.

Metcalfe, G., Lester, D., Trefry, M., Ord, A., 2008. Transport in a partially open porous media flow. Proc. SPIE 6802. https://doi.org/10.1117/12.769319 (Article 680201).

Metcalfe, G., Lester, D., Ord, A., Kulkarni, P., Rudman, M., Trefry, M., Hobbs, B., Regenauer-Lieb, K., Morris, J., 2010. An experimental and theoretical study of the mixing characteristics of a periodically reoriented irrotational flow. Philos. Trans. R. Soc. A. 368, 2147-2162. https://doi.org/10.1098/rsta.2010.0037.

Metcalfe, G., Lester, D.R., Trefry, M.G., Regenauer-Lieb, K. 2011. Method, system and apparatus for subsurface flow manipulation, Patent Numbers WO2011017771-A1; PCT/AU2010/001040; Australia 2009903821, Derwent Primary Accession Number: 2011-B76151.

Moon, F.C., 2008. Chaotic and fractal dynamics: Introduction for applied scientists and engineers. John Wiley and Sons, New York.

Neupauer, R.M., Meiss, J.D., Mays, D.C., 2014. Chaotic advection and reaction during engineered injection and extraction in heterogeneous porous media. Water Resour. Res. 50 (2), 1433-1447. https://doi.org/10.1002/2013WR014057.

Ottino, J.M., 1989. The Kinematics of Mixing: Stretching, Chaos and Transport. Cambridge University Press, New York.

Pannone, M., Kitanidis, P.K., 2001. Large-time spatial covariance of concentration of conservative solute and application to the Cape Cod tracer test. Trans. Porous Med. 42, 109-132. https://doi.org/10.1023/A:1006704215335.

Parkhurst, D. L., Appelo, C.A.J., 1999. User's guide to PHREEQC (version 2): A computer program for speciation, reaction-path, 1D- transport, and inverse geochemical calculations. U.S. Geological Survey Water Resources Investigations Report, 99–4259. https://doi.org/10.3133/wri994259.

Payne, F.C., Quinnan, J.A., Potter, S.T., 2008. Remediation Hydraulics. CRC Press, Boca Raton.

Pollock, D.W., 1994. User's guide for MODPATH/MODPATH-PLOT, version 3: A particle tracking post-processing package for MODFLOW, the U.S. Geological Survey finite-difference ground-water flow model. U.S. Geological Survey Open-File Report, 94-464. https://doi.org/10.3133/ofr94464.

Prommer, H., Post, V., 2010. A Reactive Multicomponent Transport Model for Saturated Porous Media. User's Manual. v2.10.

Reinhard, M., Shang, S., Kitanidis, P.K., Orwin, E., Hopkins, G.D., Lebron, C.A., 1997. In situ BTEX biotransformation under enhanced nitrate- and sulfate-reducing conditions. Environ. Sci. Technol. 31 (1), 28-36. https://doi.org/10.1021/es9509238.

Robin M.J.L, Gutjahr A.L., Sudicky E.A., Wilson J.L., 1993. Cross-correlated random field generation with the direct Fourier Transform Method. Water Resour. Res. 29 (7), 2385–2397. https://doi.org/10.1029/93WR00386.

Rodriguez-Escales, P., Fernandez-Garcia, D., Drechsel, J., Folch, A., Sanchez-Vila, X., 2017. Improving degradation of emerging organic compounds by applying chaotic advection in managed aquifer recharge in randomly heterogeneous porous media. Water Resour. Res. 53 (5), 4376-4392. https://doi.org/10.1002/2016WR020333.

Saenton, S., Illangasekare, T.H., Soga, K., Saba, T.A., 2002. Effects of source zone heterogeneity on surfactant-enhanced NAPL dissolution and resulting remediation end-points. J. Contam. Hydrol. 59, 27-44. https://doi.org/10.1016/S0169-7722(02)00074-8.

Scheibe, T., Yabusaki, S., 1998. Scaling of flow and transport behavior in heterogeneous groundwater systems. Adv. Water Resour. 22 (3): 223-238. https://doi.org/10.1016/S0309-1708(98)00014-1.

Siegrist, R.L, Crimi, M., Simpkin, T.J., 2016. *In Situ* Chemical Oxidation for Groundwater Remediation. Springer, New York.

Sposito, G., 1998. Scale Dependence and Scale Invariance in Hydrology. Cambridge University Press, New York.

Sposito, G., 2006. Chaotic solute advection by unsteady groundwater flows. Water Resour. Res. 42, W06D03. https://doi.org/10.1029/2005WR004518.

Swanson, P.D., Ottino, J.M., 1990. A comparative computational and experimental-study of chaotic mixing of viscous fluids. J. Fluid Mech. 213, 227-249. https://doi.org/10.1017/S0022112090002300.

Tabor, M., 1989. Chaos and Integrability in Nonlinear Dynamics. John Wiley, New York.

Thomson, N.R., Johnson, R.L., 2000. Air distribution during in situ air sparging: an overview of mathematical modeling. J. Hazard. Mater. 72, 265-282. https://doi.org/10.1016/S0304-3894(99)00143-0.

Thomson, N. R., Fraser, M. J., Lamarche, C., Barker, J.F., Forsey, S.P., 2008. Rebound of a coal tar creosote plume following partial source zone treatment with permanganate. J. Contam. Hydrol. 102, 154–171. https://doi.org/10.1016/j.jconhyd.2008.07.001.

Trefry, M.G., Lester, D.R., Metcalfe, G., Ord, A., Regenauer-Lieb, K., 2012. Toward enhanced subsurface intervention methods using chaotic advection. J. Contam. Hydrol. 127 (1-4), 15-29. https://doi.org/10.1016/j.jconhyd.2011.04.006.

Trefry, M.G., Lester, D.R., Metcalfe, G., Wu, J., 2018. Natural groundwater systems can display chaotic mixing at the Darcy scale. Manuscript submitted for publication.

Zheng, C., Wang, P.P., 1999. MT3DMS: A modular three-dimensional multi-species transport model for simulation of advection, dispersion, and chemical reactions of contaminants in groundwater systems. Report to the US Army Corps of Engineers, Washington, DC.

Zhong, L., Szecsody, J., Oostrom, M., Truex, M., Shen, X., Li, X., 2011. Enhanced remedial amendment delivery to subsurface using shear thinning fluid and aqueous foam. J. Hazard. Mat. 191, 249-257. https://doi.org/10.1016/j.jhazmat.2011.04.074.

Appendix A

Supplementary Figures for Chapter 2

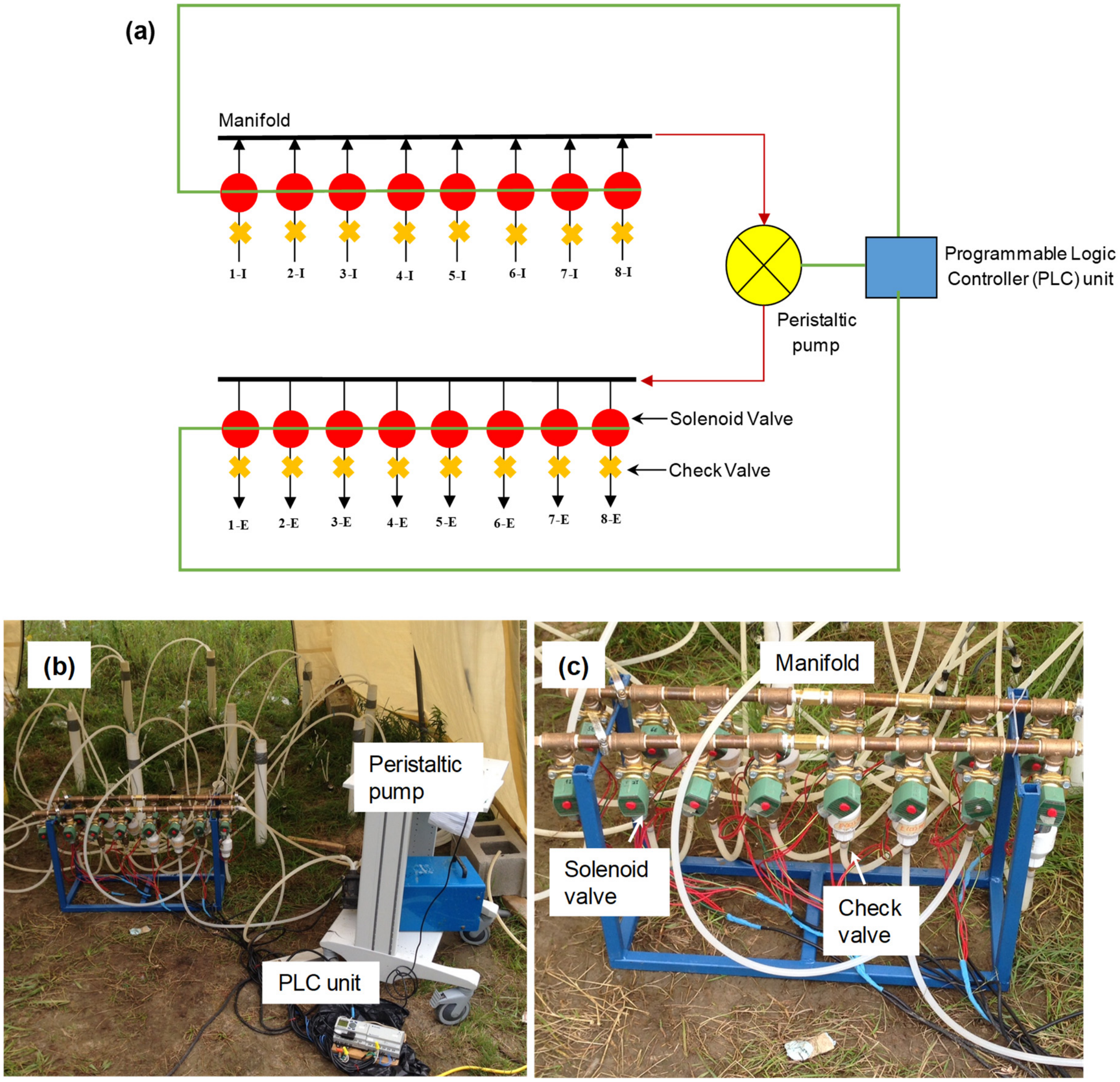

Figure A-1. (a) Schematic of the aboveground dipole pumping system. Arrows indicate direction of flow, numbers indicate the well number in which the tubing was placed, "I" indicates injection port, "E" indicates extraction port, and the green line represents the wiring connection throughout the system; (b) and (c) images of dipole pumping system showing the PLC unit, solenoid valves, check values, and manifold.

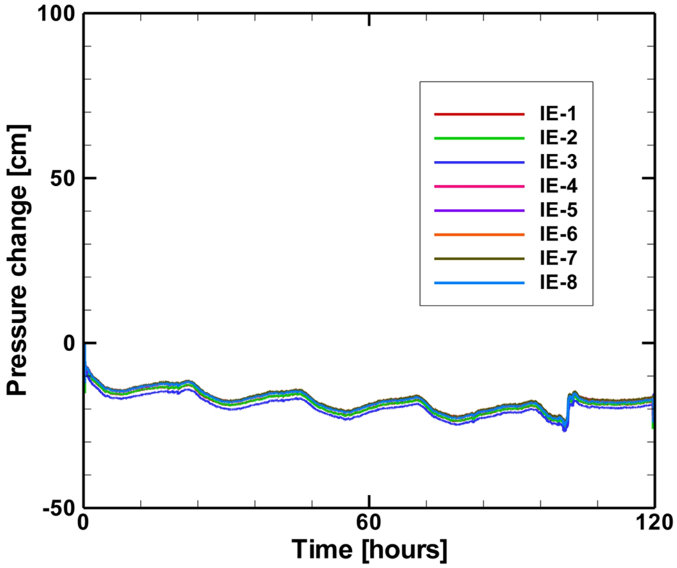

Figure A-2. Pressure change at IE wells during the natural mixing phase of the CTR1-A tracer test.

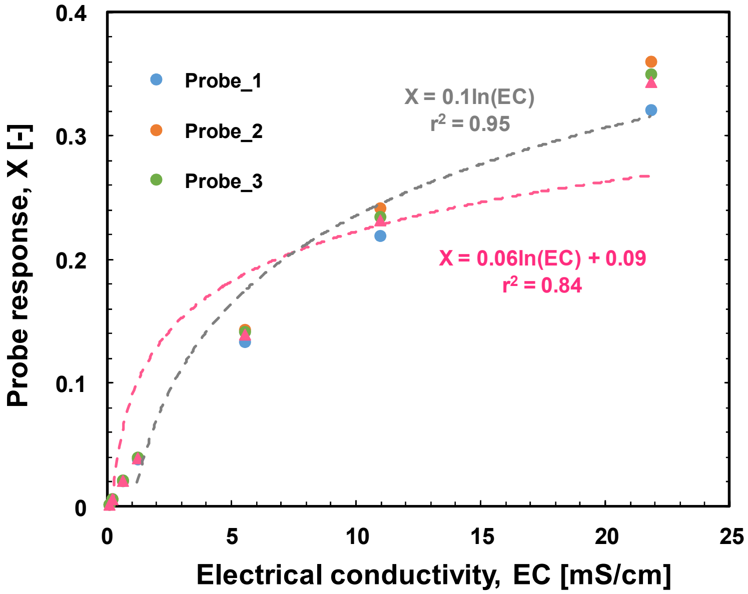

Figure A-3. Calibration curve from the laboratory experiment showing responses from all three DRPs installed in the column, and the EC measured in the effluent. The dashed line represents the best-fit logarithmic relationship for the average observed response from the three DRPs over the entire range of EC values observed (pink symbols and line), and for EC values > 1 mS/cm only (grey symbols and line).

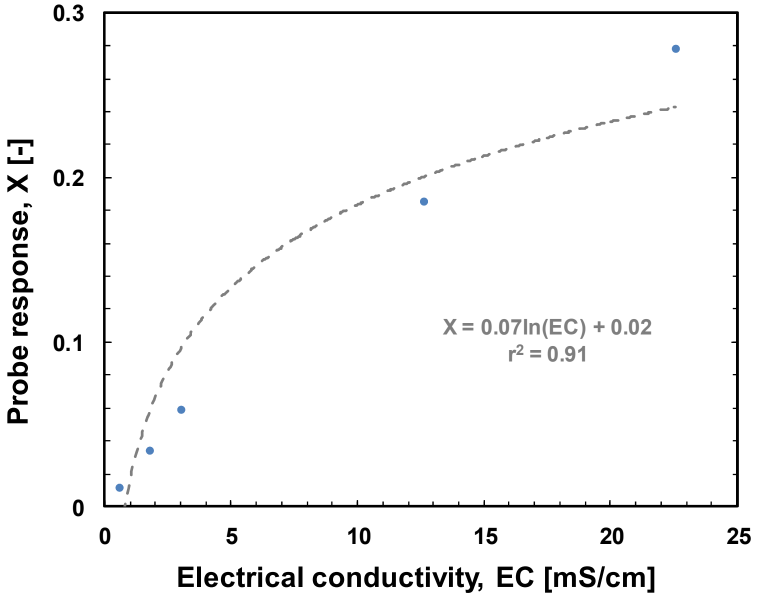

Figure A-4. Field test calibration curve for DRP O1-3 showing the DRP response and EC of the injected solution at the corresponding ML (depth of 1.45 m bgs). Dashed line represents the best-fit logarithm relationship.

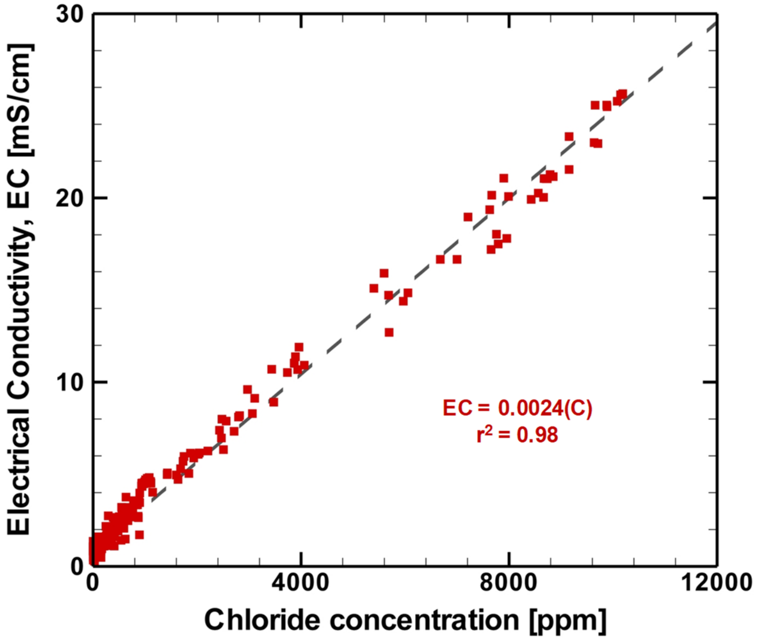

Figure A-5. Relationship between measured EC and chloride concentrations in samples collected from all ML locations and depths. The pooled data shown are from the various tracer tests conducted. The dashed line represents the best linear fit.

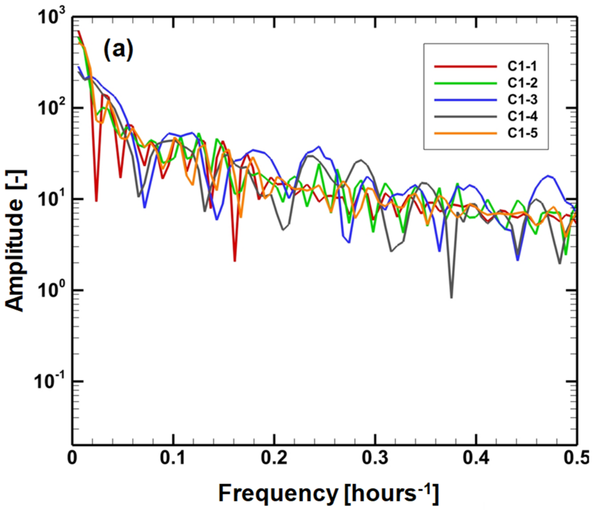

Figure A-6. Frequency spectrum of the temporal DRP responses during the RPM45-A tracer test at location (a) C1, and (b) O6.

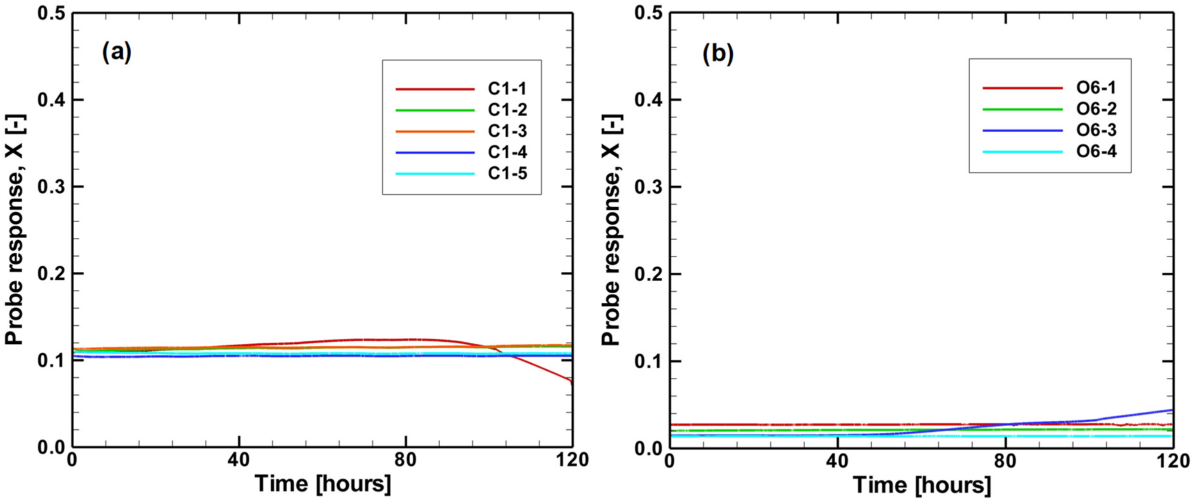

Figure A-7. DRP breakthrough curves observed during the natural mixing phase for the CTR1-A tracer test at location (a) C1, and (b) O6.

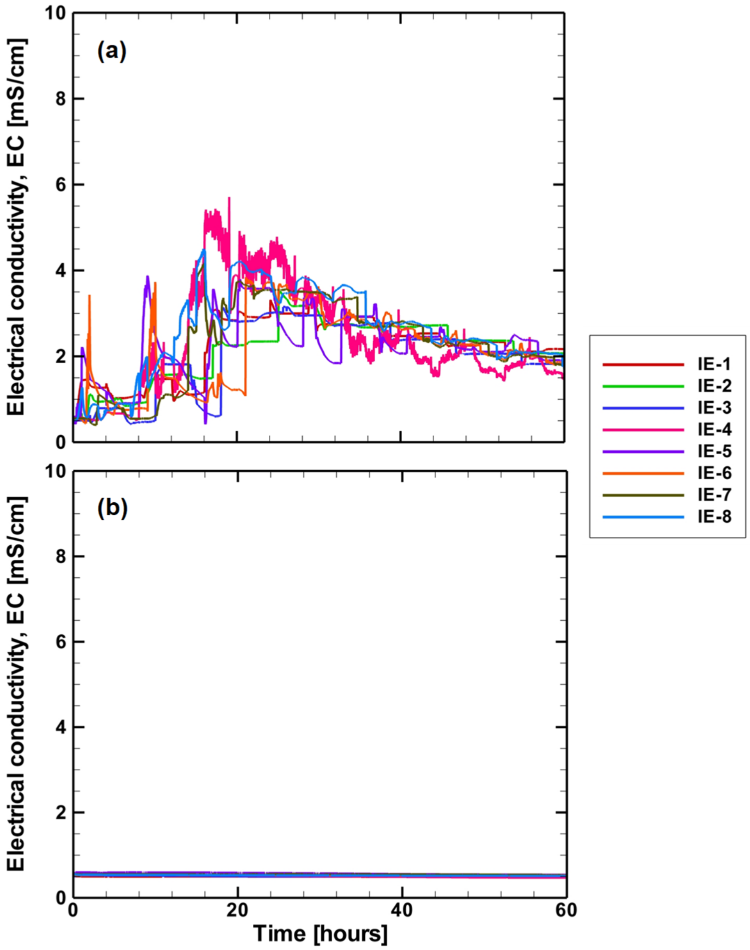

Figure A-8. EC breakthrough curves at the IE wells (a) during the mixing phase for RPM45-A, and (b) during the natural mixing phase for CTR1-A. Red dashed line represents the baseline EC before tracer injection.

Appendix B
Data from the RPM135-A Tracer Test

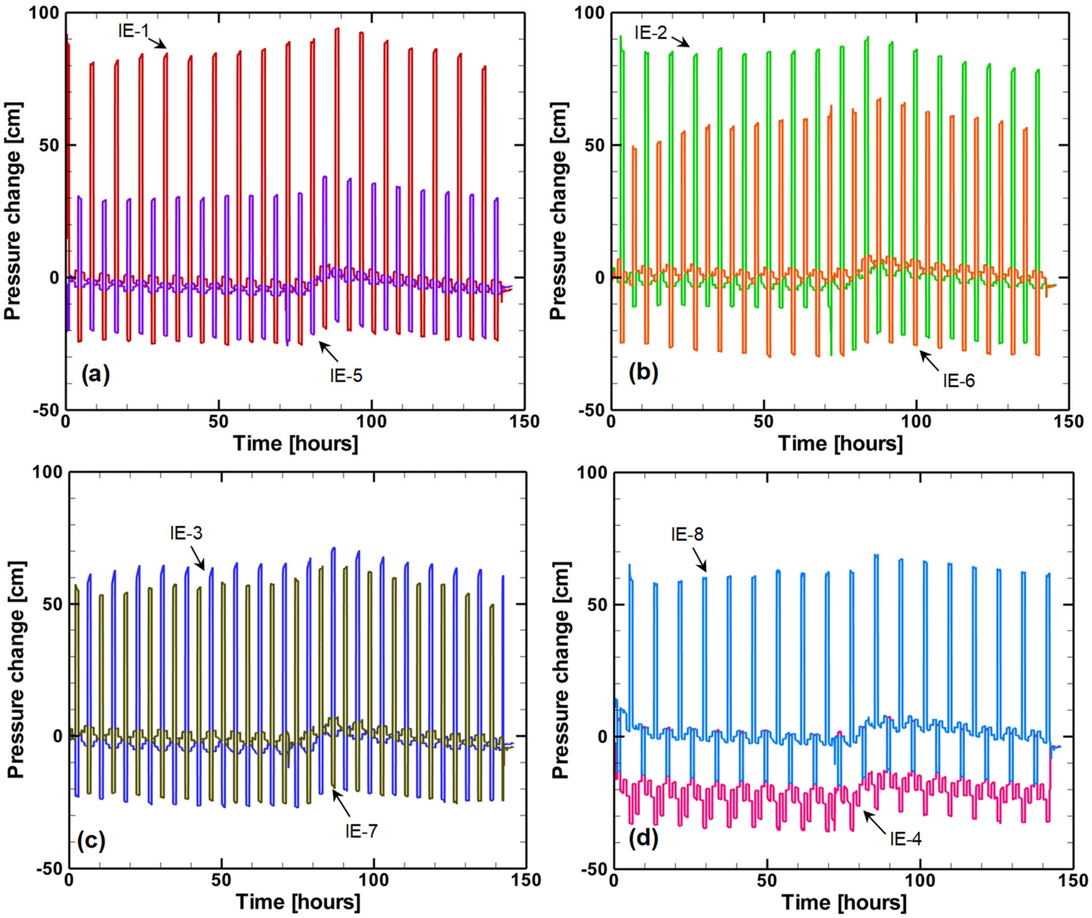

Pressure change during the mixing phase of the RPM135-A tracer test for well pairs: (a) IE-1 & IE-5, (b) IE-2 & IE-6, (c) IE-3 & IE-7 and (d) IE-4 & IE-8.

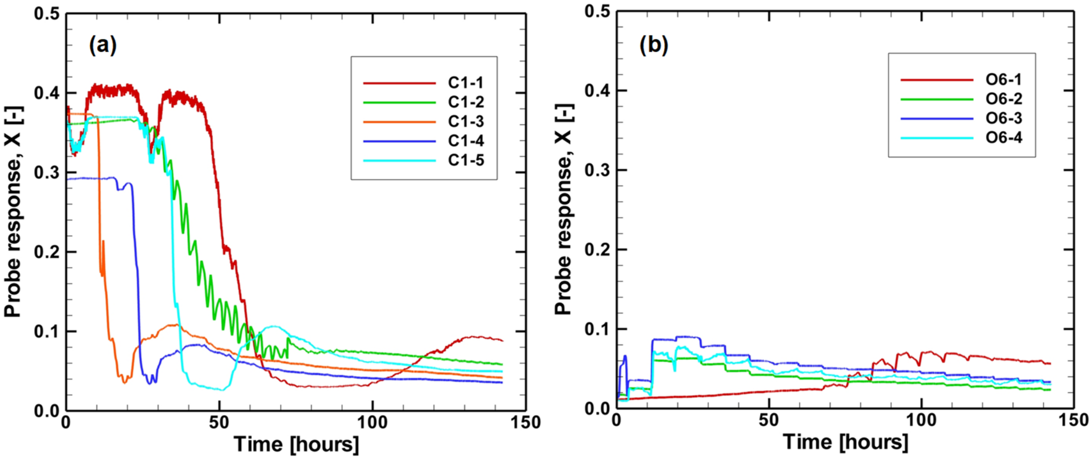

DRP response breakthrough curves during the mixing phase in the RPM135-A tracer test at location (a) C1, and (b) O6.

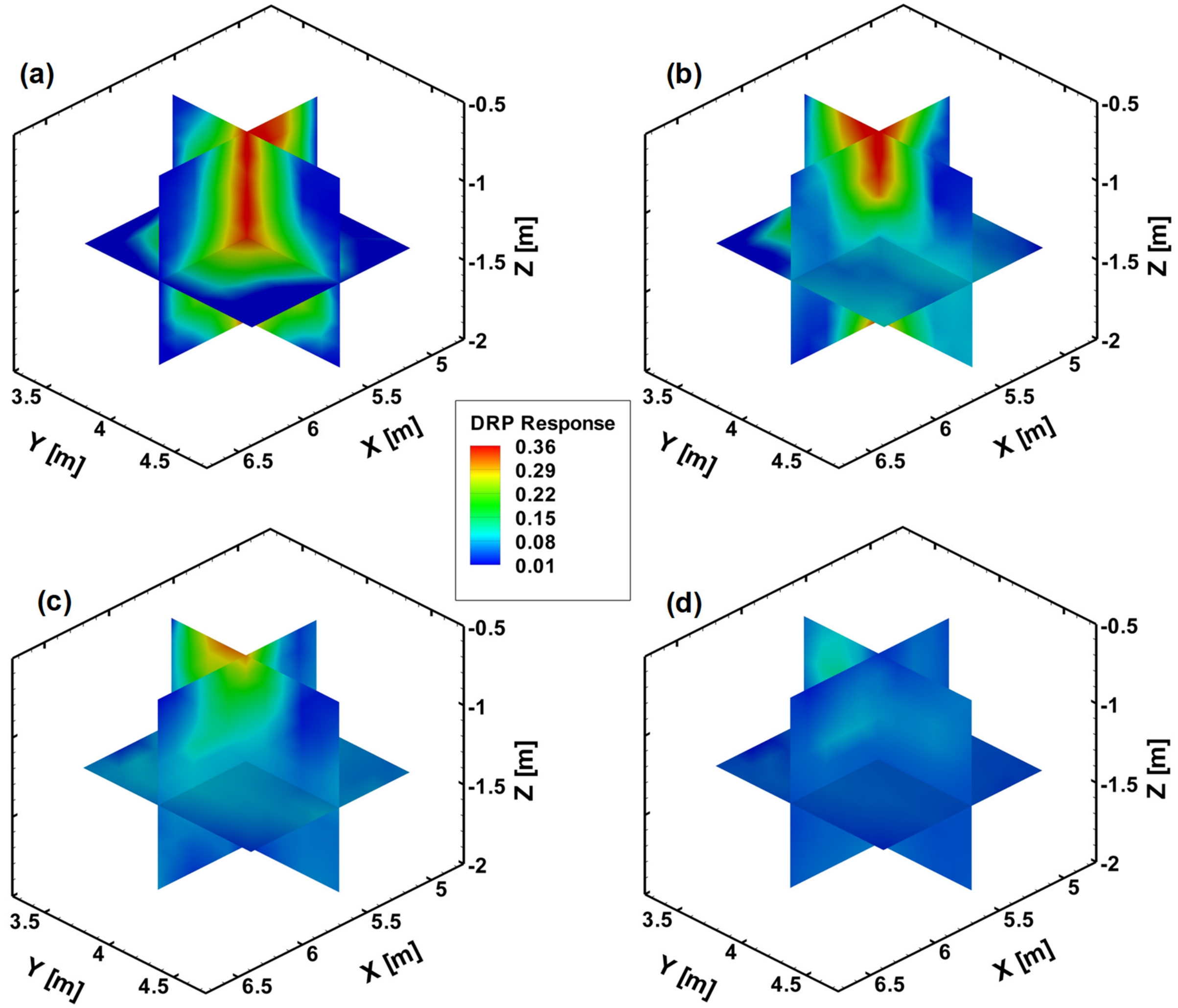

DRP response contours along three orthogonal planes through the center of the screened portion of the IW during the RPM135-A tracer test for (a) post-injection, (b) after 1 day of RPM flow, (c) after 2 days of RPM flow, and (d) after 4 days of RPM flow.

Appendix C
Data from the RPM45-B Tracer Test

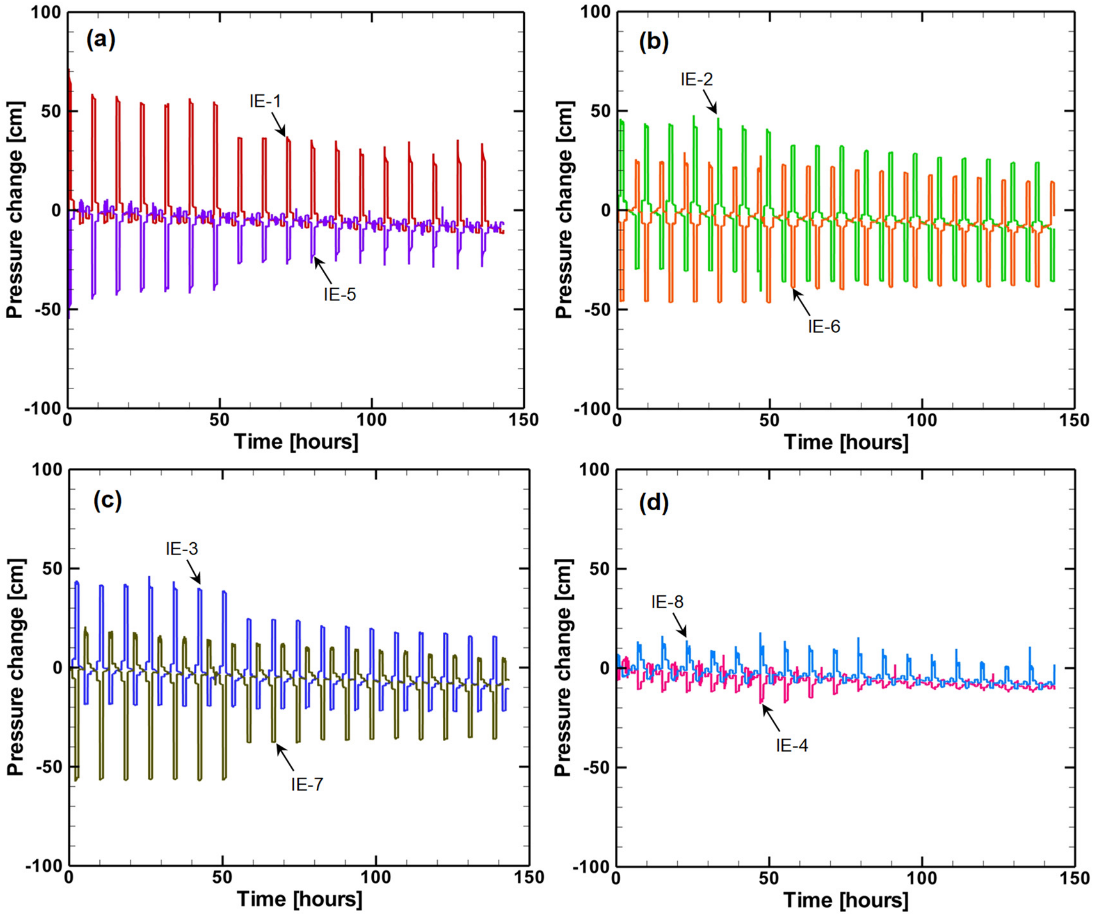

Pressure change during the mixing phase of the RPM45-B tracer test for well pairs: (a) IE-1 & IE-5, (b) IE-2 & IE-6, (c) IE-3 & IE-7 and (d) IE-4 & IE-8.

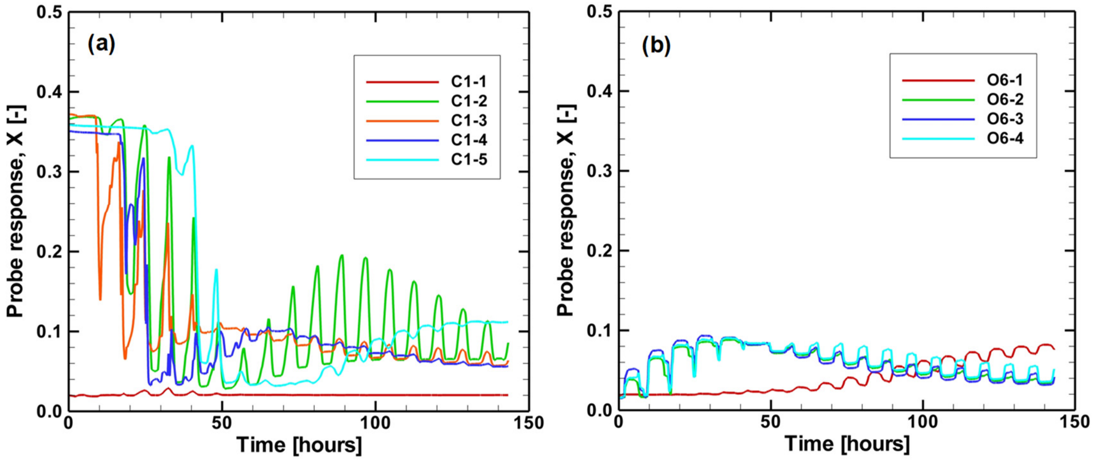

DRP response breakthrough curves during the mixing phase in the RPM45-B tracer test at location (a) C1, and (b) O6.

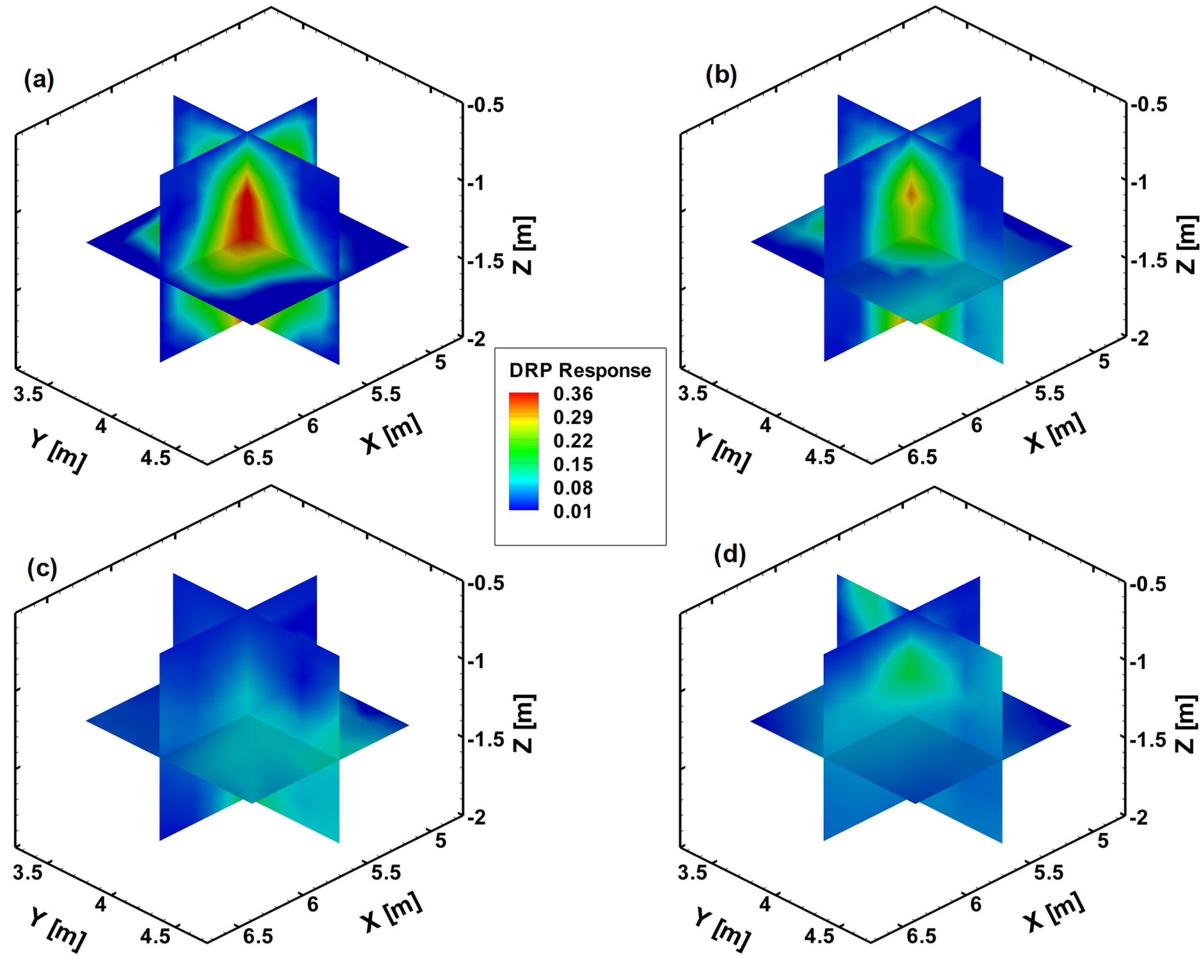

DRP response contours along three orthogonal planes through the center of the screened portion of the IW during the RPM45-B tracer test for (a) post-injection, (b) after 1 day of RPM flow, (c) after 2 days of RPM flow, and (d) after 4 days of RPM flow.

Appendix D

Supplementary Figures for Chapter 3

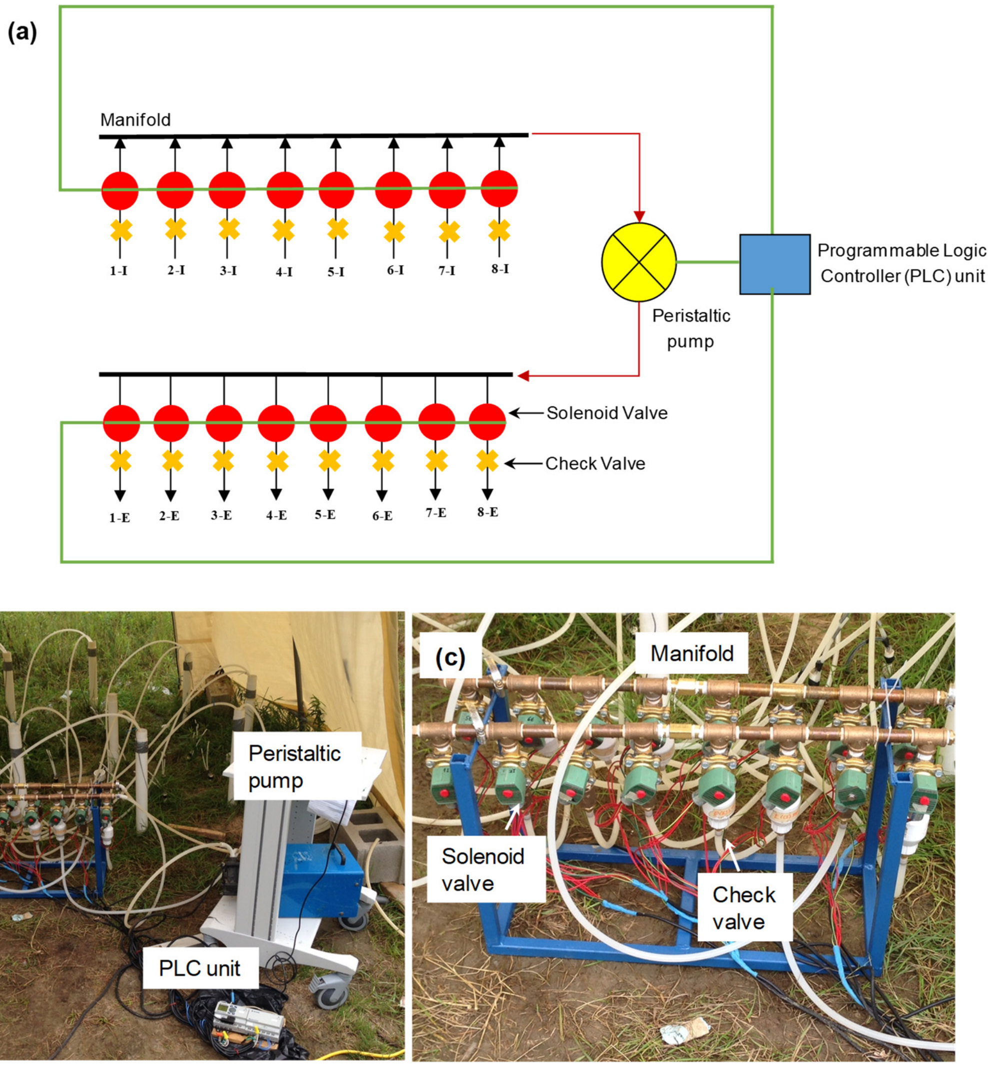

Figure D-1. (a) Schematic of the aboveground dipole pumping system. Arrows indicate direction of flow, numbers indicate the well number in which the tubing was placed, "I" indicates injection port, "E" indicates extraction port, and the green line represents the wiring connection throughout the system; (b) and (c) images of dipole pumping system showing the PLC unit, solenoid valves, check values, and manifold.

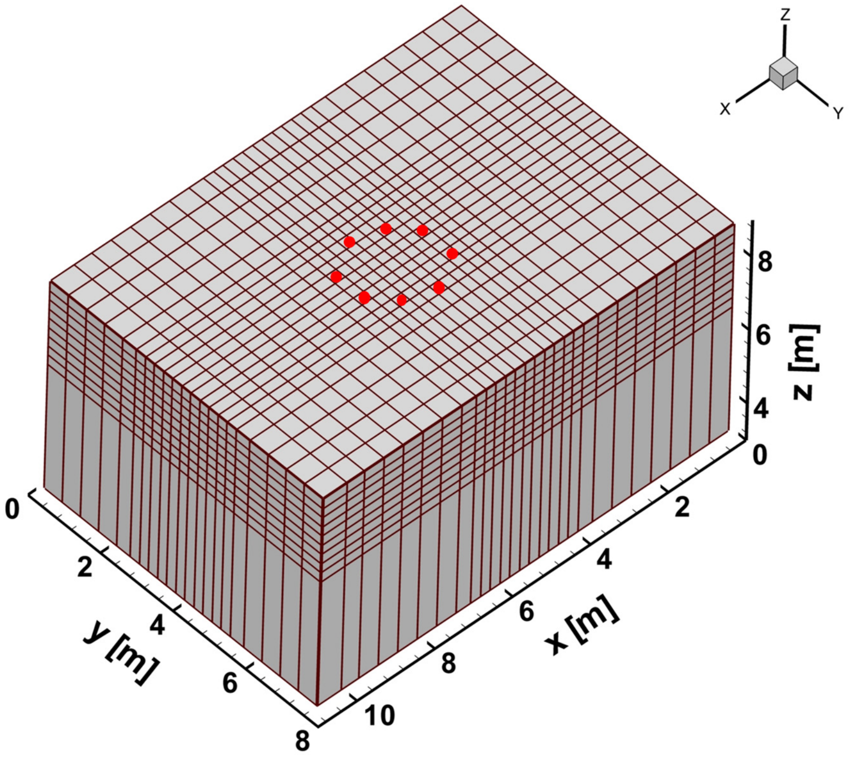

Figure D-2. Finite element mesh (6776 elements and 8004 nodes) used in the SSLE model for SSHT analysis.

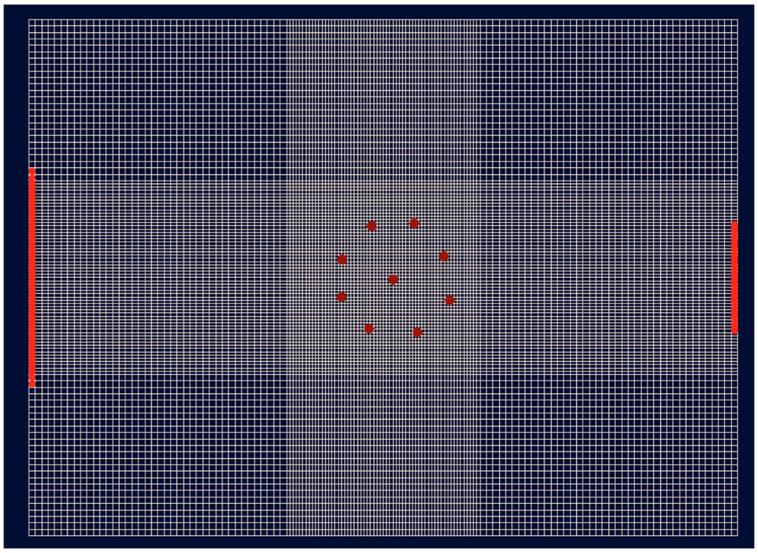

Figure D-3. Finite difference grid (110 rows, 140 columns and 51 layers) used in Visual MODFLOW® Flex for transient flow and particle tracking simulations. Red symbols indicate the location of the IE wells, and the red lines indicate the constant head boundary condition assigned to the upper 2 m of the model domain corresponding to the openings in the experimental cell.

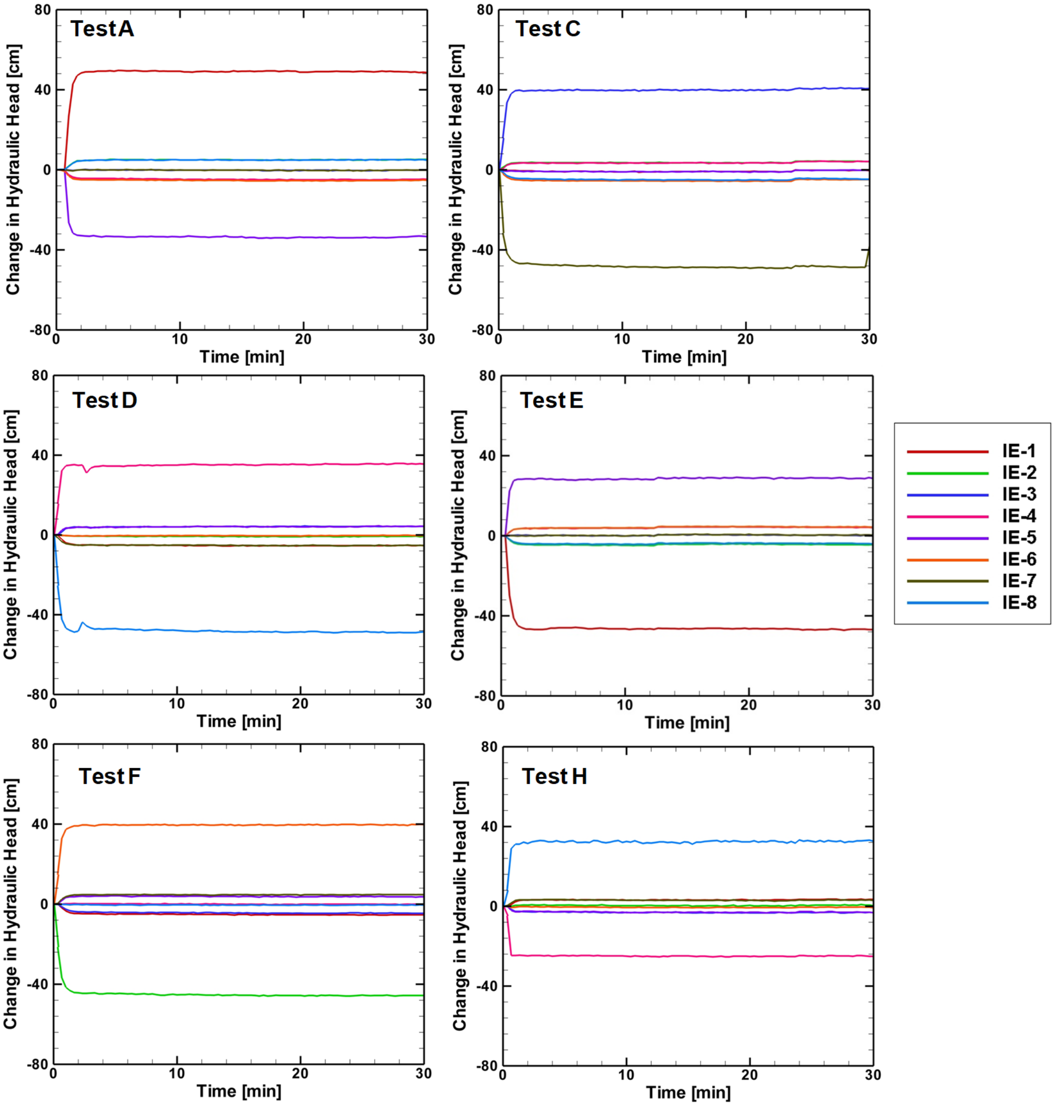

Figure D-4. Observed hydraulic head changes in all 8 IE wells during the six independent dipole pumping tests (Test A, C, D, E, F and H) conducted as part of the Stage-1 hydraulic tomography survey.

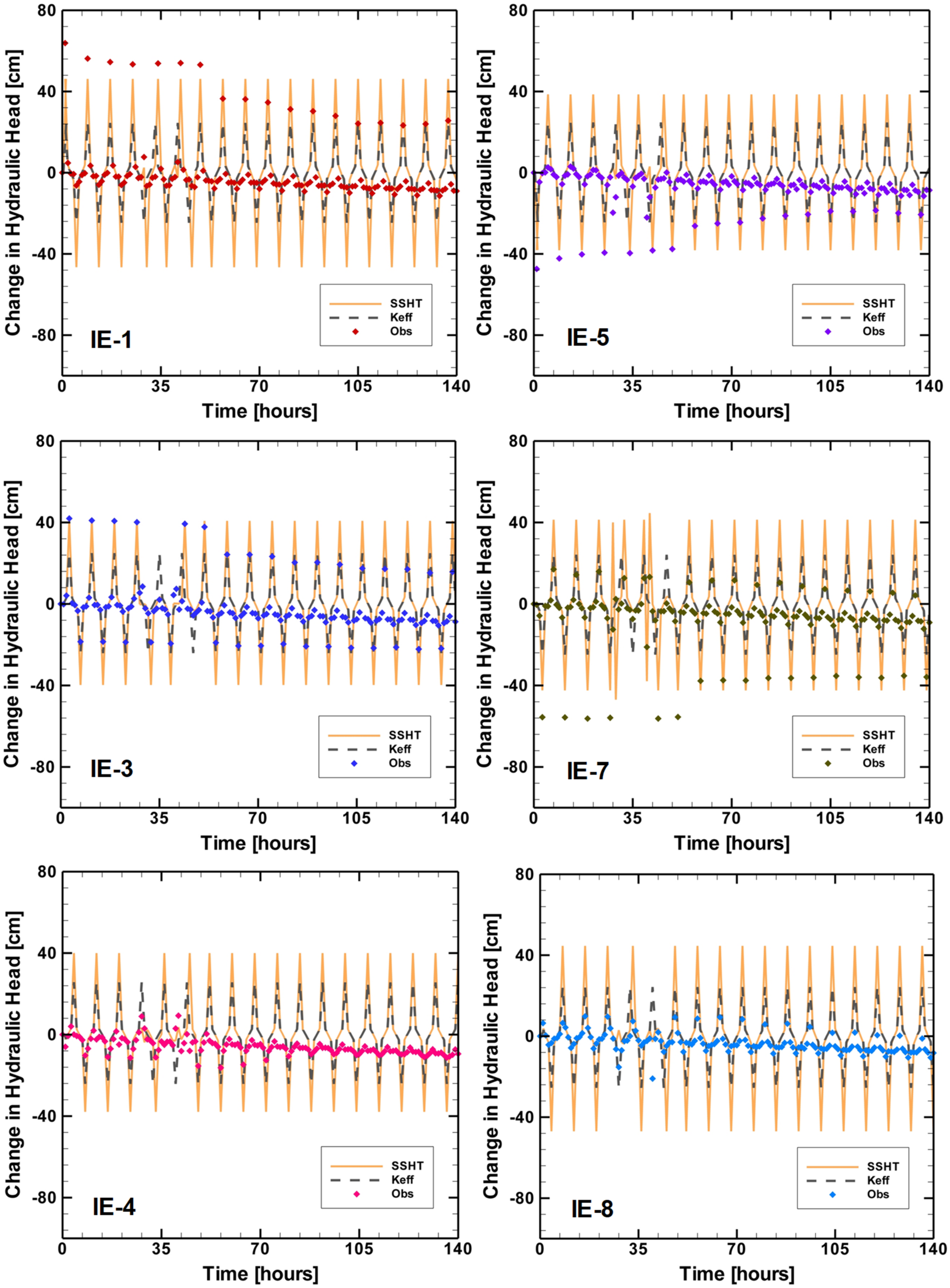

Figure D-5. Temporal hydraulic head changes in the IE wells during implementation of the RPM flow protocol conducted as part of the Stage-2 hydraulic tomography survey. The solid orange lines are the simulated hydraulic head changes produced by the SSHT scenario, while the dotted grey lines are those produced by the K_{eff} scenario. The symbols represent the observed hydraulic head changes during the RPM flow protocol.

Appendix E

Supplementary Figures for Chapter 4

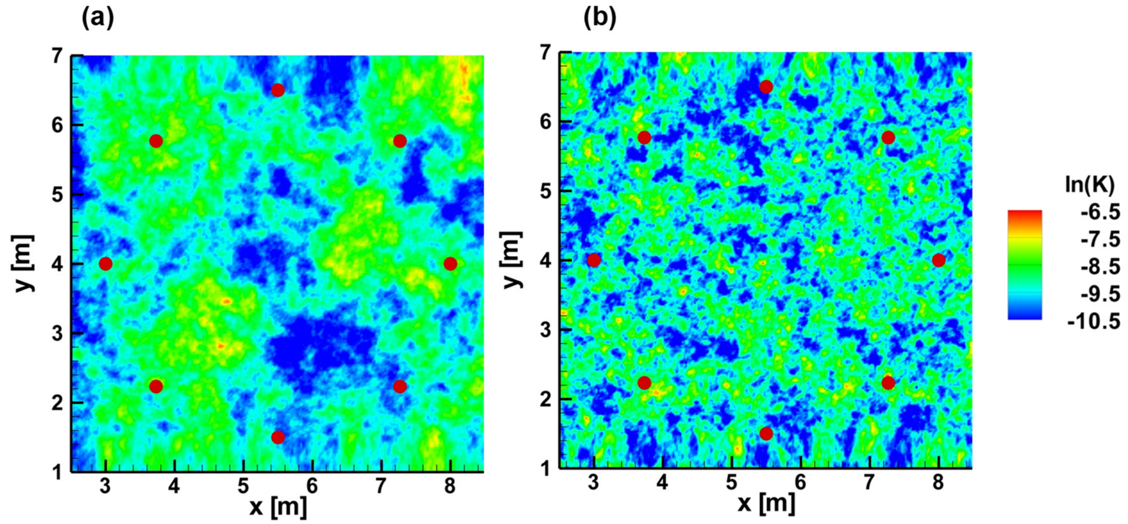

Figure E-1. Contours of the randomly generated heterogeneous *K* fields using FGEN92 with 8.5x10^{-5} m/s for the geometric mean *K*, 0.5 for the variance of the ln*(K)* and correlation lengths of: (a) 0.5 m, and (b) 0.1 m in the *x*- and *y*- directions.

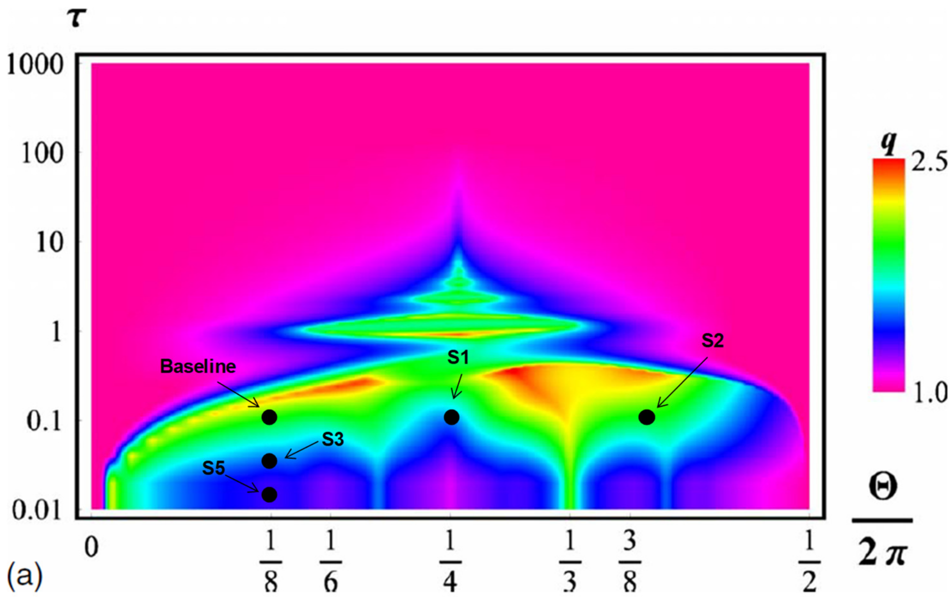

Figure E-2. Distribution of the theoretical parameter *q*, for Peclet number (Pe) = 10^1, adopted from Lester et al. (2010a). The parameter *q* describes the ratio of mixing time associated with an RPM flow, and purely dispersive system with higher values indicative of a faster rate of reagent mixing. The black circles show the approximate value of *q* for the RPM flow parameters (re-orientation angle, pumping duration and flow rate) associated with the baseline scenario, and scenarios S1, S2, S3 and S5.

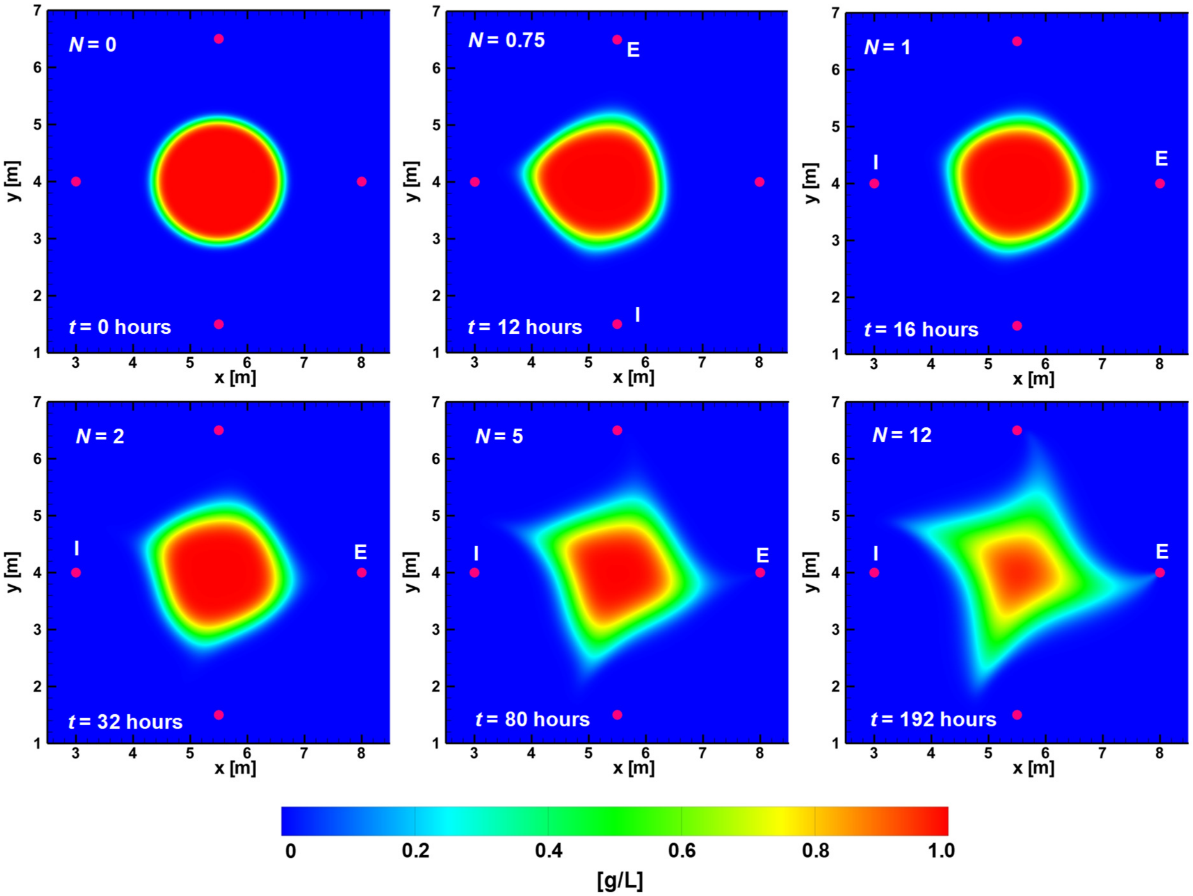

Figure E-3. Contours of simulated reagent concentrations during RPM flow for Scenario S1 (Θ = 90°, Q_{RPM} = 5 m^3/d, t_p = 4 hours, D = 5 m and N = 12) at select times, t. The pink circles indicate IE well locations used for the RPM flow system, with "I" and "E" on each panel denoting the location of the active injection and extraction well at the select time, respectively, and N is the number of complete RPM flow cycles.

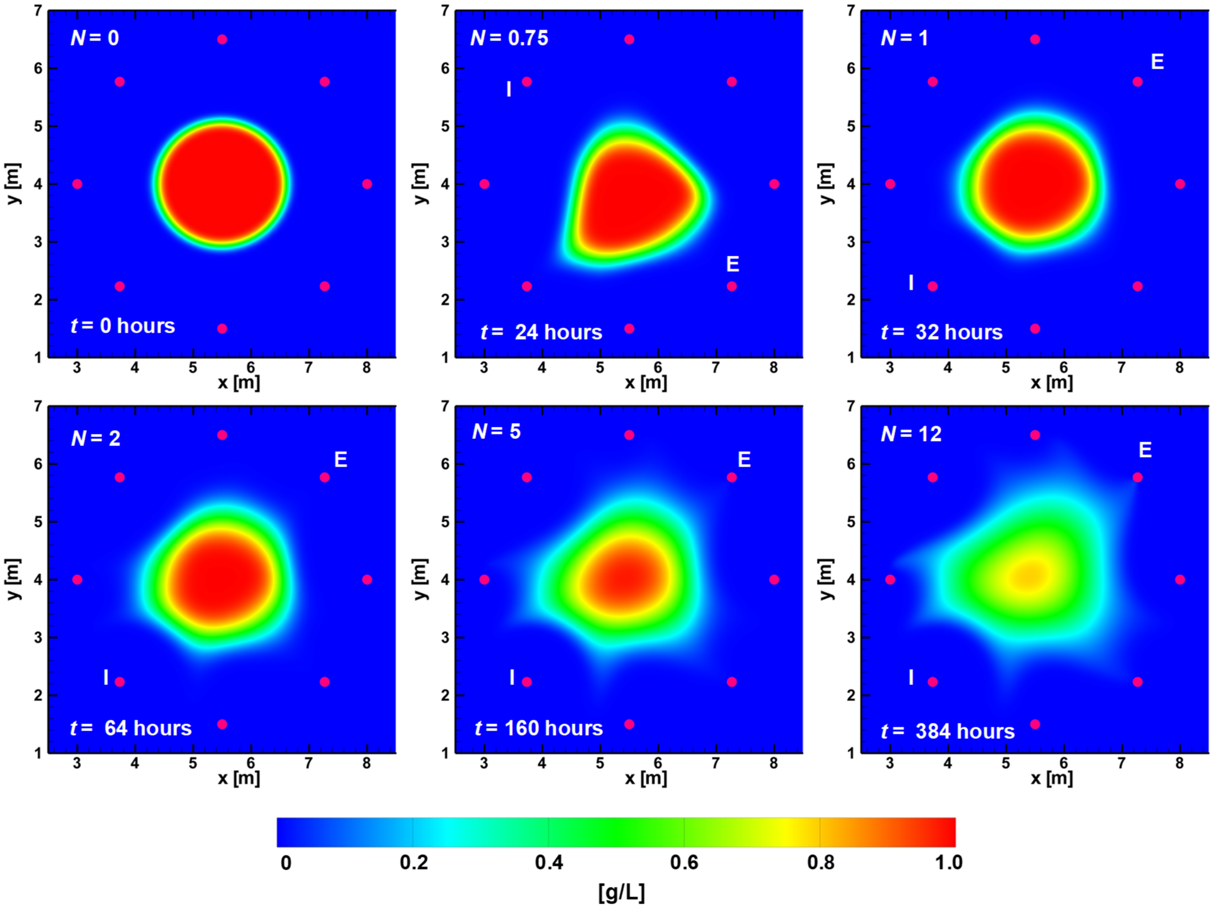

Figure E-4. Contours of simulated reagent concentrations during RPM flow for Scenario S2 ($\Theta = 135°$, $Q_{RPM} = 5$ m^3/d, $t_p = 4$ hours, $D = 5$ m and $N = 12$) at select times, t. The pink circles indicate IE well locations used for the RPM flow system, with "I" and "E" on each panel denoting the location of the active injection and extraction well at the select time, respectively, and N is the number of complete RPM flow cycles.

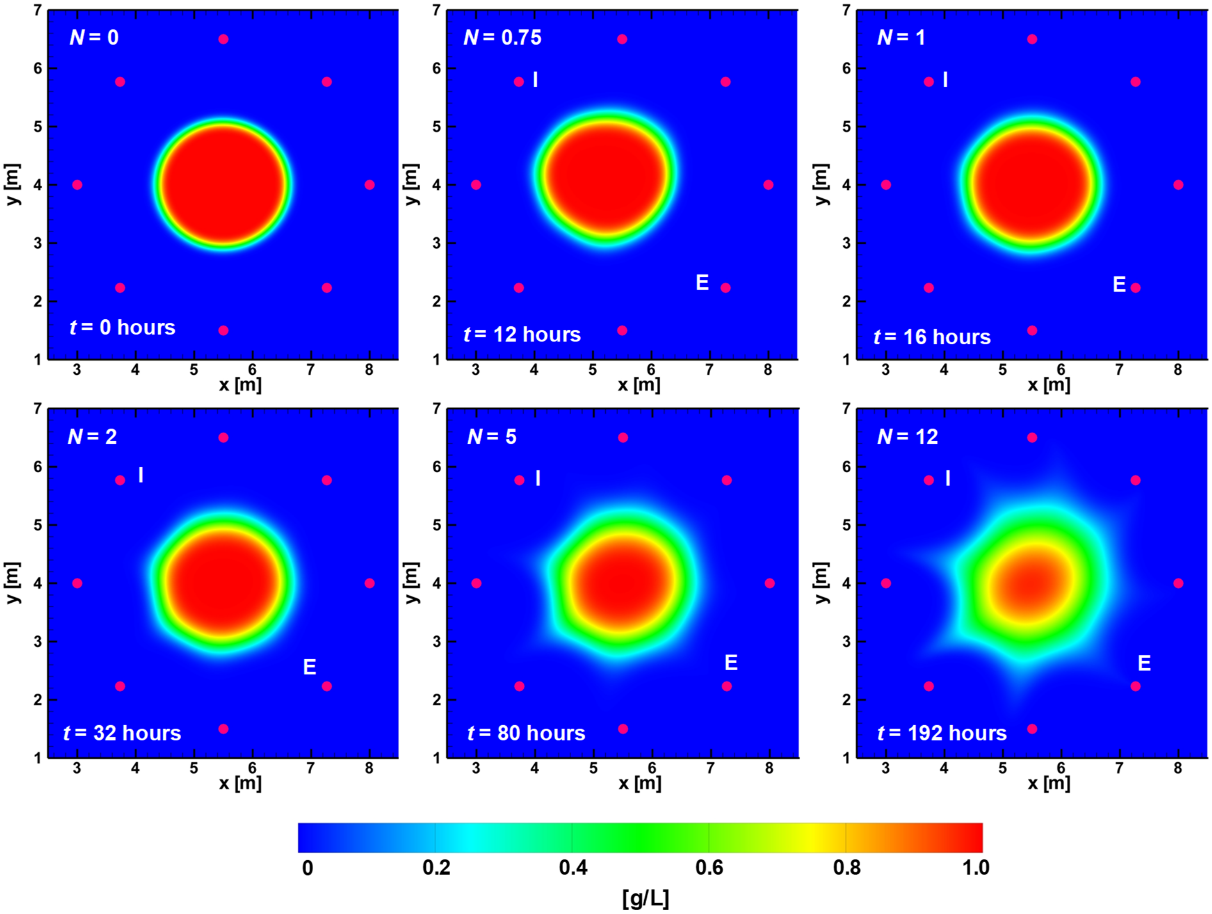

Figure E-5. Contours of simulated reagent concentrations during RPM flow for Scenario S3 (Θ = 45°, Q_{RPM} = 5 m^3/d, t_p = 2 hours, D = 5 m and N = 12) at select times, t. The pink circles indicate IE well locations used for the RPM flow system, with “I” and “E” on each panel denoting the location of the active injection and extraction well at the select time, respectively, and N is the number of complete RPM flow cycles.

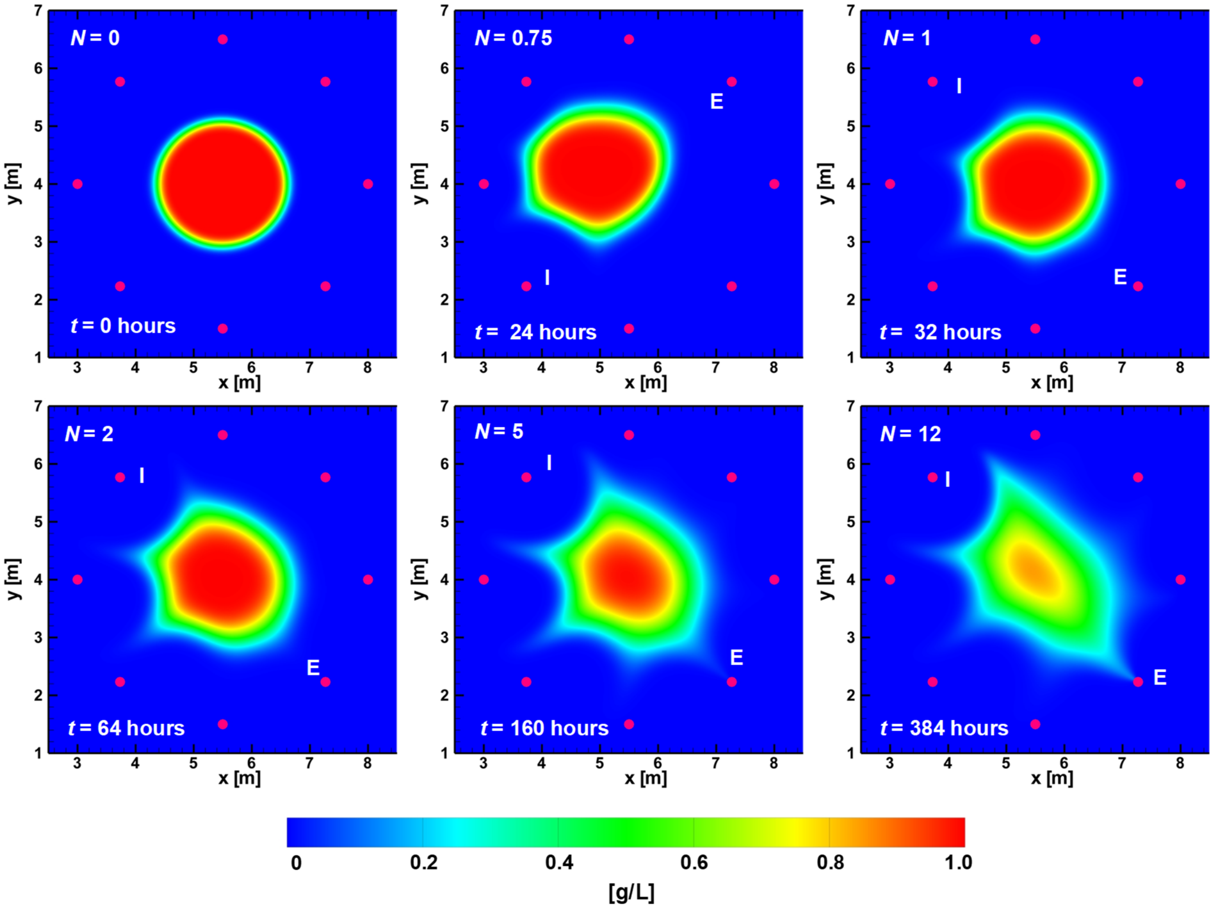

Figure E-6. Contours of simulated reagent concentrations during RPM flow for Scenario S4 ($\Theta = 45°$, $Q_{RPM} = 5$ m^3/d, $t_p = 4$ hours*, $D = 5$ m and $N = 12$, with a sequence of t_p as detailed in Table S1) at select times, t. The pink circles indicate IE well locations used for the RPM flow system, with "I" and "E" on each panel denoting the location of the active injection and extraction well at the select time, respectively, and N is the number of complete RPM flow cycles.

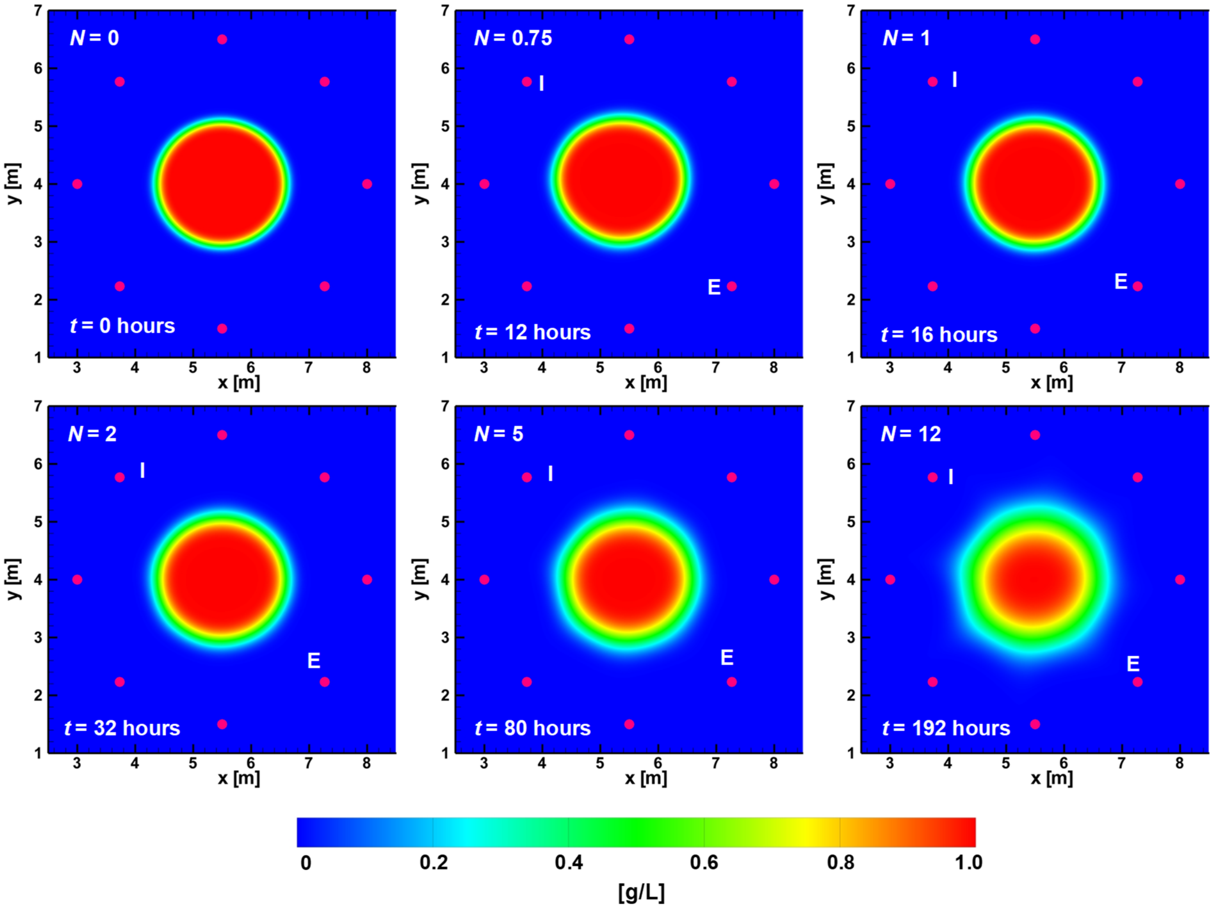

Figure E-7. Contours of simulated reagent concentrations during RPM flow for Scenario S5 (Θ = 45°, Q_{RPM} = 2.5 m^3/d, t_p = 2 hours, D = 5 m and N = 12) at select times, t. The pink circles indicate IE well locations used for the RPM flow system, with "I" and "E" on each panel denoting the location of the active injection and extraction well at the select time, respectively, and N is the number of complete RPM flow cycles.

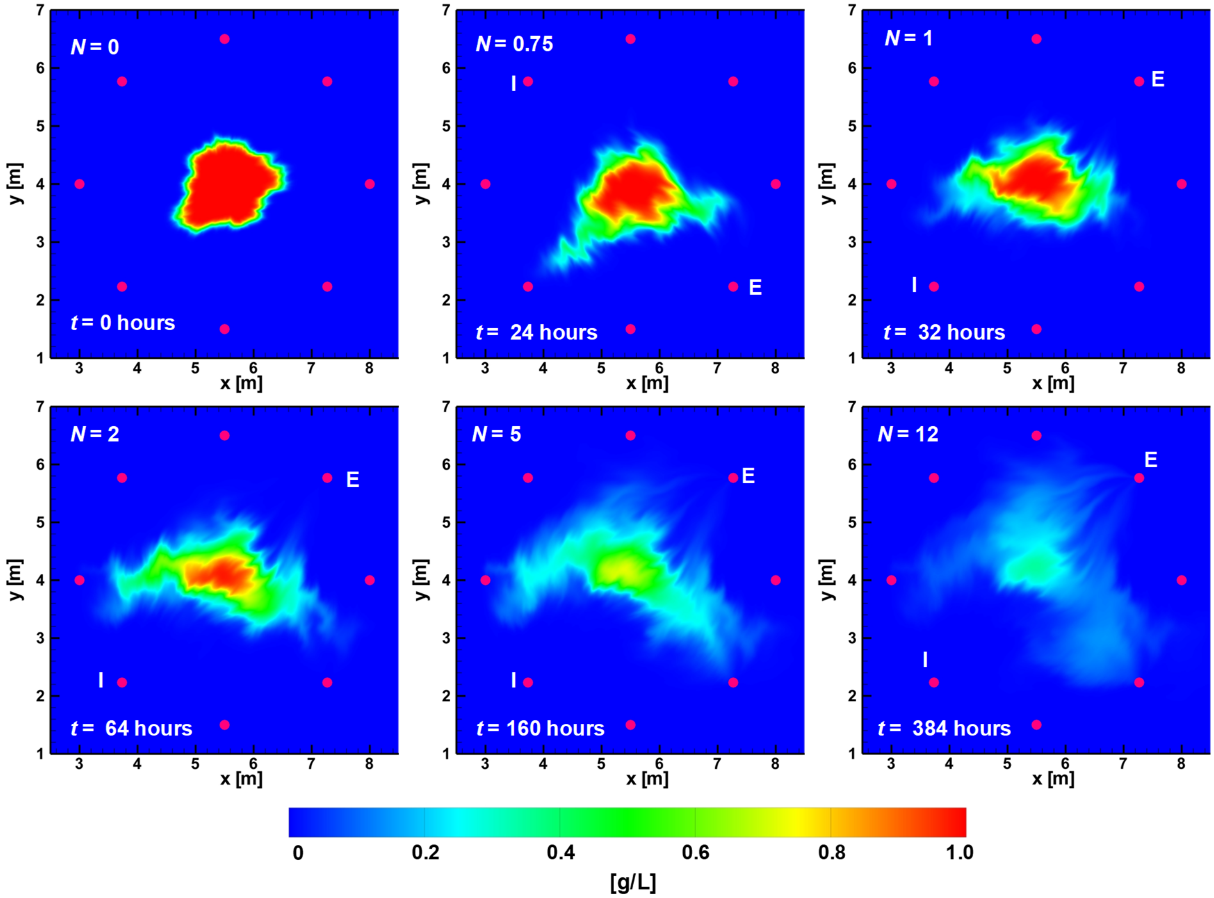

Figure E-8. Contours of simulated reagent concentrations during RPM flow for Scenario S6-A ($\Theta = 135°$, $Q_{RPM} = 5$ m^3/d, $t_p = 4$ hours, $D = 5$ m and $N = 12$ with a randomly generated heterogeneous K field) at select times, t. The pink circles indicate IE well locations used for the RPM flow system, with “I” and “E” on each panel denoting the location of the active injection and extraction well at the select time, respectively, and N is the number of complete RPM flow cycles.

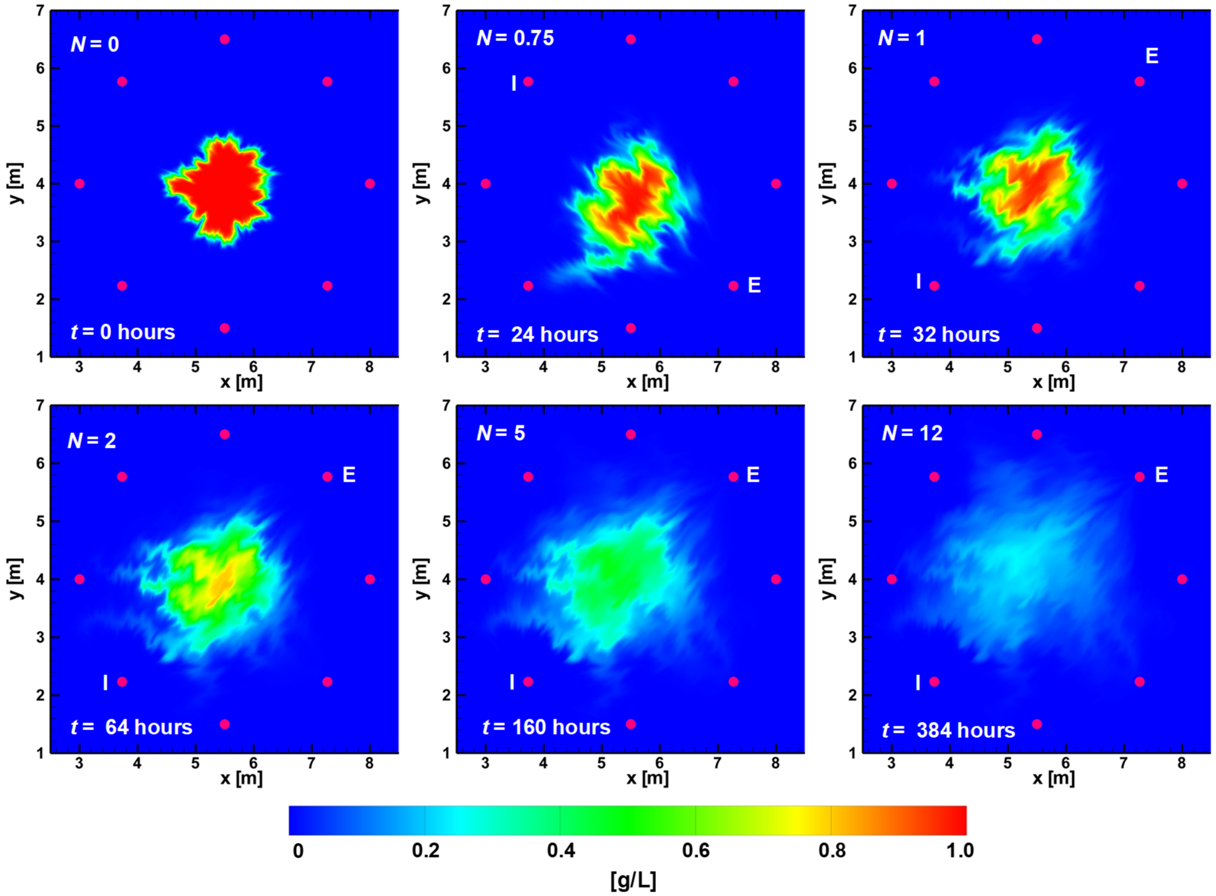

Figure E-9. Contours of simulated reagent concentrations during RPM flow for Scenario S6-B ($\Theta = 135°$, $Q_{RPM} = 5$ m^3/d, $t_p = 4$ hours, $D = 5$ m and $N = 12$ with a randomly generated heterogeneous K field) at select times, t. The pink circles indicate IE well locations used for the RPM flow system, with "I" and "E" on each panel denoting the location of the active injection and extraction well at the select time, respectively, and N is the number of complete RPM flow cycles.

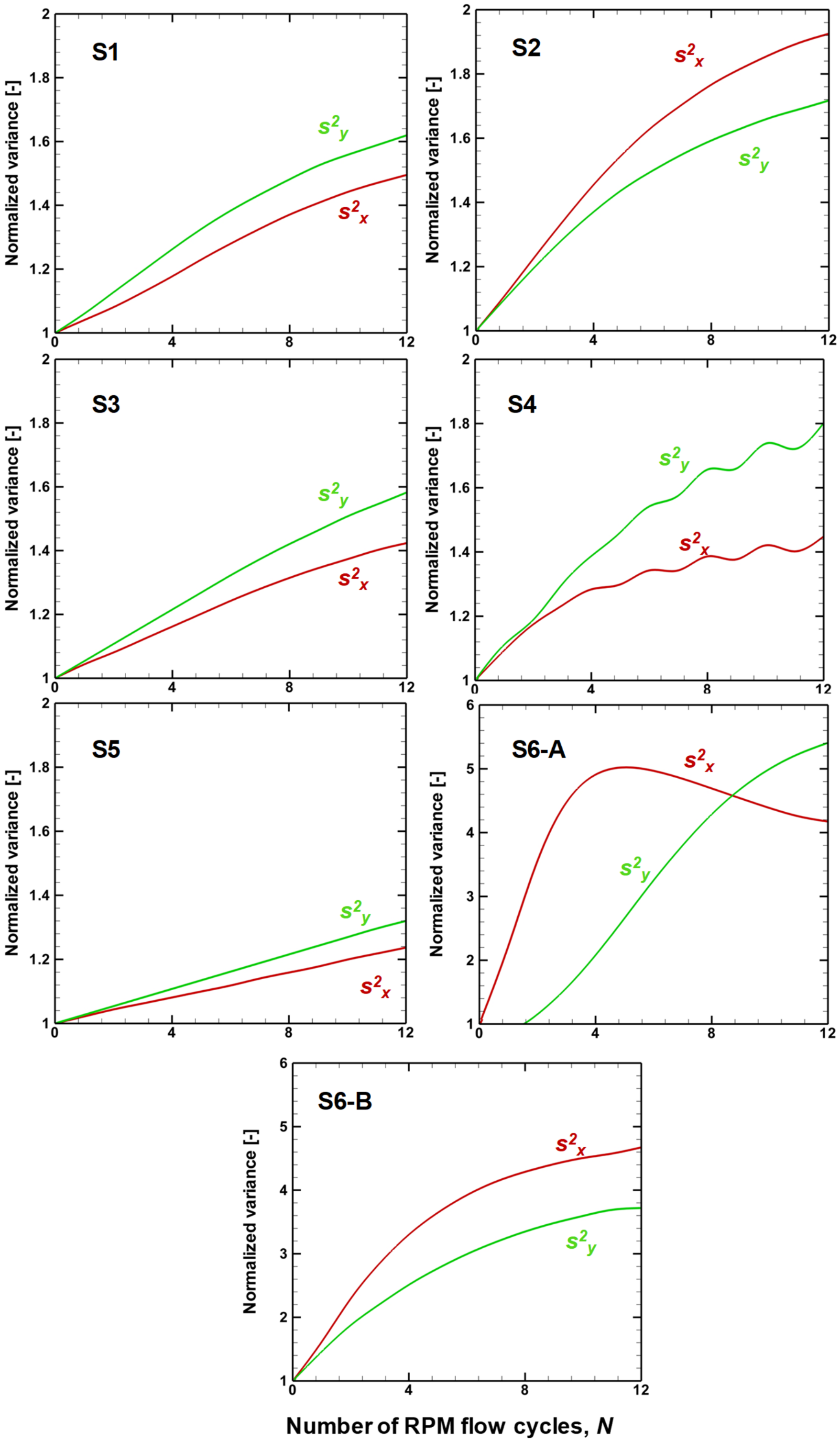

Figure E-10. Temporal profile of the normalized spatial variance $(s_x^2,\ s_y^2)$ for the base case and six scenarios (S1 to S6). Variances were normalized to estimated values from the 2D contours of simulated reagent concentrations immediately after injection.